Learning Embodied Agents with Scalably-Supervised Reinforcement Learning

Lisa Lee

September 2021
CMU-ML-21-111

Machine Learning Department
School of Computer Science
Carnegie Mellon University
Pittsburgh, PA

Submitted in partial fulfillment of the requirements for the degree of Doctor of Philosophy.

This research was sponsored by the National Science Foundation Graduate Research Fellowships Program under grant DGE1745016 and IIS1617583, the National Physical Sciences Consortium Fellowship, the Defense Advanced Research Projects Agency under grant FA870215D0002, the US Army under grant W911NF1920104, and a gift from Nvidia.

Keywords: Deep reinforcement learning, artificial intelligence, computer vision, exploration, meta-learning, multi-task learning, multimodal learning, self-supervised RL, weakly-supervised learning, representation learning, robotic continuous control, embodied visually-grounded navigation

Abstract

Reinforcement learning (RL) agents learn to perform a task through trial-and-error interactions with an initially unknown environment. Despite the recent progress in deep RL, it remains a challenge to train intelligent agents that can efficiently explore a large state space and quickly solve a wide variety of tasks. One of the biggest obstacles is the high cost of human supervision for RL: it is difficult to design reward functions that provide enough learning signal yet still induce the correct behavior at convergence. To reduce the amount of human supervision required, there has been recent progress on self-supervised RL approaches, where the agent learns on its own by interacting with the environment without an extrinsic reward function. However, without any prior knowledge about the task, these methods can be sample-inefficient and suffer from poor exploration. Towards solving these challenges, this thesis focuses on how we can balance self-supervised RL with scalable forms of human supervision to efficiently train an agent for solving various high-dimensional robotic tasks. Being mindful about the cost of human labor required, we consider alternative modalities of supervision that can be more scalable and easier to provide from the human user. We show that such supervision can drastically improve the agent's learning efficiency, enabling the agent to do directed exploration and learning within a large search space of states.

Contents

List of Figures

List of Tables

Chapter 1

Introduction

Reinforcement learning (RL) is a field within machine learning which studies how an agent learns to perform a task through trial-and-error interactions with an initially unknown environment. Deep learning has helped achieve major breakthroughs in RL by enabling methods to automatically learn features from high-dimensional observations, such as image pixels, tactile sensors, and robot joint sensors. As a result, these advances have especially benefited robotic and vision-based applications, enabling RL agents to solve specific, well-defined tasks from low-level sensory inputs.

Despite the progress, several unsolved challenges limit the applicability of RL to real world tasks. RL is computationally intensive to train, especially in domains where each interaction with the environment is expensive. Real world applications require the agent to solve a wide variety of tasks, but training RL from scratch for each task is computationally infeasible. It remains an open challenge to improve the learning and data efficiency of RL agents, and to share and reuse experience across tasks so that learned skills can be transferred to new tasks and dynamics.

Most importantly, the cost of human supervision is perhaps the largest roadblock for widely deploying RL in the real world. Reward functions require inordinate amounts of tuning and can be difficult to design, especially in high-dimensional problems. Instead of relying on reward functions, an alternative approach is to learn to imitate some expert behavior. However, these *imitation learning* approaches, such as inverse RL [Hadfield-Menell et al., 2017, Ziebart et al., 2008, Fu et al., 2017], have a voracious appetite for expert demonstrations, which can be difficult to obtain in domains with high-dimensional action spaces. Moreover, human demonstrations are often not perfect, and it remains an open question of how to explore and extrapolate beyond suboptimal demonstrations [Levine, 2018, Brown et al., 2019].

To reduce data requirements for RL, there has been recent progress on self-supervised RL approaches, where the agent learns on its own by interacting with the environment. These include intrinsic rewards for exploration [Burda et al., 2018, Schmidhuber, 1991, Chentanez et al., 2005, Stadie et al., 2015, Pathak et al., 2017], mutual-information objectives [Achiam et al., 2018, Eysenbach et al., 2018, Co-Reyes et al., 2018], and goal-conditioned RL [Andrychowicz et al., 2017] among others. While these methods do not require an extrinsic reward function or demonstration provided by a human, self-supervised approaches are notorious for being sample-inefficient and computationally expensive to train.

Can we find a balance between self-supervision and human-supervision for training RL algorithms? In this thesis, we will be mindful about the cost of human supervision, and consider alternative modalities of supervision that can be more scalable and easier to provide from the human. When thinking about how to scalably supervise RL, there are a number of desiderata to consider:

1. *Convenient user interface*: A human should be able to supervise and interact with the agent in a way that is easy and accessible to anyone, without requiring much time or expert knowledge. The user interface should also support *multimodal* supervision signals, allowing the human to provide different modalities of feedback (e.g., verbal language instructions and visual cues).

2. *Data-efficient learning*: The algorithm should be sample-efficient with respect to both the number of environment interactions, as well as the number of human labels. We should be conscious of how much time the human needs to spend supervising the agent, and we should also utilize that supervision in order to drastically cut down the number of environment interactions needed.

3. *Efficient, safe, and controllable exploration*: In order to achieve effective and efficient human-agent interaction, the agent needs to have efficient exploration capabilities. In other words, the agent should be equipped with the ability to explore interesting and novel states, so that the human can provide feedback on a diverse range of behaviors. The agent should also be able to explore in a safe and controllable manner, so that the agent can learn on its own without requiring constant supervision.

With all of these points in mind, we will study how we can balance self-supervised RL with scalable forms of human supervision in order to accelerate learning, improve generalization, and amortize the cost of human supervision. We will show how scalable supervision can be used to greatly benefit exploration and representation learning for RL, significantly improving learning efficiency over purely self-supervised approaches, while being less costly than fully-supervised approaches.

1.1 Overview

Chapter 2: Task-Agnostic Exploration via State Marginal Matching

Having a good exploratory policy that visits a diverse range of states can enable the agent to learn faster, especially in sparse reward settings, and also allows the human to provide more meaningful feedback on the agent's behavior. Moreover, being able to control how the agent does exploration can improve safety for deploying RL algorithms in real-world scenarios, and accelerate learning by focusing training on only the relevant subspace of tasks.

There has been considerable progress on exploration for RL, one common approach being intrinsic rewards as exploration bonuses [Burda et al., 2018, Schmidhuber, 1991, Chentanez et al., 2005, Stadie et al., 2015, Pathak et al., 2017]. However, these methods are often focused on learning to explore for only a single task, and it is unclear how to repurpose these methods for multi-task exploration, *i.e.*, reusing exploration experience from one task to acquire exploration strategies for another task. Moreover, it is often unclear what underlying objective is being optimized by these exploration algorithms, or how they can be altered to incorporate domain knowledge about the task.

How can we *measure* what is "good" exploration? How can we *understand* what previous exploration algorithms are doing and why they work? And lastly, how can we *amortize* the cost of learning to explore in a multi-task setting? To answer these questions, we recast exploration as a problem of *State Marginal Matching (SMM)*, where we aim to learn a policy for which the state marginal distribution matches a given target state distribution [Lee et al., 2019b]. This objective provides a clear and explicit objective for exploration, and additionally provides a convenient mechanism to incorporate prior knowledge about the task through the target distribution.

The SMM objective can be viewed as a two-player, zero-sum game between a state density model and a parametric policy, an idea that we use to build an algorithm for optimizing the SMM objective. Using this formalism, we further demonstrate that existing exploration methods approximately maximize the SMM objective, offering an explanation for the success of these methods.

While most prior work on exploration has focused on the single task setting, we show how a single, stochastic *exploration* policy learned with state marginal matching can be reused to quickly solve downstream tasks. On both simulated and real-world tasks, we demonstrate that directly optimizing the SMM objective results in agents that explore faster and adapt more quickly to new tasks as compared to prior exploration methods.

Chapter 3: Weakly-Supervised RL for Controllable Behavior

State Marginal Matching and many other unsupervised exploration methods [Andrychowicz et al., 2017, Hazan et al., 2018] require knowing a relatively low-dimensional, usually disentangled state representation that informs the agent how to explore. However, acquiring such state representations without a good exploration policy is often difficult. This chicken-and-egg problem between exploration and representation learning often hinders the applicability of RL to high-dimensional tasks.

How can we efficiently guide exploration and learning of an RL agent acting in a high-dimensional environment, without requiring expensive human supervision? In many settings, an agent must winnow down the inconceivably large space of all possible tasks to the single task that it is currently being asked to solve. Can we instead constrain the space of tasks to those that are semantically meaningful?

In Chapter 3, we introduce a framework for using weak supervision to automatically disentangle this semantically meaningful subspace of tasks from the enormous space of nonsensical "chaff" tasks. We show that this learned subspace enables efficient exploration in challenging, vision-based continuous control problems, and provides a representation that captures distance between states. Our approach leads to substantial performance gains over prior state-of-the-art methods, particularly as the complexity of the environment grows.

Chapter 4: Multimodal Learning of Language, Vision and Control

In the previous chapter, we use a learned, semantically disentangled latent goal space in order to guide the exploration, goal generation, and learning of RL. More generally, language provides a way to encode combinatorial abstractions and generalizations of the visual and physical world. It also enables us to communicate instructions, questions, plans, and intentions to one another. How can we utilize language to equip deep RL agents with structured priors about the physical world, and enable generalization and knowledge transfer across different tasks?

As a case study, we consider training an embodied agent with goals specified via language. The embodied agent interacts with a 3D environment by receiving first-person RGB views of the environment and taking navigational actions. We introduce a dual-attention architecture that disentangles the knowledge of words and visual attributes in order to transfer grounded knowledge across different tasks, and to new words and concepts not seen during training [Chaplot et al., 2020]. Additionally, we demonstrate that the modularity of our model allows easy addition of new objects and attributes to a trained model.

1.2 Summary of Publications & Open-Source Contributions

The content of chapter 2 appears in:

> Lisa Lee, Benjamin Eysenbach, Emilio Parisotto, Eric Xing, Sergey Levine, and Ruslan Salakhutdinov. Efficient exploration via state marginal matching. *arXiv preprint arXiv:1906.05274*, 2019b
> **Code:** `https://github.com/RLAgent/state-marginal-matching`

The content of chapter 3 appears in:

> Lisa Lee, Benjamin Eysenbach, Ruslan Salakhutdinov, Chelsea Finn, et al. Weakly-supervised reinforcement learning for controllable behavior. *Neural Information Processing Systems (NeurIPS)*, 2020
> **Code:** `https://github.com/google-research/weakly_supervised_control`

The content of chapter 4 appears in:

> Devendra Singh Chaplot, Lisa Lee, Ruslan Salakhutdinov, Devi Parikh, and Dhruv Batra. Embodied multimodal multitask learning. *International Joint Conference on Artificial Intelligence (IJCAI)*, 2020
> **Code:** `https://github.com/devendrachaplot/DeepRL-Grounding`

I have also pursued the following research directions during my Ph.D. studies, which are excluded from this thesis:

> Lisa Lee, Emilio Parisotto, Devendra Singh Chaplot, Eric Xing, and Ruslan Salakhutdinov. Gated path planning networks. In *International Conference on*

Machine Learning (ICML), pages 2947–2955. PMLR, 2018
Code: https://github.com/RLAgent/gated-path-planning-networks

Tianwei Ni, Harshit Sikchi, Yufei Wang, Tejus Gupta, Lisa Lee, and Benjamin Eysenbach. F-irl: Inverse reinforcement learning via state marginal matching. *Conference on Robot Learning (CoRL)*, 2020
Code: https://github.com/twni2016/f-IRL

Xiaodan Liang, Lisa Lee, and Eric P Xing. Deep variation-structured reinforcement learning for visual relationship and attribute detection. In *Proceedings of the IEEE conference on Computer Vision and Pattern Recognition (CVPR)*, pages 848–857, 2017b

Xiaodan Liang, Lisa Lee, Wei Dai, and Eric P Xing. Dual motion gan for future-flow embedded video prediction. In *Proceedings of the IEEE International Conference on Computer Vision (ICCV)*, pages 1744–1752, 2017a

Yohan Jo, Lisa Lee, and Shruti Palaskar. Combining lstm and latent topic modeling for mortality prediction. *arXiv preprint arXiv:1709.02842*, 2017

Maruan Al-Shedivat, Lisa Lee, Ruslan Salakhutdinov, and Eric Xing. On the complexity of exploration in goal-driven navigation. *arXiv preprint arXiv:1811.06889*, 2018

Chapter 2

Task-Agnostic Exploration via State Marginal Matching

Reinforcement learning (RL) algorithms must be equipped with exploration mechanisms to effectively solve tasks with long horizons and limited or delayed reward signals. These tasks arise in many real-world applications where providing human supervision is expensive.

Exploration for RL has been studied in a wealth of prior work. The optimal exploration strategy is intractable to compute in most settings, motivating work on tractable heuristics for exploration [Kolter and Ng, 2009]. Exploration methods based on random actions have limited ability to cover a wide range of states. More sophisticated techniques, such as intrinsic motivation, accelerate learning in the single-task setting. However, these methods have two limitations: (1) First, they lack an explicit objective to quantify "good exploration," but rather argue that exploration arises implicitly through some iterative procedure. Lacking a well-defined optimization objective, it remains unclear what these methods are doing and why they work. Similarly, the lack of a metric to quantify exploration, even if only for evaluation, makes it difficult to compare exploration methods and assess progress in this area. (2) The second limitation is that these methods target the single-task setting. Because these methods aim to converge to the optimal policy for a particular task, it is difficult to repurpose these methods to solve multiple tasks.

We address these shortcomings by recasting exploration as a problem of *State Marginal Matching (SMM)*: Given a target state distribution, we learn a policy for which the state marginal distribution matches this target distribution. Not only does the SMM problem provide a clear and explicit objective for exploration, but it also provides a convenient mechanism to incorporate prior knowledge about the task through the target distribution — whether in the form of safety constraints that the agent should obey; preferences for some states over other states; reward shaping; or the relative importance of each state dimension for a particular task. Without any prior information, the SMM objective reduces to maximizing the marginal state entropy $\mathcal{H}[s]$, which encourages the policy to visit all states.

In this work, we study state marginal matching as a metric for task-agnostic exploration. While this class of objectives has been considered in Hazan et al. [2018], we build on this prior work in a number of dimensions:

1. We argue that the SMM objective is an effective way to learn a *single, task-agnostic exploration policy* that can be used for solving many downstream tasks, amortizing the cost of learning to explore for each task. Learning a single exploration policy is considerably more difficult than doing exploration throughout the course of learning a single task. The latter is done by intrinsic motivation [Pathak et al., 2017, Tang et al., 2017, Oudeyer et al., 2007] and count-based exploration [Bellemare et al., 2016], which can effectively explore to find states with high reward, at which point the agent can decrease exploration and increase exploitation of those high-reward states. While these methods perform efficient exploration for learning a single task, we show in Sec. 2.3 that the policy at any particular iteration is not a good exploration policy.

   In contrast, maximizing $\mathcal{H}[s]$ produces a stochastic policy at convergence that visits states in proportion to their density under a target distribution. We use this policy as an exploration prior in our multi-task experiments, and also prove that this policy is optimal for a class of goal-reaching tasks (Section 2.5).

2. We explain how to optimize the SMM objective properly. By viewing the objective as a two-player, zero-sum game between a state density model and a parametric policy, we propose a practical algorithm to jointly learn the policy and the density by using fictitious play [Brown, 1951].

   We further decompose the SMM objective into a mixture of distributions, and derive an algorithm for learning a mixture of policies that resembles the mutual-information objectives in recent work [Achiam et al., 2018, Eysenbach et al., 2018, Co-Reyes et al., 2018]. Thus, these prior work may be interpreted as also almost doing distribution matching, with the caveat that they omit the state entropy term.

3. Our analysis provides a unifying view of prior exploration methods as *almost* performing distribution matching. We show that exploration methods based on predictive error approximately optimizes the same SMM objective, offering an explanation for the success of these methods. However, they omit a crucial historical averaging step, potentially explaining why they do not converge to an exploratory policy.

4. We demonstrate on complex RL tasks that optimizing the SMM objective allows for faster exploration and adaptation than prior state-of-the-art exploration methods.

In short, our work contributes a method to measure, amortize, and understand exploration.

2.1 State Marginal Matching

In this section, we start by showing that exploration methods based on prediction error do not acquire a single exploratory policy. This motivates us to define the State Marginal Matching problem as a principled objective for *learning to explore*. We then introduce an extension of the SMM objective using a mixture of policies.

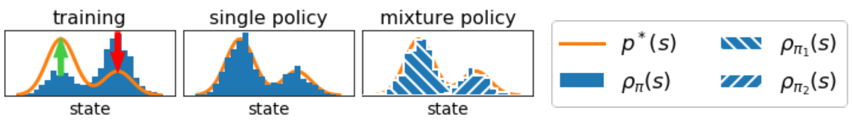

Figure 2.1: **State Marginal Matching**: *(Left)* Our goal is to learn a policy whose state distribution $\rho_\pi(s)$ matches some target density $p^*(s)$. Our algorithm iteratively increases the reward on states visited too infrequently (green arrow) and decreases the reward on states visited too frequently (red arrow). *(Center)* At convergence, these two distributions are equal. *(Right)* For complex target distributions, we use a mixture of policies $\rho_\pi(s) = \int \rho_{\pi_z}(s)p(z)dz$.

2.1.1 Why Prediction Error is Not Enough

Exploration methods based on prediction error [Burda et al., 2018, Stadie et al., 2015, Pathak et al., 2017, Schmidhuber, 1991, Chentanez et al., 2005] do not converge to an exploratory policy, even in the absence of extrinsic reward. For example, consider the asymptotic behavior of ICM [Pathak et al., 2017] in a deterministic MDP, such as the Atari games where it was evaluated. At convergence, the predictive model will have zero error in all states, so the exploration bonus is zero – the ICM objective has no effect on the policy at convergence. Similarly, consider the exploration bonus in Pseudocounts [Bellemare et al., 2016]: $1/\hat{n}(s)$, where $\hat{n}(s)$ is the (estimated) number of times that state s has been visited. In the infinite limit, each state has been visited infinitely many times, so the Pseudocount exploration bonus also goes to zero — Pseudocounts has no effect at convergence. Similar reasoning can be applied to other methods based on prediction error [Burda et al., 2018, Stadie et al., 2015]. More broadly, we can extend this analysis to stochastic MDPs, where we consider an abstract exploration algorithm that alternates between computing some intrinsic reward and performing RL (to convergence) on that intrinsic reward. Existing prediction-error exploration methods are all special cases. At each iteration, the RL step solves a fully-observed MDP, which always admits a deterministic policy as a solution [Puterman, 2014]. Thus, any exploration algorithm in this class cannot converge to a single, exploratory policy. Next, we present an objective which, when optimized, yields a single exploratory policy.

2.1.2 The State Marginal Matching Objective

We consider a parametric policy $\pi_\theta \in \Pi \triangleq \{\pi_\theta \mid \theta \in \Theta\}$, e.g. a policy parameterized by a deep network, that chooses actions $a \in \mathcal{A}$ in a Markov Decision Process (MDP) with fixed episode lengths T, dynamics distribution $p(s_{t+1} \mid s_t, a_t)$, and initial state distribution $p_0(s)$. The MDP together with the policy π_θ form an implicit generative model over states. We define the *state marginal distribution* $\rho_\pi(s)$ as the probability that the policy visits state s:

$$\rho_\pi(s) \triangleq \mathbb{E}_{\substack{s_1 \sim p_0(S), \\ a_t \sim \pi_\theta(A|s_t) \\ s_{t+1} \sim p(S|s_t, a_t)}} \left[\frac{1}{T} \sum_{t=1}^{T} \mathbb{1}(s_t = s) \right]$$

The state marginal distribution $\rho_\pi(s)$ is a distribution of states, not trajectories: it is the distribution over states visited in a finite-length episode, not the stationary distribution of the policy after infinitely many steps.[1]

[1] $\rho_\pi(s)$ approaches the policy's stationary distribution in the limit as the episodic horizon $T \to \infty$.

We assume that we are given a target distribution $p^*(s)$ over states $s \in \mathcal{S}$ that encodes our belief about the tasks we may be given at test-time. For example, a roboticist might assign small values of $p^*(s)$ to states that are dangerous, regardless of the desired task. Alternatively, we might also learn $p^*(s)$ from data about human preferences [Christiano et al., 2017]. For goal-reaching tasks, we can analytically derive the optimal target distribution (Section 2.5). Given $p^*(s)$, our goal is to find a parametric policy that is "closest" to this target distribution, where we measure discrepancy using the Kullback-Leibler (KL) divergence:

$$\min_{\pi \in \Pi} D_{\mathrm{KL}}(\rho_\pi(s) \parallel p^*(s)) \triangleq \max_{\pi \in \Pi} \mathbb{E}_{\rho_\pi(s)} \ \log p^*(s) + \mathcal{H}_\pi[s] \tag{2.1}$$

The SMM objective in Eq. 2.1 can be viewed as maximizing the pseudo-reward

$$r(s) \triangleq \log p^*(s) - \log \rho_\pi(s) \ ,$$

which assigns positive utility to states that the agent visits too infrequently and negative utility to states visited too frequently (see Fig. 2.1). Maximizing this pseudo-reward is not a RL problem because the pseudo-reward depends on the policy. Maximizing the first term alone without the state entropy regularization term will converge to the *mode* of the target distribution, rather than do distribution matching. Moreover, the SMM objective regularizes the entropy of the state distribution, not the conditional distribution of actions given states, as done in MaxEnt RL [Ziebart et al., 2008, Haarnoja et al., 2018]. This results in exploration in the space of states rather than in actions.

2.1.3 Better SMM with Mixtures of Policies

Given the challenging problem of exploration in large state spaces, it is natural to wonder whether we can accelerate exploration by automatically decomposing the potentially-multimodal target distribution into a mixture of "easier-to-learn" distributions and learn a corresponding set of policies to do distribution matching for each component. Note that the mixture model we introduce here is orthogonal to the historical averaging step discussed before. Using $\rho_{\pi_z}(s)$ to denote the state distribution of the policy conditioned on the latent variable $z \in \mathcal{Z}$, the state marginal distribution of the mixture of policies π_z with prior $p(z)$ is

$$\rho_\pi(s) = \int_{\mathcal{Z}} \rho_{\pi_z}(s) p(z) dz = \mathbb{E}_{z \sim p(z)} \left[\rho_{\pi_z}(s) \right] . \tag{2.2}$$

As before, we will minimize the KL divergence between this mixture distribution and the target distribution. Using Bayes' rule to re-write $\rho_\pi(s)$ in terms of conditional probabilities, we obtain the following optimization problem:

$$\max_{\substack{\pi_z, \\ z \in \mathcal{Z}}} \mathbb{E}_{\substack{p(z), \\ \rho_{\pi_z}(s)}} \left[r_z(s) \right] \ , \qquad r_z(s) \triangleq \underbrace{\log p^*(s)}_{(a)} - \underbrace{\log \rho_{\pi_z}(s)}_{(b)} + \underbrace{\log p(z \mid s)}_{(c)} - \underbrace{\log p(z)}_{(d)} \tag{2.3}$$

Intuitively, this says that the agent should go to states (a) with high density under the target state distribution, (b) where this agent has not been before, and (c) where this agent is clearly distinguishable from the other agents. The last term (d) says to explore in the space of mixture components z. This decomposition resembles the mutual-information objectives in

Algorithm 1 Learning to Explore via Fictitious Play

```
**Input:** Target distribution $p^*(s)$
Initialize policy $\pi(a \mid s)$, density model $q(s)$, replay buffer $\mathcal{B}$.
**while** not converged **do**
    $q^{(m)} \leftarrow \arg\max_q \mathbb{E}_{s\sim\mathcal{B}^{(m-1)}}[\log q(s)]$
    $\pi^{(m)} \leftarrow \arg\max_\pi \mathbb{E}_{s\sim\rho_\pi(s)}[r(s)]$ where $r(s) \triangleq \log p^*(s) - \log q^{(m)}(s)$
    $\mathcal{B}^{(m)} \leftarrow \mathcal{B}^{(m-1)} \cup \{(s_t, a_t, s_{t+1})\}_{t=1}^T$ with new transitions sampled from $\pi^{(m)}$
**return** historical policies $\{\pi^{(1)}, \cdots, \pi^{(m)}\}$
```

Alg. 1: An algorithm for optimizing the State Marginal Matching objective (Eq. 2.1). The algorithm iterates between (1) fitting a density model $q^{(m)}$ and (2) training the policy $\pi^{(m)}$ with a RL objective to optimize the expected return w.r.t. the updated reward function $r(s)$. The algorithm returns the collection of policies from each iteration, which do distribution matching in aggregate.

recent work [Achiam et al., 2018, Eysenbach et al., 2018, Co-Reyes et al., 2018]. Thus, one interpretation of our work is as explaining that mutual information objectives almost perform distribution matching. The caveat is that prior work omits the state entropy term $-\log \rho_{\pi_z}(s)$ which provides high reward for visiting novel states, possibly explaining why these previous works have failed to scale to complex tasks.

In Appendix 2.5.1, we also discuss how goal-conditioned RL [Kaelbling, 1993, Schaul et al., 2015] can be viewed as a special case of State Marginal Matching when the goal-sampling distribution is learned jointly with the policy.

2.2 A Practical Algorithm

In this section, we develop a principled algorithm for maximizing the state marginal matching objective. We then propose an extension of this algorithm based on mixture modelling, an extension with close ties to prior work.

2.2.1 Optimizing the State Marginal Matching Objective

Optimizing Eq. 2.1 is more challenging than standard RL because the reward function itself depends on the policy. To break this cyclic dependency, we introduce a parametric state density model $q_\psi(s) \in Q \triangleq \{q_\psi \mid \psi \in \Psi\}$ to approximate the policy's state marginal distribution, $\rho_\pi(s)$. We assume that the class of density models Q is sufficiently expressive to represent every policy:

Assumption 1. *For every policy $\pi \in \Pi$, there exists $q \in Q$ such that $D_{KL}(\rho_\pi(s) \,\|\, q(s)) = 0$.*

Under this assumption, optimizing the policy w.r.t. this approximate distribution $q(s)$ will yield the same solution as Eq. 2.1:

Algorithm 2 State Marginal Matching with Mixtures of Mixtures (SM4)

```
**Input:** Target distribution $p^*(s)$
Initialize policy $\pi_z(a \mid s)$, density model $q_z(s)$, discriminator $d(z \mid s)$, and replay buffer $\mathcal{B}$.
while not converged do
    for $z = 1, \cdots, n$ do
        $q_z^{(m)} \leftarrow \arg\max_q \mathbb{E}_{\{s \mid (z',s) \sim \mathcal{B}^{(m-1)}, z'=z\}} [\log q(s)]$
    $d^{(m)} \leftarrow \arg\max_d \mathbb{E}_{(z,s) \sim \mathcal{B}^{(m-1)}} [\log d(z \mid s)]$ {(2) Update discriminator.}
    for $z = 1, \cdots, n$ do
        $r_z^{(m)}(s) \triangleq \log p^*(s) - \log q_z^{(m)}(s) + \log d^{(m)}(z \mid s) - \log p(z)$
        $\pi_z^{(m)} \leftarrow \arg\max_\pi \mathbb{E}_{\rho_\pi(s)} \left[ r_z^{(m)}(s) \right]$
    Sample latent skill $z^{(m)} \sim p(z)$
    Sample transitions $\{(s_t, a_t, s_{t+1})\}_{t=1}^T$ with $\pi_z^{(m)}(a \mid s)$
    $\mathcal{B}^{(m)} \leftarrow \mathcal{B}^{(m-1)} \cup \{(z^{(m)}, s_t, a_t, s_{t+1})\}_{t=1}^T$
return $\{\{\pi_1^{(1)}, \cdots, \pi_n^{(1)}\}, \cdots, \{\pi_1^{(m)}, \cdots, \pi_n^{(m)}\}\}$
```

Alg. 2: An algorithm for learning a *mixture* of policies $\pi_1, \pi_2, \cdots, \pi_n$ that do state marginal matching *in aggregate*. The algorithm (1) fits a density model $q_z^{(m)}(s)$ to approximate the state marginal distribution for each policy π_z; (2) learns a discriminator $d^{(m)}(z \mid s)$ to predict which policy π_z will visit state s; and (3) uses RL to update each policy π_z to maximize the expected return of its corresponding reward function derived in Eq. 2.3. In our implementation, the density model $q_z(s)$ is a VAE that inputs the concatenated vector $\{s, z\}$ of the state s and the latent skill z used to obtain this sample s; and the discriminator is a feedforward MLP. The algorithm returns the historical average of mixtures of policies (a total of $n \cdot m$ policies).

Proposition 2.2.1. *Let policies Π and density models Q satisfying Assumption 1 be given. For any target distribution p^*, the following optimization problems are equivalent:*

$$\max_\pi \mathbb{E}_{\rho_\pi(s)}[\log p^*(s) - \log \rho_\pi(s)] = \max_\pi \min_q \quad \mathbb{E}_{\rho_\pi(s)}[\log p^*(s) - \log q(s)] \tag{2.4}$$

Proof of Proposition 2.2.1. Note that the objective in Eq. 2.4 can be written as

$$\mathbb{E}_{\rho_\pi(s)}[\log p^*(s) - \log \rho_\pi(s)] + D_{\mathrm{KL}}(\rho_\pi(s) \parallel q(s)).$$

By Assumption 1, $D_{\mathrm{KL}}(\rho_\pi(s) \parallel q(s)) = 0$ for some $q \in Q$, so we obtain the desired result:

$$\begin{aligned} &\max_\pi \left(\min_q \mathbb{E}_{\rho_\pi(s)}[\log p^*(s) - \log q(s)] \right) \\ &= \max_\pi \left(\mathbb{E}_{\rho_\pi(s)}[\log p^*(s) - \log \rho_\pi(s)] + \min_q D_{\mathrm{KL}}(\rho_\pi(s) \parallel q(s)) \right) \\ &= \max_\pi \mathbb{E}_{\rho_\pi(s)}[\log p^*(s) - \log \rho_\pi(s)]. \end{aligned}$$ □

Solving the new max-min optimization problem is equivalent to finding the Nash equilibrium of a two-player, zero-sum game: a *policy player* chooses the policy π while the *density player* chooses the density model q. To avoid confusion, we use *actions* to refer to controls $a \in \mathcal{A}$ output by the policy π in the traditional RL problem and *strategies* to refer to the decisions of the policy player $\pi \in \Pi$ and density player $q \in Q$. The Nash existence theorem [Nash, 1951] proves that such a stationary point always exists for such a two-player, zero-sum game.

One common approach to saddle point games is to alternate between updating player A w.r.t. player B, and updating player B w.r.t. player A. However, games such as Rock-Paper-Scissors illustrate that such a greedy approach is not guaranteed to converge to a stationary point. A slight variant, *fictitious play* [Brown, 1951] does converge to a Nash equilibrium in finite time [Robinson, 1951, Daskalakis and Pan, 2014]. At each iteration, each player chooses their best strategy in response to the *historical average* of the opponent's strategies. In our setting, fictitious play alternates between fitting the density model to the historical average of policies $\bar{\rho}_m(s) \triangleq \frac{1}{m} \sum_{i=1}^m \rho_{\pi_i}(s)$ (Eq. 2.5), and updating the policy with RL to minimize the log-density of the state, using a historical average of the density models $\bar{q}_m(s) \triangleq \frac{1}{m} \sum_{i=1}^m q_i(s)$ (Eq. 2.6):

$$q_{m+1} \leftarrow \arg\max_q \mathbb{E}_{s \sim \bar{\rho}_m(s)}[\log q(s)] \tag{2.5}$$

$$\pi_{m+1} \leftarrow \arg\max_\pi \mathbb{E}_{s \sim \rho_\pi(s)}[\log p^*(s) - \log \bar{q}_m(s)] \tag{2.6}$$

Crucially, the exploration policy is not the last policy, π_{m+1}, but rather the historical average policy:

Problem Statement. A *historical average policy* $\bar{\pi}(a \mid s)$, parametrized by a collection of policies $\pi_1, \cdots, \pi_m$, is a policy that randomly samples one of the policy iterates $\pi_i \sim \text{Unif}[\pi_1, \cdots, \pi_m]$ at the start of each episode and takes actions according to that policy in the episode.

We summarize the resulting algorithm in Alg. 1. In practice, we can efficiently implement Eq. 2.5 and avoid storing the policy parameters from every iteration by instead storing sampled states from each iteration. Alg. 1 looks similar to prior exploration methods based on prediction-error, suggesting that we might use SMM to understand how these prior methods work (Sec 2.3).

2.2.2 Extension to Mixtures of Policies

We refer to the algorithm with mixture modelling as SM4 (State Marginal Matching with Mixtures of Mixtures), and summarize the method in Alg. 2 in the Appendix. The algorithm (1) fits a density model $q_z^{(m)}(s)$ to approximate the state marginal distribution for each policy π_z; (2) learns a discriminator $d^{(m)}(z \mid s)$ to predict which policy π_z will visit state s; and (3) uses RL to update each policy π_z to maximize the expected return of its corresponding reward function $r_z(s)$ derived in Eq. 2.3.

The only difference from Alg. 1 is that we learn a discriminator $d(z \mid s)$, in addition to updating the density models $q_z(s)$ and the policies $\pi_z(a \mid s)$. Jensen's inequality tells us that maximizing the log-density of the learned discriminator will maximize a lower bound on the true density (see Agakov [2004]):

$$\mathbb{E}_{\substack{s \sim \rho_{\pi_z}(s), \\ z \sim p(z)}}[\log d(z \mid s)] \leq \mathbb{E}_{s \sim \rho_{\pi_z}(s), z \sim p(z)}[\log p(z \mid s)]$$

The algorithm returns the historical average of mixtures of policies (a total of $n \cdot m$ policies). Note that updates for each z can be conducted in parallel.

	inputs	targets	prior
SMM (Ours)	s	s	✓
RND	s	$e(s)$	✗
Forward Models	s, a	s'	✗
Inverse Models	s, s'	a	✗

Table 2.1: **Exploration based on predictive-error**: A number of exploration methods operate by learning a function that predicts some target quantity given some input quantities, and using this function's error as an exploration bonus. Previous methods have omitted the prior term, which our method implicitly incorporates via historical averaging.

2.3 Prediction-Error Exploration is Approximate State Marginal Matching

This section compares and contrasts SMM with prior exploration methods that use predictive-error, showing that these methods approximately optimize the same SMM objective when averaged over time, but otherwise exhibits oscillatory learning dynamics. Both the objectives and the optimization procedures are similar, but contain important yet subtle differences.

Objectives As introduced in Proposition 2.2.1, the state marginal matching objective can be viewed as a min-max objective (Eq. 2.4). When the density model is a VAE and the target distribution $p^*(s)$ is uniform, this min-max objective looks like the prediction error between a state and itself, plus a regularizer:

$$\max_{\pi} \min_{\psi} \mathbb{E}_{\rho_\pi(s)} \left[\|f_\psi(s_t) - s_t\|_2^2\right] + R_\pi(\psi),$$

where f_ϕ is our autoencoder and $R_\pi(\psi)$ is the KL penalty on the VAE encoder for the data distribution $\rho_\pi(s)$. Prior exploration methods look quite similar. For example, Exploration methods based on predictive error also optimize a min-max objective. For example, the objective for RND [Burda et al., 2018] is

$$\max_{\pi} \min_{\psi} \mathbb{E}_{\rho_\pi(s)} \left[\|f_\psi(s_t) - e(s_t)\|_2^2\right],$$

where $e(\cdot)$ is an encoder obtained by a randomly initialized neural network. Exploration bonuses based on the predictive error of forward models [Schmidhuber, 1991, Chentanez et al., 2005, Stadie et al., 2015] have a similar form, but instead consider full transitions:

$$\max_{\pi} \min_{\psi} \mathbb{E}_{\rho_\pi(s)} \left[\|f_\psi(s_t, a_t) - s_{t+1}\|_2^2\right].$$

Exploration bonuses derived from inverse models [Pathak et al., 2017] look similar:

$$\max_{\pi} \min_{\psi} \mathbb{E}_{\rho_\pi(s)} \left\|f_\psi(s_t, s_{t+1}) - a_t\|_2^2\right].$$

We summarize these methods in Table 2.1. We believe that the prior term $R(\psi)$ in the SMM objective (Eq. 2.3) that is omitted from the other objectives possibly explains why SMM continues to explore at convergence.

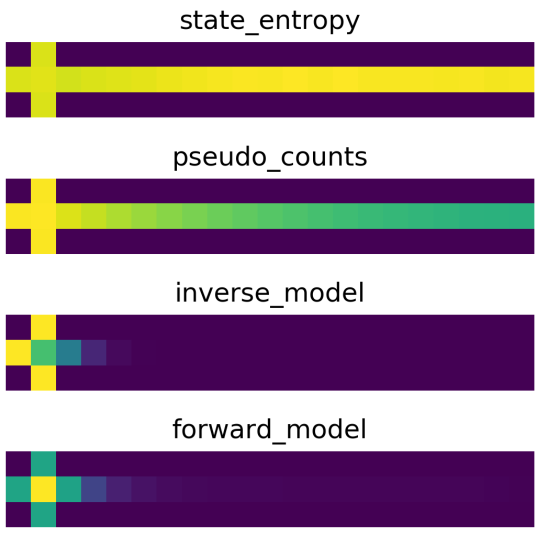

(a) State Marginals

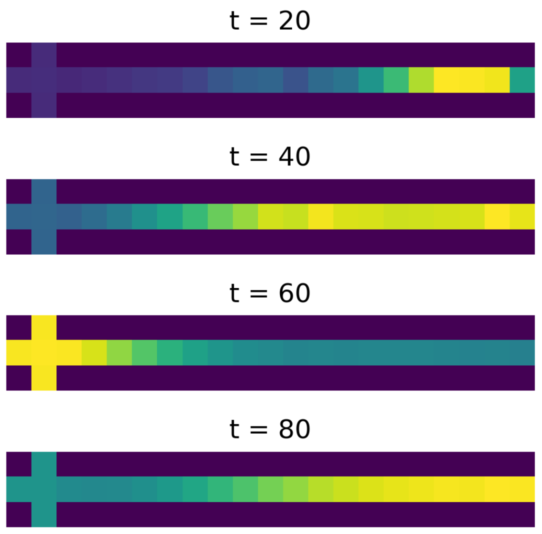

(b) Oscillatory Learning

Figure 2.2: Gridworld environment with a "noisy TV" state at the intersection of the two hallways (see Section 2.3.1). *(Left)* State Marginals of various exploration methods. *(Right)* Without historical averaging, two-player games exhibit oscillatory learning dynamics.

Optimization Both SMM and prior exploration methods employ alternating optimization to solve their respective min-max problems. Prior work uses a greedy procedure that optimizes the policy w.r.t. the *current* auxiliary model, and optimizes the auxiliary model w.r.t. the *current* policy. This greedy procedure often fails to converge, as we demonstrate experimentally in Section 2.3.1. In contrast, SMM uses fictitious play, a slight modification that optimizes the policy w.r.t. the *historical average* of the auxiliary models and optimizes the auxiliary model w.r.t. the *historical average* of the policies. Unlike the greedy approach, fictitious play is guaranteed to converge. This difference may explain why SMM learns better exploratory policies than prior methods.

While prior works use a procedure that is not guaranteed to converge, they nonetheless excel at solving hard exploration tasks. We draw an analogy to fictitious play to explain their success. While these methods never acquire an exploratory policy, over the course of training they will eventually visit all states. In other words, the *historical average* over policies will visit a wide range of states. Since the replay buffer exactly corresponds to this historical average over states, these methods will obtain a replay buffer with a diverse range of experience, possibly explaining why they succeed at solving hard exploration tasks. Moreover, this analysis suggests a surprisingly simple method for obtaining an exploration from these prior methods: use a mixture of the policy iterates throughout training. The following section will not only compare SMM against prior exploration methods, but also show that this historical averaging trick can be used to improve existing exploration methods.

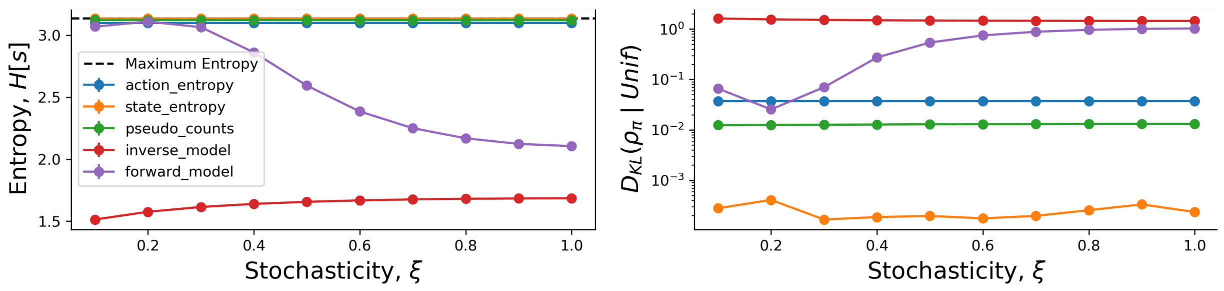

Figure 2.3: **Effect of Environment Stochasticity on Exploration**: We record the amount of exploration in the didactic gridworld environment as we increase the stochasticity of the dynamics. Both subplots were obtained from the same trajectory data.

2.3.1 Didactic Experiments

In this section, we build intuition for why SMM is an important improvement on top of existing exploration methods, and why historical averaging is an important ingredient in maximizing the SMM objective. We will consider the gridworld shown in Fig 2.2a. In each state, the agent can move up/down/left/right. In most states the commanded action is taken with probability 0.1; otherwise a random action is taken. The exception is a "noisy TV" state at the intersection of the two hallways, where the stochasticity is governed by a hyperparameter $\xi \in [0, 1]$. The motivation for considering this simple environment is that we can perform value iteration and learn forward/inverse/density models exactly, allowing us to observe the behavior of exploration strategies in the absence of function approximation error.

In our first experiment, we examine the asymptotic behavior of four methods: SMM (state entropy), inverse models, forward models, count-based exploration, and MaxEnt RL (action entropy). Fig. 2.2a shows that while SMM converges to a uniform distribution over states, other exploration methods are biased towards visiting the stochastic state on the left. To further understand this behavior, we vary the stochasticity of this state and plot the marginal state entropy of each method, which we compute exactly via the power method. Fig. 2.3 shows that SMM achieves high state entropy in all environments, whereas the marginal state entropy of the inverse model *decreases* as the environment stochasticity increases. The other methods fail to achieve high state entropy for all environments.

Our second experiment examines the role of historical averaging (HA). Without HA, we would expect that exploration methods involving a two-player game, such as SMM and predictive-error exploration, would exhibit oscillatory learning dynamics. Fig. 2.2b demonstrates this: without HA, the policy player and density player alternate in taking actions towards and placing probability mass on the left and right halves of the environment. Recalling that Fig. 2.2a included HA for SMM, we conclude that HA is an important ingredient for preventing oscillatory learning dynamics.

In summary, this didactic experiment illustrates that prior methods fail to perform uniform exploration, and that historical averaging is important for preventing oscillation. Our next experiments will show that SMM also accelerates exploration on complex, high-dimensional tasks.

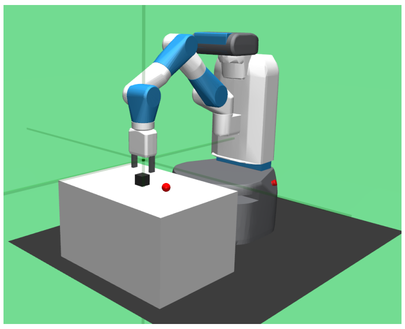

(a) *Fetch* environment

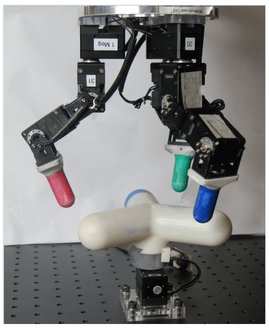

(b) *D'Claw* robot

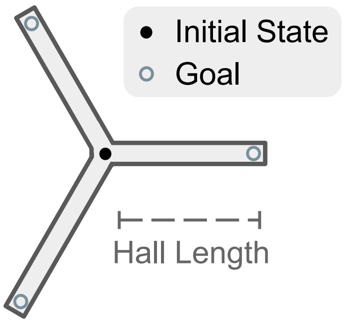

(c) *Navigation* env.

Figure 2.4: **Environments**: We ran experiments in both a simulated and real-world manipulation environments **(a-b)**, as well as a pointmass navigation environment **(c)**. In the *Navigation* environment, a point-mass agent is spawned at the center of m long hallways that extend radially outward, and the target state distribution places uniform probability mass $\frac{1}{m}$ at the end of each hallway. We can vary the length of the hallway and the number of hallways to control the task difficulty.

2.4 Experimental Evaluation

In this section, we empirically study whether our method learns to explore effectively when scaled to more complex RL benchmarks, and compare against prior exploration methods. Our experiments demonstrate how State Marginal Matching provides good exploration, a key component of which is the historical averaging step.

We compare to a state-of-the-art off-policy MaxEnt RL algorithm, Soft Actor-Critic (SAC) [Haarnoja et al., 2018]; an inverse RL algorithm, Generative Adversarial Imitation Learning (GAIL) [Ho and Ermon, 2016]; and three exploration methods:

- Count-based Exploration (Count), which discretizes states and uses $-\log \hat{\pi}(s)$ as an exploration bonus.
- Pseudo-counts (PC) [Bellemare et al., 2016], which uses the recoding probability as a bonus.
- Intrinsic Curiosity Module (ICM) [Pathak et al., 2017], which uses prediction error as a bonus.

All exploration methods have access to exactly the same information and the same extrinsic reward function. SMM interprets this extrinsic reward as the log probability of a target distribution: $p^*(s) \propto \exp(r_{\text{env}}(s))$.

We used SAC as the base RL algorithm for all exploration methods (SMM, Count, PC, ICM). For all algorithms, we use a Gaussian policy with two hidden layers with Tanh activation and a final fully-connected layer. The Value function and Q-function each are a feedforward MLP with two hidden layers with ReLU activation and a final fully-connected layer. Each hidden layer is of size 300 (SMM, SAC, ICM, C, PC) or 256 (GAIL). The same network configuration is used for the SMM discriminator, $d(z \mid s)$, and the GAIL discriminator, but with different input and output sizes.

We use a variational autoencoder (VAE) to model the density $q(s)$ for both SMM and Pseudocounts. The VAE encoder and decoder networks each consist of two hidden layers of size (150, 150) with ReLU activation.

In our SMM implementation, we estimated the density of data x as $p(x) \approx \text{decoder}(\hat{x} = x | z = \text{encoder}(x))$. That is, we encoded x to z, reconstruction $\hat{x}$ from z, and then took the likelihood of the true data x under a unit-variance Gaussian distribution centered at the reconstructed $\hat{x}$. The log-likelihood is therefore given by the mean-squared error between the data x and the reconstruction $\hat{x}$, plus a constant that is independent of x: $\log q(x) = \frac{1}{2}\|x - \hat{x}\|_2^2 + C$.

For SMM, we approximate the historical average of density models (Eq. 2.6) with the most recent iterate, and use a uniform categorical distribution for the prior $p(z)$. To train GAIL, we generated synthetic expert data by sampling expert states from the target distribution $p^*(s)$. Results for all experiments are averaged over 4-5 random seeds. Additional details about the experimental setup can be found in Appendix A.1.

2.4.1 Environments

We ran experiments in various manipulation and navigation environments, shown in Fig 2.4. We summarize the environments and the target state marginal distributions below.

Fetch. We used a simulated *Fetch* environment [Plappert et al., 2018] consisting of a single gripper arm and a block object on top of the table (Fig. 2.4a). The state vector $s \in \mathbb{R}^{28}$ includes the xyz-coordinates $s_{\text{obj}}, s_{\text{robot}} \in \mathbb{R}^3$ of the block and the robot gripper respectively, as well as their velocities, orientations, and relative position $s_{\text{obj}} - s_{\text{robot}}$. At the beginning of each episode, we spawn the object at the center of the table, and the robot gripper above the initial block position. We terminate each episode after 50 environment steps, or if the block falls off the table.

We considered two target state marginal distributions. In *Fetch-Uniform*, we defined the target distribution to be uniform over the entire state space (joint + block configuration), with the constraints that we put low probability mass on states where the block has fallen off the table; that actions should be small; and that the arm should be close to the object. The target density is given by

$$p^*(s) \propto \exp\left(\alpha_1 r_{\text{goal}}(s) + \alpha_2 r_{\text{robot}}(s) + \alpha_3 r_{\text{action}}(s)\right)$$

where $\alpha_1, \alpha_2, \alpha_3 > 0$ are fixed weights, and the rewards

$$\begin{aligned} r_{\text{goal}}(s) &:= 1 - \mathbb{1}(s_{\text{obj}} \text{ is on the table surface}) \\ r_{\text{robot}}(s) &:= \mathbb{1}(\|s_{\text{obj}} - s_{\text{robot}}\|_2^2 < 0.1) \\ r_{\text{action}}(s) &:= -\|a\|_2^2 \end{aligned}$$

correspond to (1) a uniform distribution of the block position over the table surface (the agent receives +0 reward while the block is on the table), (2) an indicator reward for moving the robot gripper close to the block, and (3) action penalty, respectively. The environment reward is a weighted sum of the three reward terms: $r_{\text{env}}(s) \triangleq 20 r_{\text{goal}}(s) + r_{\text{robot}}(s) + 0.1 r_{\text{action}}(s)$. At test-time, we sample a goal block location $g \in \mathbb{R}^3$ uniformly on the table surface, and the goal is not observed by the agent.

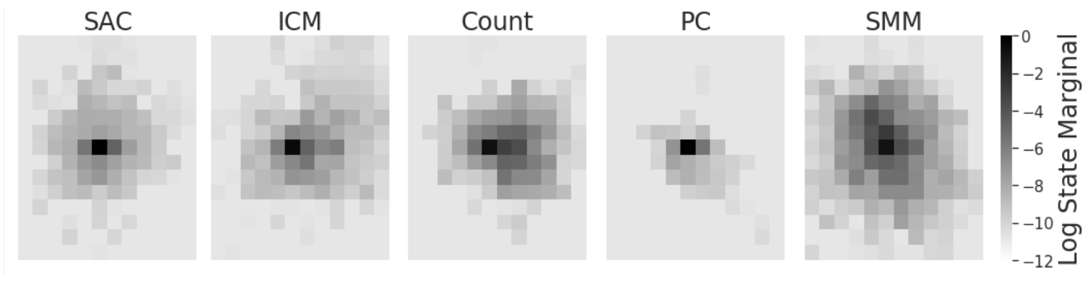

Figure 2.5: After training, we visualize the policy's log state marginal over the object coordinates in *Fetch*. SMM achieves wider state coverage than baselines.

In *Fetch-Half*, the target state density places higher probability mass to states where the block is on the left-side of the table. This is implemented by replacing $r_{\text{goal}}(s)$ with a reward function that gives a slightly higher reward $+0.1$ for states where the block is on the left-side of the table.

D'Claw. The *D'Claw* robot [Ahn et al., 2019]controls three claws to rotate a valve object (Fig. 2.4b). The environment consists of a 9-dimensional action space (three joints per claw) and a 12-dimensional observation space that encodes the joint angles and object orientation. We fixed each episode at 50 timesteps, which is about 5 seconds on the real robot. In the hardware experiments, each algorithm was trained on the same four *D'Claw* robots to ensure consistency.

We defined the target state distribution to place uniform probability mass over all object angles in $[-180°, 180°]$. It also incorporates reward shaping terms that place lower probability mass on states with high joint velocity and on states with joint positions that deviate far from the initial position (see [Zhu et al., 2019]).

Navigation: A point-mass agent is spawned at the center of m long hallways that extend radially outward, and the target state distribution places uniform probability mass $\frac{1}{m}$ at the end of each hallway (Fig. 2.4c). We can procedurally control the complexity of the environment by varying the hall length and the number of halls. Episodes have a maximum time horizon of 100 steps. The environment reward is

$$r_{\text{env}}(s) = \begin{cases} p_i & \text{if } \|s_{\text{robot}} - g_i\|_2^2 < \epsilon \text{ for any } i \in [n] \\ 0 & \text{otherwise} \end{cases}$$

where s_{xy} is the xy-position of the agent. We used a uniform target distribution over the end of all m halls, so the environment reward at training time is $r_{\text{env}}(s) = \frac{1}{m}$ if the robot is close enough to the end of any of the halls.

We used a fixed hall length of 10 in Figures 2.9a and 2.9b, and length 50 in Fig. 2.9c. All experiments used $m = 3$ halls, except in Fig. 2.9b where we varied the number of halls $\{3, 5, 7\}$.

2.4.2 State Coverage at Convergence

In the *Fetch* environment, we trained each method for 1e6 environment steps and then measured how well they explore by computing the marginal state entropy, which we compute by discretizing the state space.[2] In Fig. 2.6a, we see that SMM maximizes state entropy at least as effectively

[2]Discretization is used only for evaluation, no policy has access to it (except for Count).

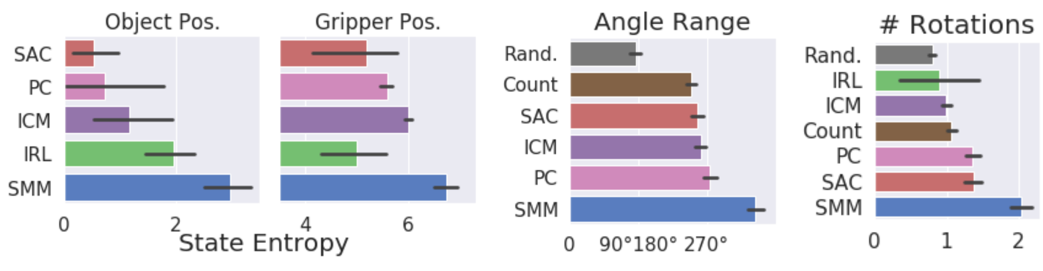

(a) *Fetch* environment (b) Sim2Real on *D'Claw*

Figure 2.6: **The Exploration of SMM: (a)** In the *Fetch* environment, we plot the policy's state entropy over the object and gripper coordinates, averaged over 1,000 epochs. SMM explores more than baselines, as indicated by the larger state entropy (larger is better). **(b)** In the *D'Claw* environment, we trained policies in simulation and then observed how far the trained policy rotated the knob on the hardware robot, measuring both the total number of rotations and the minimum and maximum valve rotations. SMM turns the knob further to the left and right than the baselines, and also completes a larger cumulative number of rotations.

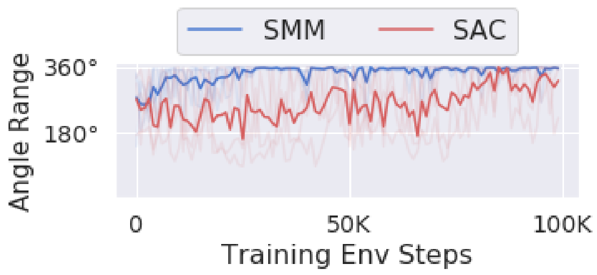

Figure 2.7: **Training on Hardware (*D'Claw*)**: We trained SAC and SMM on the real robot for 1e5 environment steps (about 9 hours in real time), and measured the angle turned throughout training. We see that SMM moves the knob more and visits a wider range of states than SAC. All results are averaged over 4-5 seeds.

as prior methods, if not better. While this comparison is somewhat unfair, as we measure exploration using the objective that SMM maximizes, none of the methods we compare against propose an alternative metric for exploration.

On the *D'Claw* robot, we trained SMM and other baselines in simulation, and then evaluated the acquired exploration policy on the real robot using two metrics: the total number of rotations (in either direction), and the maximum radians turned (in both directions). For each method, we computed the average metric across 100 evaluation episodes. We repeated this process for 5 independent training runs. Compared to the baselines, SMM turns the knob more to a wider range of angles (Fig. 2.6b). To test for statistical significance, we used a 1-sided Student's t-test to test the hypothesis that SMM turned the knob more to a wider range of angles than SAC. The p-values were all less than 0.05: $p = 0.046$ for number of rotations, $p = 0.019$ for maximum clockwise angle, and $p = 0.001$ for maximum counter-clockwise angle. The results on the *D'Claw* hardware robot suggests that exploration techniques may actually be useful in the real world, which may encourage future work to study exploration methods on real-world tasks.

We also investigated whether it was possible to learn an exploration policy directly in the real world, without the need for a simulator, an important setting in scenarios where faithful simulators are hard to build. In Fig. 2.7, we plot the range of angles that the policy explores

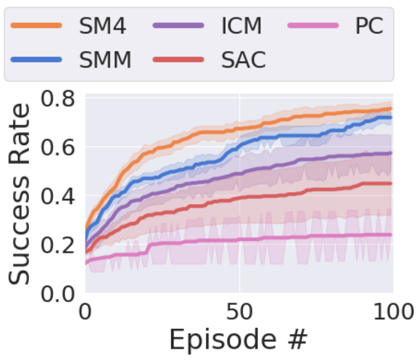

(a) Test-time adaptation

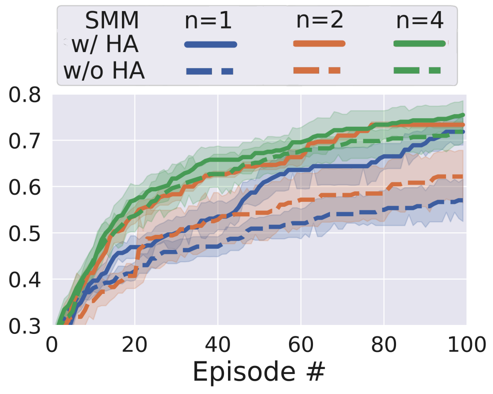

(b) SMM ablation

Figure 2.8: **Fast Adaptation**: **(a)** We plot the percentage of test-time goals found within N episodes. SMM and its mixture-model variant SM4 both explore faster than the baselines, allowing it to successfully find the goal in fewer episodes. **(b)** We compare SMM/SM4 with different numbers of mixtures, and with vs. without historical averaging. Increasing the number of latent mixture components $n \in \{1, 2, 4\}$ accelerates exploration, as does historical averaging. Error bars show std. dev. across 4 random seeds.

throughout training. Not only does SMM explore a wider range of angles than SAC, but its ability to explore increases throughout training, suggesting that the SMM objective is correlated with real-world metrics of exploration.

2.4.3 Test-time Exploration

We also evaluated whether the exploration policy acquired by SMM allows us to solve downstream tasks more quickly. As shown in Fig. 2.8a, SMM and its mixture variant, SM4, both adapt substantially more quickly than other exploration methods, achieving a success rate 20% higher than the next best method, and reaching the same level of performance of the next baseline (ICM) in 4x fewer episodes.

Ablation Study. In Fig. 2.8b, we study the effect of mixture modelling on test-time exploration. After running SMM/SM4 with a uniform distribution, we count the number of episodes required to find an (unknown) goal state. We run each method for the same number of environment transitions; a mixture of three policies *does not* get to take three times more transitions. We find that increasing the number of mixture components increases the agents success. However, the effect was smaller when using historical averaging. Taken together, this result suggests that efficient exploration requires *either* historical averaging *or* mixture modelling, but might not need both. In particular, SMM without historical averaging attains similar performance as the next best baseline (ICM), suggesting that historical averaging is the key ingredient, while the particular choice of prediction error or VAE is less important.

2.4.4 Exploration in State Space vs. Action Space

Is exploration in state space (as done by SMM) better than exploration in action space (as done by MaxEnt RL, e.g., SAC)? To study this question, we implemented a *Navigation* environment, shown in Fig. 2.4c. To evaluate each method, we counted the number of hallways that the agent

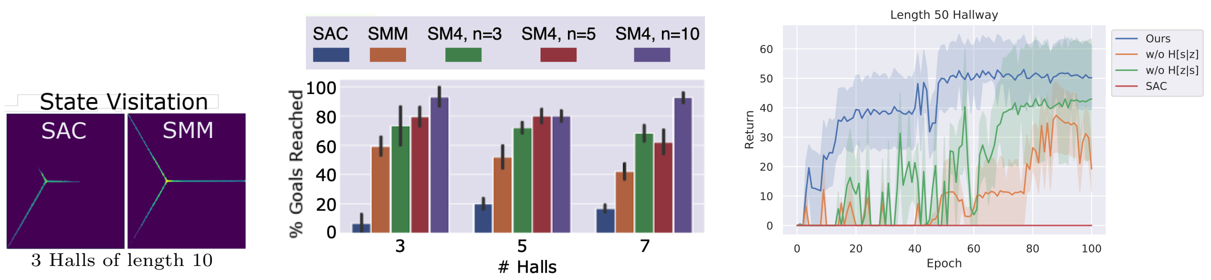

(a) $\rho_\pi(s)$ (b) % Goals reached during training (c) Train-time Performance

Figure 2.9: **Exploration in State Space (SMM) vs. Action Space (SAC) for *Navigation***: **(a)** A heatmap showing states visited by SAC and SMM during training illustrates that SMM explores a wider range of states. **(b)** SMM reaches more goals than the MaxEnt baseline. SM4 is an extension of SMM that incorporates mixture modelling with $n > 1$ skills (see Appendix 2.1.3), and further improves exploration of SMM. **(c)** **Ablation Analysis of SM4.** On the *Navigation* task, we compare SM4 (with three mixture components) against ablation baselines that lack conditional state entropy, latent conditional action entropy, or both (i.e., SAC) in the SM4 objective (Eq. 2.3). We see that both terms contribute heavily to the exploration ability of SM4, but the state entropy term is especially critical.

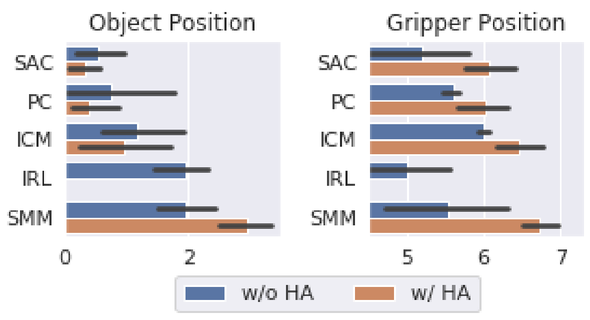

Figure 2.10: **With vs. Without Historical Averaging**: After training, we rollout the policy for 1e3 epochs, and record the entropy of the object and gripper positions in *Fetch*. SMM achieves higher state entropy than the other methods. Historical averaging also helps previous exploration methods achieve greater state coverage.

fully explored (i.e., reached the end) during training. Fig. 2.9a shows the state visitations for the three hallway environment, illustrating that SAC only explores one hallway, whereas SMM explores all three. Fig. 2.9b also shows that SMM consistently explores 60% of hallways, whereas SAC rarely visits more than 20% of hallways.

2.4.5 Does Historical Averaging help other baselines?

In Fig. 2.10, we see that historical averaging is not only beneficial to SMM, but also improves the exploration of prior methods. The result further supports our hypothesis that prior exploration methods are approximately optimizing the same SMM objective.

2.4.6 Non-Uniform Exploration

We check whether prior knowledge injected via the target distribution is reflected in the policy obtained from State Marginal Matching. Using the same *Fetch* environment as above, we modified the target distribution to assign larger probability to states where the block was on the left half

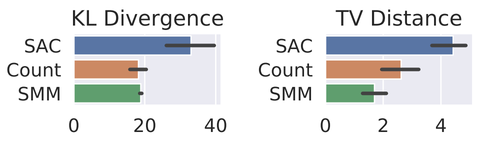

Figure 2.11: **Non-Uniform Exploration**: We measure the discrepancy between the state marginal distribution, $\rho_\pi(s)$, and a non-uniform target distribution. SMM matches the target distribution better than SAC and is on par with Count. Error bars show std. dev. across 4 random seeds.

of the table than on the right half. In Fig. 2.11, we measure whether SMM is able to achieve the target distribution by measuring the discrepancy between the block's horizontal coordinate and the target distribution. Compared to the SAC baseline, SMM and the Count baseline are half the distance to the target distribution. No method achieves zero discrepancy, suggesting that future methods could be better at matching state marginals.

2.4.7 SMM Ablation Study

To understand the relative contribution of each component in the SM4 objective (Eq. 2.3), we compare SM4 to baselines that lack conditional state entropy $\mathcal{H}_{\pi_z}[s] = -\log \rho_{\pi_z}(s)$, latent conditional action entropy $\log p(z \mid s)$, or both (i.e, SAC). In Fig. 2.9c, we plot the training time performance on the *Navigation* task with 3 halls of length 50. We see that SM4 relies heavily on both key differences from SAC.

2.4.8 Visualizing Mixture Components of SM4

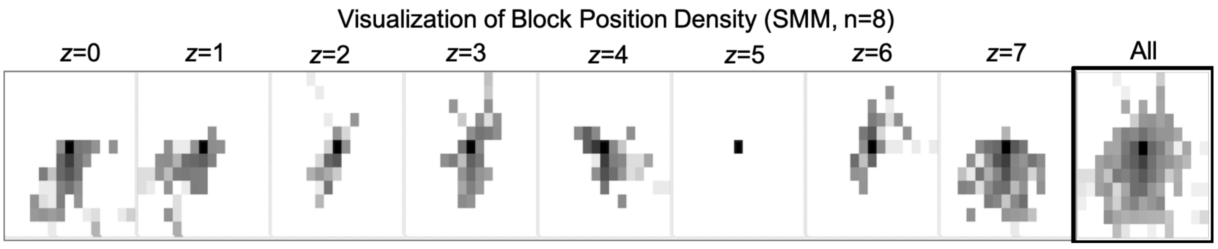

Figure 2.12: **SM4 with Eight Mixture Components**. In *Fetch*, we plot the log state marginal $\log \rho_{\pi_z}(s)$ over block XY-coordinates for each latent component $z \in \{0, \ldots, 7\}$, results are averaged over 1000 epochs.

In Fig. 2.12, we visualize the state marginals of each mixture component of SM4 for the *Fetch* task. The policy was trained using a uniform target distribution.

2.5 Choice of the Target Distribution for Goal-Reaching Tasks

In general, the choice of the target distribution $p^*(s)$ will depend on the distribution of test-time tasks. In this section, we consider the special case where the test-time tasks correspond to goal-reaching derive the optimal target distribution $p^*(s)$. We consider the setting where goals $g \sim p_g(g)$ are sampled from some known distribution. Our goal is to minimize the number of episodes required to reach that goal state. We define reaching the goal state as visiting a state that lies within an ϵ ball of the goal, where both $\epsilon > 0$ and the distance metric are known.

We start with a simple lemma that shows that the probability that we reach the goal at any state in a trajectory is at least the probability that we reach the goal at a randomly chosen state in that same trajectory. Defining the binary random variable $z_t \triangleq \mathbb{1}(\|s_t - g\| \le \epsilon)$ as the event that the state at time t reaches the goal state, we can formally state the claim as follows:

Lemma 2.5.1.

$$p\left(\sum_{t=1}^{T} z_t > 0\right) \ge p(z_{\mathbf{t}}) \qquad \textit{where} \quad \mathbf{t} \sim Unif[1, \cdots, H]$$

Proof. We start by noting the following implication:

$$z_{\mathbf{t}} = 1 \implies \sum_{t=1}^{T} z_t > 0$$

Thus, the probability of the event on the RHS must be at least as large as the probability of the event on the LHS:

$$p(z_{\mathbf{t}}) \le p\left(\sum_{t=1}^{T} z_t > 0\right)$$

□

Next, we look at the expected number of *episodes* to reach the goal state. Since each episode is independent, the expected hitting time is simply

$$\begin{aligned}\textsc{HittingTime}(s) &= \frac{1}{p(\text{some state reaches } s)} \\ &= \frac{1}{p\left(\sum_{t=1}^{T} z_t > 0\right)} \le \frac{1}{p(z_{\mathbf{t}})}\end{aligned}$$

Note that we have upper-bounded the hitting time using Lemma 2.5.1. Since the goal g is a random variable, we take an expectation over g:

$$\begin{aligned}\mathbb{E}_{s\sim p_g(s)}\left[\textsc{HittingTime}(s)\right] &\le \mathbb{E}_{s\sim p_g(s)}\left[\frac{1}{p(z_{\mathbf{t}})}\right] \\ &\le \mathbb{E}_{s\sim p_g(s)}\left[\frac{1}{\int p^*(\tilde{s})\mathbb{1}(\|s-\tilde{s}\| \le \epsilon)d\tilde{s}}\right] \triangleq \mathcal{F}(p^*)\end{aligned}$$

where $p^*(s)$ denotes the target state marginal distribution. We will minimize $\mathcal{F}$, an upper bound on the expected hitting time.

Lemma 2.5.2. *The state marginal distribution $p^*(s) \propto \sqrt{\tilde{p}(s)}$ minimizes $\mathcal{F}(p^*)$, where*

$$\tilde{p}(s) \triangleq \int p_g(\tilde{s})\mathbb{1}(\|s - \tilde{s}\| \le \epsilon)d\tilde{s}$$

is a smoothed version of the target density.

Before presenting the proof, we provide a bit of intuition. In the case where $\epsilon \to 0$, the optimal target distribution is $p^*(s) \propto \sqrt{p_g(s)}$. For non-zero ϵ, the policy in Lemma 2.5.2 is equivalent to convolving $p_g(s)$ with a box filter before taking the square root. In both cases, we see that the optimal policy does distribution matching to some function of the goal distribution. Note that $\tilde{p}(\cdot)$ may not sum to one and therefore is not a proper probability distribution.

Proof. We start by forming the Lagrangian:

$$\mathcal{L}(p^*) \triangleq \int \frac{p_g(s)}{\int p^*(\tilde{s}) \mathbb{1}(\|s - \tilde{s}\| \le \epsilon) \, d\tilde{s}} \, ds \\ + \lambda \left(\int p^*(\tilde{s}) \, d\tilde{s} - 1 \right)$$

The first derivative is

$$\frac{d\mathcal{L}}{dp^*(\tilde{s})} = \int \frac{-p_g(s)\mathbb{1}(\|s - \tilde{s}\| \le \epsilon)}{p^{*2}(\tilde{s})} ds + \lambda = 0$$

Note that the second derivative is positive, indicating that this Lagrangian is convex, so all stationary points must be global minima:

$$\frac{d^2\mathcal{L}}{dp^*(\tilde{s})^2} = \int \frac{2p_g(s)\mathbb{1}(\|s - \tilde{s}\| \le \epsilon)}{p^{*3}(\tilde{s})} ds > 0$$

Setting the first derivative equal to zero and rearranging terms, we obtain

$$\pi(\tilde{s}) \propto \sqrt{\int p_g(s) \mathbb{1}(\|s - \tilde{s}\| \le \epsilon) ds}$$

Renaming $\tilde{s} \leftrightarrow s$, we obtain the desired result. □

2.5.1 Connections to Goal-Conditioned RL

Goal-Conditioned RL [Kaelbling, 1993, Nair et al., 2018, Held et al., 2017] can be viewed as a special case of State Marginal Matching when the goal-sampling distribution is learned jointly with the policy. In particular, consider the State Marginal Matching with a mixture policy (Alg. 2), where the mixture component z maps bijectively to goal states. In this case, we learn goal-conditioned policies of the form $\pi(a \mid s, z)$. Consider the SMM objective with Mixtures of Policies in Eq. 2.3. The second term $p(z \mid s)$ is an estimate of which goal the agent is trying to reach, similar to objectives in intent inference [Ziebart et al., 2009, Xie et al., 2013]. The third term $\pi(s \mid z)$ is the distribution over states visited by the policy when attempting to reach goal z. For an optimal goal-conditioned policy in an infinite-horizon MDP, both of these terms are Dirac functions:

$$\pi(z \mid s) = \rho_\pi(s \mid z) = \mathbb{1}(s = z)$$

In this setting, the State Marginal Matching objective simply says to sample goals $g \sim \pi(g)$ with probability equal to the density of that goal under the target distribution.

$$D_{\mathrm{KL}}(\rho_\pi(s) \parallel p^*(s)) = \mathbb{E}_{\substack{z \sim \pi(z) \\ s \sim \pi(s|z)}} [\log p^*(s) - \log \pi(z)]$$

Whether goal-conditioned RL is the preferable way to do distribution matching depends on (1) the difficulty of sampling goals and (2) the supervision that will be provided at test time. It is natural to use goal-conditioned RL in settings where it is easy to sample goals, such as when the space of goals is small and finite or otherwise low-dimensional. If a large collection of goals is available apriori, we could use importance sampling to generate goals to train the goal-conditioned policy [Pong et al., 2019]. However, many real-world settings have high-dimensional goals, which can be challenging to sample. While goal-conditioned RL is likely the right approach when we will be given a test-time task, a latent-conditioned policy may explore better in settings where the goal-state is not provided at test-time.

2.6 Related Work

Many exploration algorithms can be classified by whether they explore in the space of actions, policy parameters, goals, or states. Common exploration strategies including ϵ-greedy and Ornstein–Uhlenbeck noise [Lillicrap et al., 2015], and MaxEnt RL algorithms [Ziebart, 2010, Haarnoja et al., 2018] explore in the action space. Fortunato et al. [2017], Plappert et al. [2017] show that adding parameter noise to the policy can result in good exploration.

Most closely related to our work are methods that perform exploration in the space of states or goals [Colas et al., 2018, Held et al., 2017, Nair et al., 2018, Pong et al., 2019, Hazan et al., 2018]. While the state marginal matching objective is also considered in Hazan et al. [2018], our work builds upon this prior work in a number of dimensions. First, we explain how to do distribution matching properly by analyzing the SMM objective as a two-player game and applying historical averaging from fictitious play. Our analysis also leads to a unified view of a large class of existing intrinsic motivation techniques that previously were proposed as exploration heuristics, showing that in fact these methods *almost* perform state marginal matching. Furthermore, we introduce the notion that this objective yields a task-agnostic "policy prior" that can quickly solve new tasks, and demonstrate this empirically on complex RL benchmarks. We also prove that the SMM objective induces the optimal exploration for a certain class of goal-reaching tasks (Appendix 2.5).

One class of exploration methods uses prediction error of some auxiliary task as an exploration bonus, which provides high (intrinsic) reward in states where the predictive model performs poorly [Pathak et al., 2017, Oudeyer et al., 2007, Schmidhuber, 1991, Houthooft et al., 2016, Burda et al., 2018]. Another set of approaches [Tang et al., 2017, Bellemare et al., 2016, Schmidhuber, 2010] directly encourage the agent to visit novel states. While all methods effectively explore during the course of solving a single task [Taïga et al., 2019], we showed in Sec. 2.3 that the policy obtained at convergence is often not a good exploration policy by itself. In contrast, our method converges to a highly-exploratory policy by maximizing state entropy.

The problems of exploration and meta-RL are tightly coupled. Meta-RL algorithms [Duan et al., 2016, Finn et al., 2017, Rakelly et al., 2019, Mishra et al., 2017] must perform effective exploration if they hope to solve a downstream task. Some prior work has explicitly looked at the problem of learning to explore [Gupta et al., 2018, Xu et al., 2018]. Our problem statement is similar to meta-learning, in that we also aim to learn a policy as a prior for solving downstream tasks. However, whereas meta-RL requires a distribution of task reward functions, our method requires only a single target state marginal distribution. Due to the simpler problem assumptions and training procedure, our method may be easier to apply in real-world domains.

Related to our approach are maximum *action* entropy algorithms [Haarnoja et al., 2018, Kappen et al., 2012, Rawlik et al., 2013, Ziebart et al., 2008, Theodorou and Todorov, 2012]. While these algorithms are referred to as *MaxEnt RL*, they are maximizing entropy over actions, not states. These algorithms can be viewed as performing inference on a graphical model where the likelihood of a trajectory is given by its exponentiated reward [Toussaint and Storkey, 2006, Levine, 2018, Abdolmaleki et al., 2018]. While distributions over trajectories induce distributions over states, computing the exact relationship requires integrating over all possible trajectories, an intractable problem for most MDPs. A related but distinct class of *relative* entropy methods use a similar entropy-based objective to limit the size of policy updates [Peters et al., 2010, Schulman et al., 2015].

Many of the underlying ingredients of our method, such as adversarial games and density estimation, have seen recent progress in imitation learning [Ziebart et al., 2008, Ho and Ermon, 2016, Finn et al., 2016a, Fu et al., 2017]. Similar to some inverse RL algorithms [Ho and Ermon, 2016, Fu et al., 2018a], our method iterates between learning a policy and learning a reward function, though our reward function is obtained via a density model instead of a discriminator. While inverse RL algorithms assume access to expert trajectories, we instead assume access to the density of the target state marginal distribution. In many realistic settings, such as robotic control with many degrees of freedom, providing fully-specified trajectories may be much more challenging than defining a target state marginal distribution. The latter only requires some aggregate statistics about expert behavior, and does not even need to be realizable by any policy.

2.7 Discussion

This work studied state marginal matching as a formal objective for exploration. While it is often unclear what existing exploration methods will converge to, the SMM objective has a clear solution: at convergence, the policy should visit states in proportion to their density under a target distribution. The resulting policy can be used as a prior in a multi-task setting to amortize exploration and adapt more quickly to new, potentially sparse, reward functions.

We explain how to perform distribution matching properly via historical averaging. We further demonstrate that prior work approximately maximizes the SMM objective, offering an explanation for the success of these methods. Augmenting these prior methods with an important historical averaging step not only guarantees that they converge, but also empirically improves their exploration. Experiments on both simulated and real-world tasks demonstrated how SMM learns to explore, enabling an agent to efficiently explore in new tasks provided at test time.

In summary, our work unifies prior exploration methods as performing approximate distribution matching, and explains how state distribution matching can be performed properly. This perspective provides a clearer picture of exploration, and is useful particularly because many of the underlying ingredients, such as adversarial games and density estimation, have seen recent progress and therefore might be adopted to improve exploration methods.

One limitation of many exploration algorithms, including state marginal matching, is the requirement of knowing a relatively low-dimensional state representation that informs the agent along which state dimensions it should explore. However, learning a good state representation requires data collected from a policy that does efficient exploration. This Catch-22 situation between exploration and representation learning remains an unsolved challenge in RL. In Chapter 3, we will look at how weakly-supervised representation learning can allow us to scalably learn a structured representation for better exploration and learning.

Chapter 3

Weakly-Supervised RL for Controllable Behavior

A general purpose agent must be able to efficiently learn a diverse array of tasks through interacting with the real world. The typical approach is to manually define a set of reward functions and only learn the tasks induced by these reward functions [Finn et al., 2017, Hausman et al., 2018]. However, defining and tuning the reward functions is labor intensive and places a significant burden on the user to specify reward functions for all tasks that they care about. Designing reward functions that provide enough learning signal yet still induce the correct behavior at convergence is challenging [Hadfield-Menell et al., 2017]. An alternative approach is to parametrize a family of tasks, such as goal-reaching tasks, and learn a policy for each task in this family [Hazan et al., 2018, Pong et al., 2019, Lee et al., 2019b, Ghasemipour et al., 2019, Stanley and Miikkulainen, 2002, Pugh et al., 2016]. However, learning a single goal-conditioned policy for reaching all goals is a challenging optimization problem and is prone to underfitting, especially in high-dimensional tasks with limited data [Dasari et al., 2019]. In this work, we aim to accelerate the acquisition of goal-conditioned policies by narrowing the goal space through weak supervision. Answering this question would allow an RL agent to prioritize exploring and learning meaningful tasks, resulting in faster acquisition of behaviors for solving human-specified tasks.

How might we constrain the space of tasks to those that are semantically meaningful? Reward functions and demonstrations are the predominant approaches to training RL agents, but they are expensive to acquire [Hadfield-Menell et al., 2017]. Generally, demonstrations require expert humans to be present [Finn et al., 2016a, Duan et al., 2017, Laskey et al., 2017], and it remains a challenge to acquire high-quality demonstration data from crowdsourcing [Mandlekar et al., 2018]. In contrast, human preferences and ranking schemes provide an interface for sources of supervision that are easy and intuitive for humans to specify [Christiano et al., 2017], and can scale with the collection of offline data via crowd-sourcing. However, if we are interested in learning many tasks rather than just one, these approaches do not effectively facilitate scalable learning of many different tasks or goals.

In this work, we demonstrate how weak supervision provides useful information to agents with minimal burden, and how agents can leverage that supervision when learning in an environment. We will study one approach to using weak supervision in the goal-conditioned RL setting [Kael-

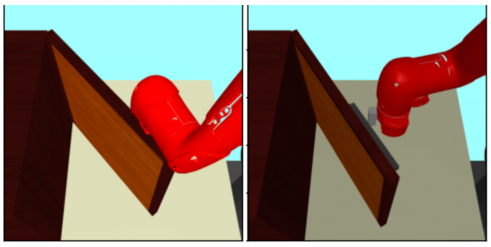
In which image...

1. ...is the door opened wider?
2. ...is the lighting brighter?
3. ...is the robot closer to the door?

Figure 3.1: We propose weak supervision as a means to scalably introduce structure into goal-conditioned RL. The weak supervision is provided by a human who answers true/false questions (right) based on the two images (left).

bling, 1993, Schaul et al., 2015, Andrychowicz et al., 2017, Pong et al., 2018, Nair et al., 2018]. Instead of exploring and learning to reach every goal state, our weakly-supervised agent need only learn to reach states along meaningful axes of variation, ignoring state dimensions that are irrelevant to solving human-specified tasks. Critically, we propose to place such constraints through weak forms of supervision, instead of enumerating goals or tasks and their corresponding rewards. This weak supervision is obtained by pairwise queries (see Figure 3.1), and our approach uses this supervision to learn a structured representation space of observations and goals, which can in turn be used to guide exploration, goal generation, and learning. Our approach enables the user to specify the axes of variation that matter for the efficient development of general-purpose agents, and implicitly characterize factors that are not relevant to human-specified tasks.

The main contribution of this work is *weakly-supervised control (WSC)*, a simple framework for introducing weak supervision into RL. Our approach learns a semantically meaningful representation space with which the agent can generate its own goals, acquire distance functions, and perform directed exploration. WSC consists of two stages: we first learn a disentangled representation of states from weakly-labeled offline data, then we use the disentangled representation to constrain the exploration space for RL agents. We empirically show that learning disentangled representations can speed up reinforcement learning on various manipulation tasks, and improve the generalization abilities of the learned RL agents. We also demonstrate that WSC produces an *interpretable* latent policy, where latent goals directly align with controllable features of the environment.

3.1 Preliminaries

In this section, we overview notation and prior methods that we build upon in this work.

3.1.1 Goal-conditioned reinforcement learning

We define a finite-horizon goal-conditioned Markov decision process by a tuple $(\mathcal{S}, \mathcal{A}, P, H, \mathcal{G})$ where $\mathcal{S}$ is the observation space, $\mathcal{A}$ is the action space, $P(s' \mid s, a)$ is an unknown dynamics function, H is the maximum horizon, and $\mathcal{G} \subseteq \mathcal{S}$ is the goal space. In goal-conditioned RL, we train a policy $\pi_\theta(a_t \mid s_t, g)$ to reach goals from the goal space $g \sim \mathcal{G}$ by optimizing the expected cumulative reward $\mathbb{E}_{g\sim\mathcal{G}, \tau\sim(\pi,P)}\left[\sum_{s\in\tau} R_g(s)\right]$, where $R_g(s)$ is a reward function defined by some distance metric between goals $g \in \mathcal{G}$ and observations $s \in \mathcal{S}$.

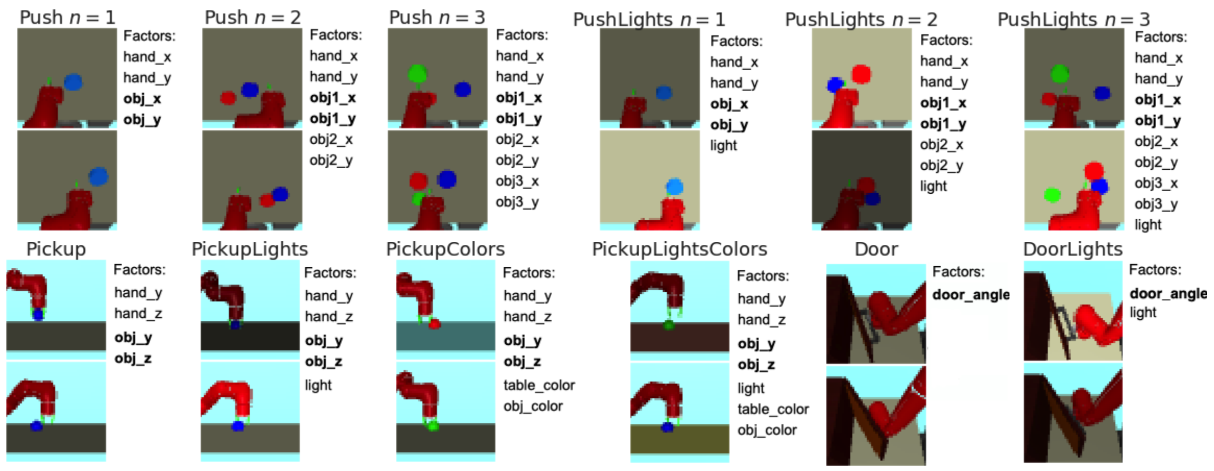
Push $n = 1$
Factors: hand_x hand_y **obj_x** **obj_y**
Push $n = 2$
Factors: hand_x hand_y **obj1_x** **obj1_y** obj2_x obj2_y
Push $n = 3$
Factors: hand_x hand_y **obj1_x** **obj1_y** obj2_x obj2_y obj3_x obj3_y
PushLights $n = 1$
Factors: hand_x hand_y **obj_x** **obj_y** light
PushLights $n = 2$
Factors: hand_x hand_y **obj1_x** **obj1_y** obj2_x obj2_y light
PushLights $n = 3$
Factors: hand_x hand_y **obj1_x** **obj1_y** obj2_x obj2_y obj3_x obj3_y light
Pickup
Factors: hand_y hand_z **obj_y** **obj_z**
PickupLights
Factors: hand_y hand_z **obj_y** **obj_z** light
PickupColors
Factors: hand_y hand_z **obj_y** **obj_z** table_color obj_color
PickupLightsColors
Factors: hand_y hand_z **obj_y** **obj_z** light table_color obj_color
Door
Factors: **door_angle**
DoorLights
Factors: **door_angle** light

Figure 3.2: Our method uses weak supervision, like that depicted in this figure, to direct exploration and accelerate learning on visual manipulation tasks of varying complexity. Each data sample consists of a pair of image observations $\{s_1, s_2\}$ and a factor label vector $y \in \{0,1\}^K$, where $y_k = \mathbf{1}(f_k(s_1) < f_k(s_2))$ indicates whether the kth factor of image s_1 has smaller value than that of image s_2. Example factors of variation include the gripper position, object positions, brightness, and door angle. Note that we only need to collect labels for the axes of variation that may be relevant for future downstream tasks (see Appendix 3.4.5). In environments with 'light' as a factor (e.g., *PushLights*), the lighting conditions change randomly at the start of each episode. In environments with 'color' as a factor (e.g., *PickupColors*), both the object color and table color randomly change at the start of each episode. Bolded factors correspond to the user-specified factor indices $\mathcal{I}$ indicating which of the factors are relevant for solving the class of tasks (see Sec. 3.2)

In low-dimensional tasks, one can simply take the reward to be the negative ℓ_2-distance in the state space [Andrychowicz et al., 2017]. However, defining distance metrics is more challenging in high-dimensional spaces, such as images [Yu et al., 2019]. Prior work on visual goal-conditioned RL [Nair et al., 2018, Pong et al., 2019] train an additional state representation model, such as a VAE encoder $e^{\text{VAE}} : \mathcal{S} \to \mathcal{Z}^{\text{VAE}}$. Their methods train a policy over encoded states and goals, and define rewards using ℓ_2-distance in latent space:

$$R_g(s) = -\|e^{\text{VAE}}(s) - e^{\text{VAE}}(g)\|_2^2.$$

3.1.2 Weakly-supervised disentangled representations

Our approach leverages weakly-supervised disentangled representation learning in the context of reinforcement learning. Disentangled representation learning aims to learn interpretable representations of data, where each dimension of the representation measures a distinct *factor of variation*, conditioned on which the data was generated (see Fig. 3.2 for examples of factors). More formally, consider data-generating processes where $(f_1, \ldots, f_K) \in \mathcal{F}$ are the factors of variation, and observations $s \in \mathcal{S}$ are generated from a function $g^* : \mathcal{F} \to \mathcal{S}$. We would like to learn a disentangled latent representation $e : \mathcal{S} \to \mathcal{Z}$ such that, for any factor subindices $\mathcal{I} \subseteq [K]$, the subset of latent values $e_{\mathcal{I}}(s) = z_{\mathcal{I}}$ are only influenced by the true factors $f_{\mathcal{I}}$, and conversely, $e_{\setminus \mathcal{I}}(s) = z_{\setminus \mathcal{I}}$ are only influenced by $f_{\setminus \mathcal{I}}$.

We consider a form of weak supervision called *rank pairing*, where data samples $\mathcal{D} := \{(s_1, s_2, y)\}$ consist of pairs of observations $\{s_1, s_2\}$ and weak binary labels $y \in \{0,1\}^K$, where

$y_k = \mathbf{1}(f_k(s_1) < f_k(s_2))$ indicates whether the kth factor value for observation s_1 is smaller than the corresponding factor value for s_2. Using this data, the weakly-supervised method proposed by Shu et al. [2019] trains an encoder $e : \mathcal{S} \to \mathcal{Z}$, generator $G : \mathcal{Z} \to \mathcal{S}$, and discriminator D by optimizing the following losses:

$$\begin{aligned}
&\min_D \quad \mathbb{E}_{(s_1,s_2,y)\sim\mathcal{D}}\left[D(s_1,s_2,y)\right] + \mathbb{E}_{z_1,z_2\sim N(0,I)}\left(1 - D(G(z_1),G(z_2),y^{\text{fake}})\right) \\
&\max_G \quad \mathbb{E}_{z_1,z_2\sim N(0,I)}\left[D(G(z_1),G(z_2),y^{\text{fake}})\right] \\
&\min_e \quad \mathbb{E}_{z\sim N(0,I)}\left[e(z \mid G(z))\right] \qquad (3.1)
\end{aligned}$$

Shu et al. [2019] showed that this approach is guaranteed to recover the true disentangled representation under mild assumptions. We build upon their work in two respects. First, while Shu et al. [2019] used a balanced and clean dataset, we extend the method to work on significantly less clean data – data from an agent's observations in a physical world. Second, we show how the learned representations can be used to accelerate RL.

3.2 The Weakly-Supervised RL Problem

Unlike standard RL, which requires hand-designed reward functions that are often expensive to obtain in complex environments, we aim to design the weakly-supervised RL problem in a way that provides a convenient form of supervision that scales with the collection of offline data. Further, we will require no labels in the loop of reinforcement learning, nor precise segmentations or numerical coordinates to be provided by the human.

Consider an environment with high complexity and large observation space such that it is intractable for an agent to explore the entire state space. Suppose that we have access to an offline dataset of weakly-labeled observations, where the labels capture semantically meaningful properties about the environment that are helpful to solving downstream tasks. How can a general-purpose RL agent leverage this dataset to learn new tasks faster? In this section, we formalize this problem statement.

Problem Statement. Assume we are given a weakly-labelled dataset $\mathcal{D} := \{(s_1, s_2, y)\}$, which consists of pairs of observations $\{s_1, s_2\}$ and weak binary labels $y \in \{0,1\}^K$, where $y_k = \mathbf{1}(f_k(s_1) < f_k(s_2))$ indicates whether the k-th factor value for observation s_1 is smaller than the corresponding factor value for s_2. Beyond these labels, the user also specifies a subset of indices, $\mathcal{I} \subseteq [K]$, indicating which of the factors $(f_1, \ldots, f_K) \in \mathcal{F}$ are relevant for solving a class of tasks. During training, the agent may interact with the environment, but receives no supervision (e.g. no rewards) beyond the weak labels in $\mathcal{D}$.

At test time, an unknown goal factor $f^*_{\mathcal{I}} \in \mathcal{F}_{\mathcal{I}}$ is sampled, and the agent receives a goal observation, e.g. a goal image, whose factors are equal to $f^*_{\mathcal{I}}$. The agent's objective is to learn a latent-conditioned RL policy that minimizes the goal distance: $\min_\pi \, \mathbb{E}_\pi \, d(f_{\mathcal{I}}(s), f^*_{\mathcal{I}})$.

The weakly-supervised RL problem formulated in this section is applicable in many real-world scenarios in which acquiring weak supervision is relatively cheap, e.g. through offline crowd compute, while acquiring demonstrations is expensive and rewards require expertise. For example,

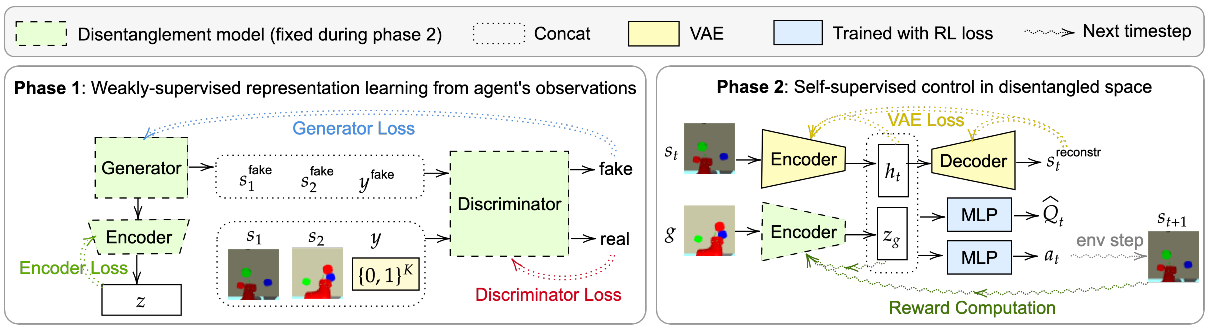

Figure 3.3: **Weakly-Supervised Control framework**. *Left*: In Phase 1, we use the weakly-labelled dataset $\mathcal{D} = \{(s_1, s_2, y)\}$ to learn a disentangled representation by optimizing the losses in Eq. 3.1. *Right*: In Phase 2, we use the learned disentangled representation to guide goal generation and define distances. At the start of each episode, the agent samples a latent goal z_g either by encoding a goal image g sampled from the replay buffer, or by sampling directly from the latent goal distribution (Eq. 3.2). The agent samples actions using the goal-conditioned policy, and defines rewards as the negative ℓ_2 distance between goals and states in the disentangled latent space (Eq. 3.3).

consider a vision-based robotic manipulation environment (Fig. 3.2). The labels in the dataset $\mathcal{D}$ could indicate the relative position of the robot gripper arm between two image observations. The goal factor space $\mathcal{F}_\mathcal{I}$ consists of XY-positions of the object that the agent should learn to move around. Note that we only need to collect labels for the axes of variation that may be relevant for future downstream tasks (see Appendix 3.4.5). At test time, the agent receives a goal image observation, and is evaluated on how closely it can move the object to the goal location.

The next section will develop a RL framework for solving the weakly supervised RL problem. Our experiments (Sec. 3.4) will investigate whether weak supervision is an economical way to accelerate learning on complex tasks.

3.3 Weakly-Supervised Control

In this section, we describe a simple training framework for the weakly-supervised RL problem. Our *weakly-supervised control (WSC)* framework consists of two stages: we first learn a disentangled representation from weakly-labelled RL observations, and then use this disentangled space to guide the exploration of goal-conditioned RL along semantically meaningful directions.

3.3.1 Learning disentangled representations from observations

We build upon the work of Shu et al. [2019] for learning disentangled representations, though, in principle other methods could be used. Their method trains an encoder $e : \mathcal{S} \to \mathcal{Z}$, generator $G : \mathcal{Z} \to \mathcal{S}$, and discriminator D by optimizing the losses in Eq. 3.1. After training the disentanglement model, we discard the discriminator and the generator, and use the encoder to define the goal space and compute distances between states.

While Shu et al. [2019] assumes that all combinations of factors are present in the dataset and that data classes are perfectly balanced (i.e., exactly one image for every possible combination of factors), these assumptions usually do not hold for significantly less clean data coming from an agent's observations in a physical world. For example, not all factor combinations are physically possible to achieve: an object cannot be floating in mid-air without a robot gripper holding it, and two solid objects cannot occupy the same space at the same time. This affects the data distribution: for example, when the robot is holding the object in *Pickup*, there is high correlation between the gripper and object positions. Another issue is partial observability: the agent may lack sensors to observe some aspects of its environment, such as being unable to see through occlusions.

To generate the Sawyer datasets shown in Fig. 3.2, we corrected the sampled factor combinations to be physically feasible before generating the corresponding image observations in the Mujoco simulator. Furthermore, to reflect the difficulty of collecting a large amount of samples in complex RL environments, we only sampled 256 or 512 images in the training dataset, which is much smaller than the combinatorial size of toy datasets such as dSprites [Matthey et al., 2017] (737,280 images).

Empirically, we found that it is more challenging to learn a disentangled representation on the Sawyer observations (see Table 3.2), yet we show in Sec. 3.4 that imperfect disentanglement models can still drastically accelerate training of goal-conditioned policies. In the next section, we describe how we use the learned disentangled space to generate goals, define reward functions, and do directed exploration.

3.3.2 Structured Goal Generation & Distance Function

In this section, we describe how our method uses the learned disentangled model $e : \mathcal{S} \to \mathcal{Z}$ and the user-specified factor indices $\mathcal{I} \subseteq [K]$ to train a goal-conditioned policy $\pi(a \mid s, z_g)$. The agent will propose its own goals to practice, attempt the proposed goals, and use the experience to update its goal-conditioned policy.

Our method defines the goal space to be the learned disentangled latent space $\mathcal{Z}_\mathcal{I}$, restricted to the indices in $\mathcal{I}$. The goal sampling distribution is defined as

$$p(\mathcal{Z}_\mathcal{I}) := \text{Uniform}(\mathcal{Z}_\mathcal{I}^{\min}, \mathcal{Z}_\mathcal{I}^{\max}), \tag{3.2}$$

where $\mathcal{Z}_\mathcal{I}^{\min} = \min_{s\in\mathcal{D}}\ e_\mathcal{I}(s)$ and $\mathcal{Z}_\mathcal{I}^{\max} = \max_{s\in\mathcal{D}}\ e_\mathcal{I}(s)$ denote the element-wise min and max latent values.

In each iteration, our method samples latent goals $z_g \in \mathcal{Z}_\mathcal{I}$ by either sampling from $p(\mathcal{Z}_\mathcal{I})$, or sampling an image observation from the replay buffer and encoding it with the disentangled model, $z_g = e_\mathcal{I}(s_g)$. Then, our method attempts this goal by executing the policy to get a trajectory $(s_1, a_1, ..., s_T)$. When sampling transitions (s_t, a_t, s_{t+1}, z_g) from the replay buffer for RL training, we use hindsight relabeling [Andrychowicz et al., 2017] with corrected goals to provide additional training signal. In other words, we sometimes relabel the transition $(s_t, a_t, s_{t+1}, z_g')$ with a corrected goal z_g', which is sampled from either the goal distribution $p(\mathcal{Z}_\mathcal{I})$ in Eq. 3.2, or from a future state in the current trajectory. Our method defines the reward function as the negative ℓ_2-distance in the disentangled latent space:

$$r_t := R_{z_g}(s_{t+1}) := -\|e_\mathcal{I}(s_{t+1}) - z_g\|_2^2. \tag{3.3}$$

We summarize our weakly-supervised control (WSC) framework in Fig. 3.3 and Alg. 3. We start by learning the disentanglement module using the weakly-labelled data. Next, we train the policy

Algorithm 3 Weakly-Supervised Control

```
Input: Weakly-labeled dataset $\mathcal{D}$, factor subindices $\mathcal{I} \subseteq [K]$
 1: Train disentangled representation $e : \mathcal{S} \mapsto \mathcal{Z}$ using $\mathcal{D}$.
 2: Compute $\mathcal{Z}_\mathcal{I}^{\min} = \min_{s \in \mathcal{D}} \; e_\mathcal{I}(s)$.
 3: Compute $\mathcal{Z}_\mathcal{I}^{\max} = \max_{s \in \mathcal{D}} \; e_\mathcal{I}(s)$.
 4: Define $p(\mathcal{Z}_\mathcal{I}) := \text{Uniform}(\mathcal{Z}_\mathcal{I}^{\min}, \mathcal{Z}_\mathcal{I}^{\max})$.
 5: Initialize replay buffer $\mathcal{R} \leftarrow \emptyset$.
 6: for iteration$= 0, 1, \ldots,$ do
 7:     Sample a goal $z_g \in \mathcal{Z}$ and an initial state $s_0$.
 8:     for $t = 0, 1, \ldots, H-1$ do
 9:         Get action $a_t \sim \pi(s_t, z_g)$.
10:         Execute action and observe $s_{t+1} \sim p(\cdot \mid s_t, a_t)$.
11:         Store $(s_t, a_t, s_{t+1}, z_g)$ into replay buffer $\mathcal{R}$.
12:     for $t = 0, 1, \ldots, H-1$ do
13:         for $j = 0, 1, \ldots, J$ do
14:             With probability $p$, sample $z'_g \sim p(\mathcal{Z}_\mathcal{I})$. Otherwise, sample a future state $s' \in \tau_{>t}$ in
                the current trajectory and compute $z'_g = e_\mathcal{I}(s')$.
15:             Store $(s_t, a_t, s_{t+1}, z'_g)$ into $\mathcal{R}$.
16:     for $k = 0, 1, \ldots, N-1$ do
17:         Sample $(s, a, s', z_g) \sim \mathcal{R}$.
18:         Compute $r = R_{z_g}(s') = -\|e_\mathcal{I}(s') - z_g\|_2^2$.
19:         Update actor and critic using $(s, a, s', z_g, r)$.
20: return $\pi(a \mid s, z)$
```

Method	$p(\mathcal{Z})$	$R_{z_g}(s')$
RIG	$\mathcal{N}(0, I)$	$-\|e^{\text{VAE}}(s') - z_g\|_2^2$
SkewFit	$p^{\text{skew}}(\mathcal{R})$	$-\|e^{\text{VAE}}(s') - z_g\|_2^2$
WSC	$\text{Uniform}(\mathcal{Z}_\mathcal{I}^{\min}, \mathcal{Z}_\mathcal{I}^{\max})$	$-\|e_\mathcal{I}(s') - z_g\|_2^2$

Table 3.1: Conceptual comparison between our method weakly-supervised control (WSC), and prior visual goal-conditioned RL methods, with their respective latent goal distributions $p(\mathcal{Z})$ and goal-conditioned reward functions $R_{z_g}(s')$. Our method can be seen as an extension of prior work to the weakly-supervised setting.

with off-policy RL, sampling transitions (s, a, s', z_g) with hindsight relabeling. At termination, our method outputs a goal-conditioned policy $\pi(a \mid s, z_g)$ which is trained to go to a state that is close to z_g in the disentangled latent space.

3.4 Experiments

We aim to first and foremost answer our core hypothesis: (1) Does weakly supervised control help guide exploration and learning, for increased performance over prior approaches? Further we also investigate: (2) What is the relative importance of the goal generation mechanism vs. the distance metric used in WSC?, (3) Is weak supervision necessary for learning a disentangled state representation?, (4) Is the policy's behavior interpretable?, and (5) How much weak supervision is needed to learn a sufficiently-disentangled state representation? Questions (1) through (4) are investigated in this section, while question (5) is studied in Appendix 3.4.5.

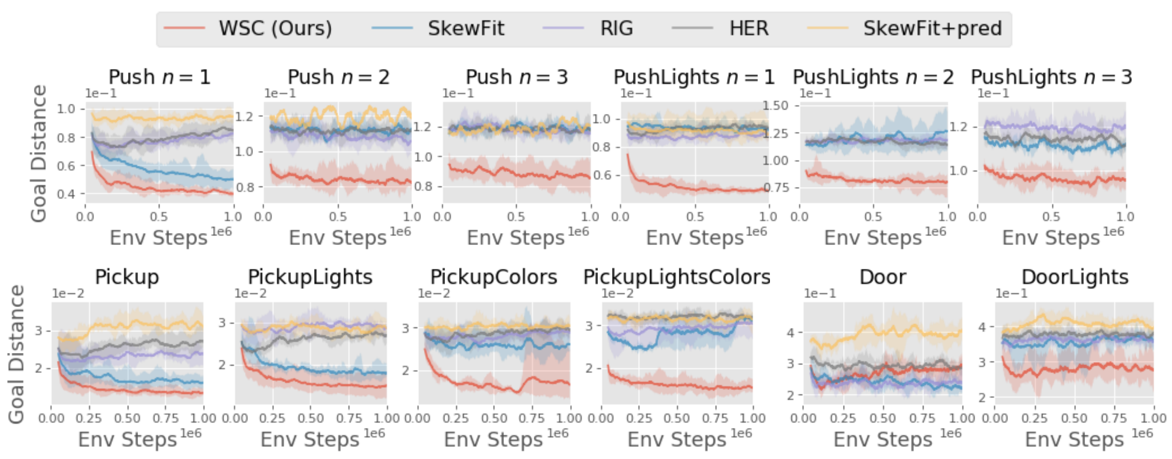

Figure 3.4: **Performance vs. training steps on visual goal-conditioned tasks**. Weakly-Supervised Control (WSC) learns more quickly than prior state-of-the-art goal-conditioned RL methods (HER, RIG, SkewFit), particularly as the complexity of the environment grows. Thus, we see that doing directed exploration and goal sampling in a (learned) semantically-disentangled latent space can be more effective than doing purely unsupervised exploration in the VAE latent space.

To answer these questions, we consider several vision-based, goal-conditioned manipulation tasks of varying complexity, shown in Fig. 3.2. In the *Push* and *Pickup* environments, the agent's task is to move a specific object to a goal location. In the *Door* environments, the agent's task is to open the door to match a goal angle. Both the state and goal observations are 48×48 RGB images.

Domain randomization: To further increase task complexity, we randomized the dynamics of some environments. In environments with 'light' as a factor (*PushLights*, *PickupLights*, *PickupLightsColors*, *DoorLights*), the lighting changes randomly at the start of each episode, with diffuse values sampled from $\text{Uniform}(0.2, 0.8)$. In environments with 'color' as a factor (*PickupColors*, *PickupLightsColors*), both the object color and table color are randomly at the start of each episode (from 5 table colors and 3 object colors).

Dataset generation: Both the training and test datasets were generated from the same distribution, and each consists of 256 or 512 images (see Table A.3). To generate the Sawyer datasets shown in Fig. 3.2, we first sampled each factor value uniformly within their respective range, then corrected the factors to be physically feasible before generating the corresponding image observations in the Mujoco simulator. In *Push* environments with $n > 1$ objects, the object positions were corrected to avoid collision. In *Pickup* environments, we sampled the object position on the ground (obj_z=0) with 0.8 probability, and otherwise placed the object in the robot gripper (obj_z$\geq$ 0). In *Door* environments, the gripper position was corrected to avoid collision with the door.

Eval metric: At test-time, all RL methods only have access to the test goal image, and is evaluated on the true goal distance. In *Push* and *Pickup*, the true goal distance is defined as the ℓ_2-distance between the current object position and the goal position. In *Push* environments with $n > 1$ objects, we only consider the goal distance for the blue object, and ignore the red and green objects (which are distractor objects to make the task more difficult). In *Door* environments,

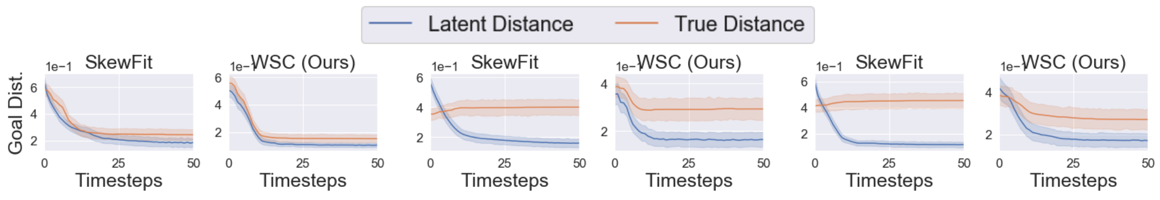

(a) Push $n = 1$ (b) Push $n = 2$ (c) Push $n = 3$

Figure 3.5: We roll out trained policies on visual goal-conditioned tasks, and compare the latent goal distance vs. the true goal distance between the object and the goal position. As the environment becomes increasingly complex (*Push* with $n \in \{1, 2, 3\}$ objects), the latent distance reward optimized by SkewFit becomes less indicative of the true goal distance, whereas the disentangled distance optimized by our method remains more accurate.

the true goal distance is defined as the distance between the current door angle and the goal angle value.

Comparisons: We compare our method to prior state-of-the-art goal-conditioned RL methods, which are summarized in Table 3.1. While the original hindsight experience replay (HER) algorithm [Andrychowicz et al., 2017] requires the state space to be disentangled, this assumption does not hold in our problem setting, where the observations are high-dimensional images. Thus, in our experiments, we modified **HER** [Andrychowicz et al., 2017] to sample relabeled goals from the VAE prior $g \sim \mathcal{N}(0, I)$ and use the negative ℓ_2-distance between goals and VAE-encoded states as the reward function. **RIG** [Nair et al., 2018] and **SkewFit** [Pong et al., 2019] are extensions of HER that use a modified goal sampling distribution that places higher weight on rarer states. RIG uses MLE to train the VAE, while SkewFit uses data samples from $p^{\text{skew}}(\mathcal{R})$ to train the VAE. For direct comparison, we use the weakly-labeled dataset $\mathcal{D}$ in HER, RIG, and SkewFit to pre-train the VAE, from which goals are sampled.

Additionally, to investigate whether our disentanglement approach for utilizing weak suppervision is better than alternative methods, we compare to a variant of SkewFit that optimizes an auxiliary prediction loss on the factor labels, which we refer to as **Skewfit+pred**.

Implementation details: Both the disentanglement model and VAE were pre-trained using the same dataset (size 256 or 512). A separate evaluation dataset of 512 image goals is used to evaluate the policies on visual goal-conditioned tasks. We used soft actor-critic [Haarnoja et al., 2018] as the base RL algorithm. All results are averaged over 5 random seeds. See Appendix A.2 for further details.

3.4.1 Does weakly supervised control help guide exploration and learning?

Do the disentangled representations acquired by our method guide goal-conditioned policies to explore in more semantically meaningful ways? In Fig. 3.4, we compare our method to prior state-of-the-art goal-conditioned RL methods on visual goal-conditioned tasks in the Sawyer environments (see Fig. 3.2). We see that doing directed exploration and goal sampling in a (learned) disentangled latent space is substantially more effective than doing purely unsupervised exploration in VAE latent state space, particularly for environments with increased variety in lighting and appearance.

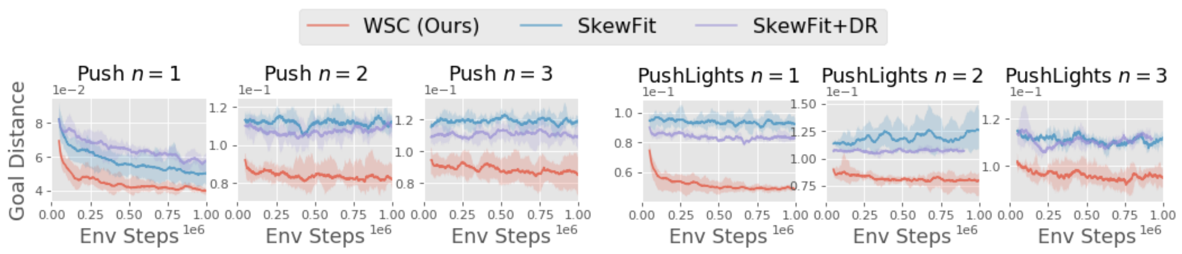

Figure 3.6: SkewFit+DR is a variant that samples goals in VAE latent space, but uses reward distances in disentangled latent space. We see that the disentangled distance metric can help slightly in harder environments (e.g., *Push* $n = 3$), but the goal generation mechanism of WSC is crucial to achieving efficient exploration.

Then, a natural next question remains: is our disentanglement approach for utilizing weak supervision better than alternative methods? One obvious approach for using supervision is to simply add an auxiliary loss to predict the weak labels from the representation. To this end, we trained a variant of SkewFit where the final hidden layer of the VAE is also trained to optimize an auxiliary prediction loss on the factor labels, which we refer to as 'Skewfit+pred'. In Fig. 3.4, we find that Skewfit+pred performs worse than WSC even though it uses stronger supervision (exact labels) compared to WSC. Hence, naive auxiliary losses do not lead to good representations for directing exploration or providing distance metrics. This comparison instead suggests that our approach of disentangling meaningful and irrelevant factor of the environment is important for effectively leveraging weak supervision.

3.4.2 Ablation: What is the role of distances vs. goals?

Our method uses the representation in two places: for goal-generation (Eq. 3.2) and for the distance metric (Eq. 3.3). Our next experiment will study the relative importance of using a disentangled representation in both places. First, we investigate whether the distance metric defined over the learned disentangled representation provides a more accurate signal for the true goal distance. In Fig. 3.5, we evaluate trained policies on visual goal-conditioned tasks, and compare the latent goal distance vs. the true goal distance between the object and the goal position at every timestep. As the environment becomes increasingly complex ($n \in \{1, 2, 3\}$), the latent distance reward optimized by SkewFit becomes less indicative of the true goal distance compared to the disentangled distance optimized by our method. The results suggest that the disentangled representation provide a more accurate reward signal for the training agent.

Next, we tested whether the distance metric in the disentangled space alone is enough to learn goal-conditioned tasks quickly. To do so, we trained a variant of SkewFit that samples latent goals in VAE latent space, but uses distances in disentangled latent space as the reward function. In Fig. 3.6, we see that the disentangled distance metric can help slightly in harder environments, but underperforms compared to the full method (WSC) with goal generation in disentangled latent space. Thus, we conclude that both the goal generation mechanism and distance metric of our method are crucial components for enabling efficient exploration.

3.4.3 Is the learned state representation disentangled?

To see whether weak supervision is necessary to learn state representations that are disentangled, we measure the correlation between true factor values and the latent dimensions of the encoded image in Table. 3.2. For the VAE, we took the latent dimension that has the highest correlation with the true factor value. The results illustrate that unsupervised losses are often insufficient for learning a disentangled representation, and utilizing weak labels in the training process can greatly improve disentanglement, especially as the environment complexity increases.

		Pearson correlation	
Env	Factor	VAE (SkewFit)	WSC (Ours)
Push $n = 1$	hand_x	0.97 ± 0.04	0.97 ± 0.01
	hand_y	0.85 ± 0.07	0.93 ± 0.02
	obj_x	0.78 ± 0.28	0.97 ± 0.01
	obj_y	0.65 ± 0.31	0.95 ± 0.01
Push $n = 3$	hand_x	0.95 ± 0.03	0.98 ± 0.01
	hand_y	0.50 ± 0.33	0.94 ± 0.03
	obj1_x	0.12 ± 0.18	0.96 ± 0.01
	obj1_y	0.15 ± 0.03	0.92 ± 0.02

Table 3.2: **Is the learned state representation disentangled?** We measure the correlation between the true factor value of the input image vs. the latent dimension of the encoded image on the evaluation dataset. We show the 95% confidence interval over 5 seeds. We find that unsupervised VAEs are often insufficient for learning a disentangled representation.

3.4.4 Is the policy's latent space interpretable?

Since our method uses an interpretable latent goal space to generate self-proposed goals and compute rewards for training the policy, we checked whether the learned policy is also semantically meaningful. In Table 3.3, we measure the correlation between latent goals and the final states of the policy rollout. For various latent goals $z_g \in \mathcal{Z}$, we rolled out the trained policy $\pi(a \mid s, z_g)$ and compared the final state with the latent goal z_g that the policy was conditioned on (see Section 3.4.4). For our method, we did a grid sweep over the latent goal values in $[\mathcal{Z}_{\mathcal{I}}^{\min}, \mathcal{Z}_{\mathcal{I}}^{\max}]$. For SkewFit, we took the latent dimensions that have the highest correlations with the true object XY positions, then did a similar grid sweep over the latent goal space. The results show that our method achieves higher Pearson correlation between latent goals and final states, meaning that it learns a more interpretable goal-conditioned policy where the latent goals align directly with the final state of the trajectory rollout.

In Fig. 3.7, we visualize the trajectories generated by our method's policy when conditioned on different latent goals $z_g = (z_1, z_2)$ obtained by doing a grid sweep over the latent space $[\mathcal{Z}_{\mathcal{I}}^{\min}, \mathcal{Z}_{\mathcal{I}}^{\max}]$. The object and gripper were spawned at fixed locations at the start of each trajectory. We see that the latent goal values z_g directly align with the final object position after rolling out the policy $\pi(a \mid s, z_g)$. In other words, varying each latent goal dimension corresponds to directly changing the object position in the X- or Y-coordinate. Thus, we conclude that our method produces a more semantically-meaningful goal-conditioned policy, where the latent goal

		Pearson correlation	
Env	Factor	SkewFit	WSC (Ours)
Push $n = 1$	obj_x	0.94 ± 0.03	0.95 ± 0.03
	obj_y	0.66 ± 0.17	0.94 ± 0.04
Push $n = 2$	obj1_x	0.59 ± 0.50	0.69 ± 0.37
	obj1_y	0.44 ± 0.68	0.86 ± 0.05
Push $n = 3$	obj1_x	0.44 ± 1.05	0.78 ± 0.11
	obj1_y	0.38 ± 1.44	0.89 ± 0.01

Table 3.3: **Is the learned policy interpretable?** We investigate whether latent goals z_g align directly with the final state of the trajectory after rolling out $\pi(a \mid s, z_g)$. We measure the correlation between the true factor value of the final state in the trajectory vs. the corresponding latent dimension of z_g. We show the 95% confidence interval over 5 seeds. Our method attains higher correlation between latent goals and final states, meaning that it learns a more interpretable goal-conditioned policy.

values directly align with the final position of the target object. The difference between WSC and SkewFit grows larger as we increase the complexity of the environment (i.e., increase the number of objects from $n = 1$ to $n = 3$).

3.4.5 How much weak supervision is needed?

Our method relies on learning a disentangled representation from weakly-labelled data, $\mathcal{D} = \{(s_1^{(i)}, s_2^{(i)}, y^{(i)})\}_{i=1}^N$. However, the total possible number of pairwise labels for each factor of variation is $N = \binom{M}{2}$, where $M \in \{256, 512\}$ is the number of images in the dataset. In this section, we investigate how much weak supervision is needed to learn a sufficiently-disentangled state representation such that it helps supervise goal-conditioned RL.

Number of factors that are labelled: There can be many axes of variation in an image observation, especially as the complexity of the environment grows. For example, the *PushLights* environment with $n = 3$ objects has nine factors of variation, including the positions of the robot arm and objects, and lighting (see Figure 3.2).

In Figure 3.8, we investigate whether WSC requires weak labels for all or some of the factors of variation. To do so, we compared the performance of WSC as we vary the set of factors of variation that are weakly-labelled in the dataset $\mathcal{D}$. We see that WSC performs well even when weak labels are not provided for task-irrelevant factors of variation, such as hand position and lighting.

Number of weak labels: In Table 3.4, we evaluate the quality of the learned disentangled representation model as we vary the number of weak labels, N. We measure disentanglement by evaluating the Pearson correlation between the true factor value compared to the latent dimension. We observe that, even with only 1024 pairwise labels, the resulting representation has a good degree of disenganglement, i.e. Pearson correlation of 0.8 or higher.

In Figure 3.9, we evaluate the downstream performance of our method on visual goal-conditioned tasks as we vary the number of weak labels. We see that our method outperforms SkewFit when provided at least 1024, 1024, 256, and 128 weak labels for *Push* $n = 1$, *PushLights*

	PushLights $n = 3$								
N	hand_x	hand_y	obj1_x	obj1_y	obj2_x	obj2_y	obj3_x	obj3_y	light
128	0.79 ± 0.04	0.64 ± 0.05	0.44 ± 0.08	0.32 ± 0.05	0.60 ± 0.03	0.51 ± 0.05	0.49 ± 0.07	0.41 ± 0.06	0.86 ± 0.04
256	0.87 ± 0.02	0.75 ± 0.05	0.58 ± 0.04	0.57 ± 0.04	0.60 ± 0.04	0.66 ± 0.03	0.65 ± 0.07	0.50 ± 0.06	0.90 ± 0.02
512	0.93 ± 0.01	0.86 ± 0.01	0.71 ± 0.03	0.70 ± 0.05	0.70 ± 0.04	0.58 ± 0.05	0.76 ± 0.04	0.67 ± 0.05	0.85 ± 0.04
1024	0.97 ± 0.01	0.91 ± 0.01	0.86 ± 0.01	0.81 ± 0.02	0.83 ± 0.02	0.80 ± 0.03	0.83 ± 0.03	0.80 ± 0.02	0.94 ± 0.02
2048	0.98 ± 0.00	0.94 ± 0.01	0.89 ± 0.01	0.87 ± 0.03	0.87 ± 0.01	0.86 ± 0.02	0.86 ± 0.02	0.84 ± 0.02	0.92 ± 0.01
4096	0.97 ± 0.00	0.94 ± 0.01	0.93 ± 0.01	0.88 ± 0.01	0.90 ± 0.01	0.88 ± 0.02	0.91 ± 0.01	0.85 ± 0.01	0.95 ± 0.00
VAE	0.00 ± 0.00	0.00 ± 1.00	0.02 ± 2.00	0.00 ± 3.00	0.01 ± 4.00	0.01 ± 5.00	0.02 ± 6.00	0.02 ± 7.00	0.02 ± 8.00

	PickupLightsColors							DoorLights	
N	hand_y	hand_z	obj_y	obj_z	light	table_color	obj_color	door_angle	light
128	0.94 ± 1.00	0.91 ± 2.00	0.72 ± 4.00	0.31 ± 5.00	0.88 ± 6.00	0.43 ± 7.00	0.62 ± 8.00	0.89 ± 3.00	0.84 ± 4.00
256	0.95 ± 1.00	0.96 ± 2.00	0.85 ± 4.00	0.47 ± 5.00	0.95 ± 6.00	0.62 ± 7.00	0.77 ± 8.00	0.95 ± 3.00	0.92 ± 4.00
512	0.96 ± 1.00	0.97 ± 2.00	0.91 ± 4.00	0.61 ± 5.00	0.97 ± 6.00	0.79 ± 7.00	0.82 ± 8.00	0.89 ± 3.00	0.95 ± 4.00
1024	0.95 ± 1.00	0.96 ± 2.00	0.94 ± 4.00	0.69 ± 5.00	0.97 ± 6.00	0.87 ± 7.00	0.92 ± 8.00	0.91 ± 3.00	0.94 ± 4.00
2048	0.95 ± 1.00	0.98 ± 2.00	0.95 ± 4.00	0.75 ± 5.00	0.96 ± 6.00	0.90 ± 7.00	0.93 ± 8.00	0.91 ± 3.00	0.94 ± 4.00
4096	0.95 ± 1.00	0.96 ± 2.00	0.94 ± 4.00	0.80 ± 5.00	0.96 ± 6.00	0.89 ± 7.00	0.96 ± 8.00	0.92 ± 3.00	0.95 ± 4.00
VAE	0.08 ± 0.00	0.25 ± 1.00	0.07 ± 2.00	0.09 ± 3.00	0.24 ± 4.00	0.09 ± 5.00	0.04 ± 6.00	0.01 ± 0.00	0.34 ± 1.00

Table 3.4: **How many weak labels are needed to learn a sufficiently-disentangled state representation?** We trained disentangled representations on varying numbers of weakly-labelled data samples $\{(s_1^{(i)}, s_2^{(i)}, y^{(i)})\}_{i=1}^{N}$ ($N \in \{128, 256, \ldots, 4096\}$), then evaluated how well they disentangled the true factors of variation in the data. On the evaluation dataset, we measure the Pearson correlation between the true factor value of the input image vs. the latent dimension of the encoded image. For the VAE (obtained from SkewFit), we took the latent dimension that has the highest correlation with the true factor value. We report the 95% confidence interval over 5 seeds. Even with a small amount of weak supervision (e.g. around 1024 labels), we are able to attain a representation with good disentanglement.

$n = 3$, *PickupLightsColors*, and *DoorLights*, respectively. Further, we find that 1024 pairwise labels is generally sufficient for good performance on all domains.

3.4.6 Noisy data experiments

While the weakly-labelled data can be collected at scale from crowd-sourcers and does not require expertise, the human labellers may mistakenly provide inaccurate rankings. Thus, we evaluated the robustness of the disentangled representation learning on more realistic, noisy datasets which are far less clean than the toy datasets used by Shu et al. [2019].

	PushLights $n = 1$					
Noise	hand_x	hand_y	obj1_x	obj1_y	light	All
5%	0.952 ± 0.012	0.822 ± 0.124	0.730 ± 0.276	0.606 ± 0.298	0.875 ± 0.094	0.797 ± 0.298
10%	0.721 ± 0.507	0.718 ± 0.296	0.520 ± 0.502	0.501 ± 0.270	0.730 ± 0.279	0.638 ± 0.410

	PushLights $n = 2$							
Noise	hand_x	hand_y	obj1_x	obj1_y	obj2_x	obj2_y	light	All
5%	0.949 ± 0.024	0.793 ± 0.226	0.864 ± 0.103	0.844 ± 0.145	0.842 ± 0.147	0.873 ± 0.032	0.936 ± 0.041	0.872 ± 0.118
10%	0.853 ± 0.165	0.588 ± 0.357	0.665 ± 0.422	0.518 ± 0.506	0.747 ± 0.185	0.864 ± 0.02	0.916 ± 0.04	0.736 ± 0.400

	PushLights $n = 3$								
Noise	hand_x	hand_y	obj1_x	obj1_y	obj2_x	obj2_y	obj3_x	obj3_y	All
5%	0.786 ± 0.144	0.78 ± 0.164	0.728 ± 0.217	0.698 ± 0.180	0.791 ± 0.117	0.858 ± 0.057	0.877 ± 0.013	0.833 ± 0.038	0.794 ± 0.661
10%	0.632 ± 0.487	0.551 ± 0.295	0.587 ± 0.264	0.547 ± 0.315	0.613 ± 0.307	0.817 ± 0.023	0.864 ± 0.033	0.851 ± 0.068	0.610 ± 0.643

Table 3.5: **Noisy labels**: We trained disentangled representations on noisy *PushLights* datasets for $n \in \{1, 2, 3\}$ objects, where each factor label was corrupted with probability 5% or 10%. We then measured the Pearson correlation between the true factor values vs. the corresponding latent dimension. Our method learns robustly-disentangled representations with 5% noise (around 80% correlation), but achieves lower performance with 10% noise (around 60-70% correlation). Results are taken over 5 seeds.

Real-world dataset: We collected 1,285 RGB images (1,029 train, 256 test) on a real Franka robot with 5 blocks (see Fig. 3.10a). We collected the images under various indoor lighting settings and at different times of the day, but we did not provide labels for the environment lighting conditions. We found that the robot arm often caused occlusion, hiding blocks from the camera view, so we used two RGB cameras placed at different locations, and stacked the RGB images into 6 channels (i.e., image arrays of shape $48 \times 48 \times 6$). We then had a human provide weak labels for the block positions. In Fig. 3.10b, we show that the learned disentangled model attains a sufficiently high Pearson correlation between the true XY-position of the block (relative to the image frame) vs. the corresponding latent dimension of the encoded image. The results suggest that weakly-supervised disentangled representation learning may be useful for training robots in the real-world, despite challenges such as environment stochasticity and object occlusion.

Noisy labels: We generated noisy datasets for *PushLights* with $n \in \{1, 2, 3\}$ objects, where each factor label was corrupted with probability 5% or 10%. In Table 3.5, we evaluate the quality of the learned disentangled representation model on the noisy datasets. Our method learns a robustly-disentangled representation with 5% noise (around 80% correlation), but achieves lower performance with 10% noise (around 60-70% correlation).

3.5 Related Work

Reinforcement learning of complex behaviors in rich environments with high-dimensional observations remains an open problem. Many of the successful applications of RL in prior work [Silver et al., 2017, Berner et al., 2019, Vinyals et al., 2019, Gu et al., 2017] effectively operate in a regime where the amount of data (i.e., interactions with the environment) dwarfs the complexity of task at hand. Insofar as alternative forms of supervision is the key to success for RL methods, prior work has proposed a number of techniques for making use of various types of ancillary supervision.

A number of prior works incorporate additional supervision beyond rewards to accelerate RL. One common theme is to use the task dynamics itself as supervision, using either forward dynamics [Watter et al., 2015, Finn and Levine, 2017, Hafner et al., 2018, Zhang et al., 2018a, Kaiser et al., 2019], some function of forward dynamics [Dosovitskiy and Koltun, 2016], or inverse dynamics [Pathak et al., 2017, Agrawal et al., 2016, Pathak et al., 2018] as a source of labels. Another approach explicitly predicts auxiliary labels [Jaderberg et al., 2016, Shelhamer et al., 2016, Gordon et al., 2018, Dilokthanakul et al., 2019]. Compact state representations can also allow for faster learning and planning, and prior work has proposed a number of tools for learning these representations [Mahadevan, 2005, Machado et al., 2017, Finn et al., 2016b, Barreto et al., 2017, Nair et al., 2018, Gelada et al., 2019, Lee et al., 2019a, Yarats et al., 2019]. Bengio et al. [2017], Thomas et al. [2017] propose learning representations using an independent controllability metric, but the joint RL and representation learning scheme has proven difficult to scale in environment complexity. Perhaps most related to our method is prior work that directly learns a compact representation of goals [Goyal et al., 2019, Pong et al., 2019, Nachum et al., 2018]. Our work likewise learns a low-dimensional representation of goals, but crucially learns it in such a way that we "bake in" a bias towards meaningful goals, thereby avoiding the problem of accidentally discarding salient state dimensions.

Human supervision is an important but expensive aspect of reward design [Hadfield-Menell et al., 2017], and prior work has studied how reward functions might be efficiently elicited from weak supervision. In settings where a human operator can manually control the system, a reward function can be acquired by applying inverse RL on top of human demonstrations [Ratliff et al., 2006, Finn et al., 2016a, Fu et al., 2017, Brown et al., 2019, Ghasemipour et al., 2019]. Another technique for sample-efficient reward design is to define rewards in terms of pre-trained classifiers [Xie et al., 2018, Fu et al., 2018b, Singh et al., 2019, Vecerik et al., 2019], which might be learned with supervised learning. State marginal distributions, which can be easier to specify in some tasks, have also been used as supervision for RL [Lee et al., 2019b, Ghasemipour et al., 2019]. Our method utilizes a much weaker form of supervision than state marginals, which potentially allows it to scale to more complex tasks. A final source of supervisory signal comes in the form of human preferences or rankings [Yaman et al., 2010, Christiano et al., 2017, Brown et al., 2019], where humans provide weak supervision about which of two behaviors they prefer. Our approach similarly obtains weak supervision from humans, but uses it to acquire a disentangled space for defining many tasks, rather than directly defining a single task reward.

Finally, our approach leverages weakly-supervised disentangled representation learning in the context of reinforcement learning. Learning such semantically-meaningful representations are useful for many downstream tasks that require machine learning models to be human-controllable or interpretable [Gilpin et al., 2018, Lake et al., 2017, van Steenkiste et al., 2019]. While there is no canonical definition for disentanglement, several formal definitions have been proposed [Higgins et al., 2018, Shu et al., 2019]. Many unsupervised methods for disentangled representation learning Higgins et al. [2017], Chen et al. [2018a, 2016], Kim and Mnih [2018], Esmaeili et al. [2018] learn a latent-variable model with prior $p(Z)$ and generator g, where $g(Z)$ approximates $g^*(\mathcal{F})$. However, unsupervised methods are generally brittle to hyperparameter settings and, more importantly, do not lead to consistently disentangled latent representations [Locatello et al., 2018]. Recently, weakly-supervised disentangled representation learning methods [Chen and Batmanghelich, 2019, Gabbay and Hoshen, 2019, Shu et al., 2019] have been shown to produce more robust disentangled representations than unsupervised methods, without requiring large amounts of supervision.

3.6 Discussion

We proposed weak supervision as a means to scalably introduce structure into goal-conditioned reinforcement learning. To leverage the weak supervision, we proposed a simple two phase approach that first learns a disentangled representation and then uses it to guide exploration, propose goals, and inform a distance metric. Our experimental results indicate that our approach, WSC, substantially outperforms self-supervised methods that cannot cope with the same breadth of environments as our method does. Further, our comparisons suggest that our disentanglement-based approach is critical for effectively leveraging the weak supervision.

Despite its strong performance, WSC has multiple limitations. WSC has the ability to leverage weak labels that can be easily collected offline with approaches like crowd compute, and does not require human demonstrations or reward specifications, but still may require the user to indicate the factors of variation that are relevant for downstream tasks. Further, our method only uses weak supervision during pre-training, which may produce representations that do not always generalize to new interaction later encountered by the agent. Incorporating weak supervision online, in the loop of RL, could address this issue to improve performance. In such settings, we expect class imbalance and human-in-the-loop learning to present important, but surmountable challenges.

Looking forward, our results suggest a number of interesting directions for future work. For example, there may be other forms of weak supervision [Shu et al., 2019] that can provide useful signal to the agent, as well as other ways to leverage these labels. Given the promising results in increasingly complex environments, evaluating this approach with robots in real-world environments is an exciting future direction. Overall, we believe that our framework provides a new perspective on supervising the development of general-purpose agents acting in complex environments.

The weakly-supervised RL framework utilizes weakly-labelled data to learn a semantically disentangled representation of images in order to learn more effectively in high-dimensional task spaces. More generally, language provides a way to encode combinatorial abstractions and generalizations of the visual and physical world. It also enables us to communicate instructions, questions, plans, and intentions to one another. How can we utilize language to equip deep RL agents with structured priors about the physical world, and enable generalization and knowledge transfer across different tasks? In the next chapter, we consider an embodied navigation agent that acts in a 3D environment to solve a task specified by an instruction or a question.

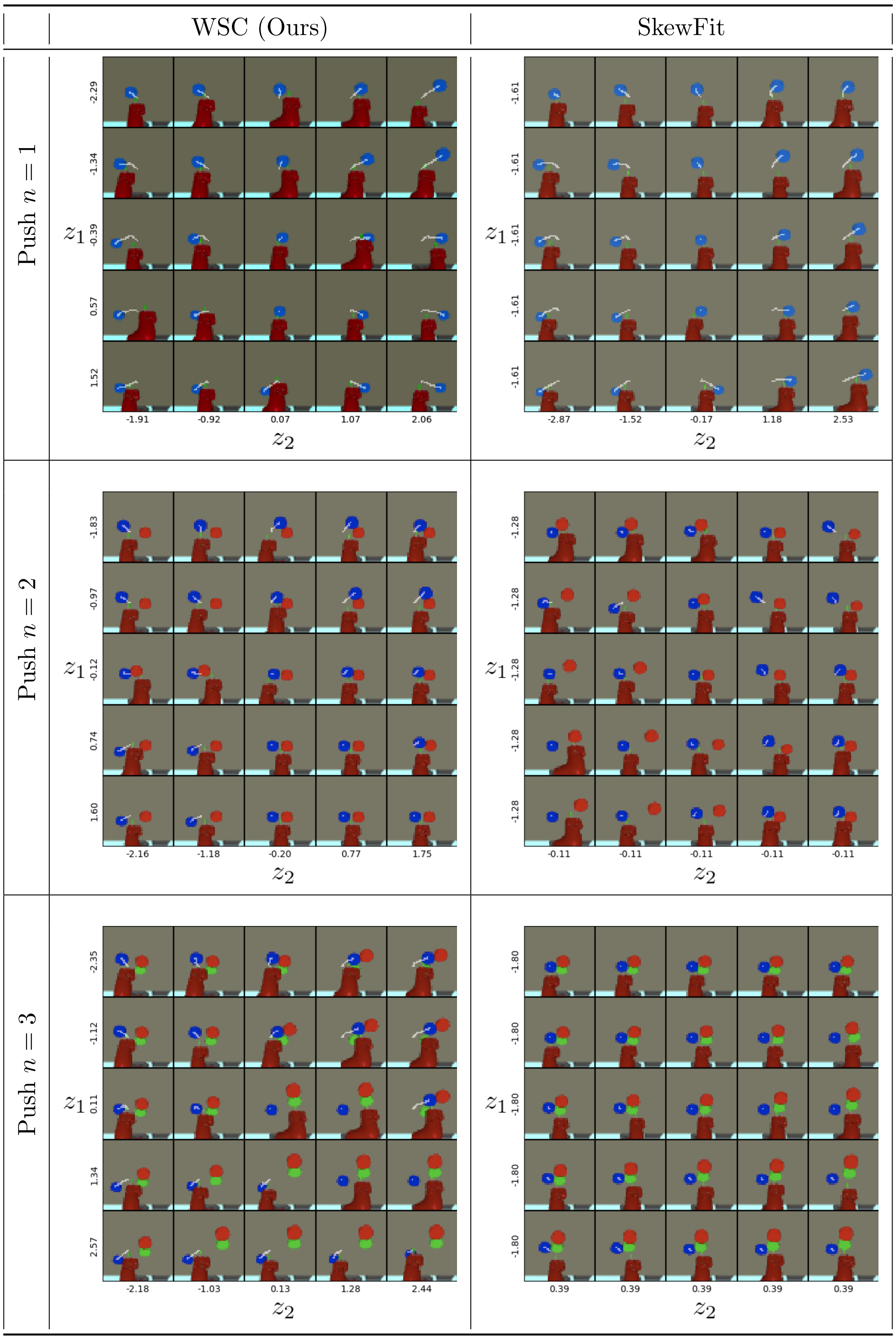

Figure 3.7: **Interpretable control**: Trajectories generated by WSC (*left*) and SkewFit (*right*), where the policies are conditioned on varying latent goals $(z_1, z_2) \in \mathbb{R}^2$. For SkewFit, we varied the latent dimensions that have the highest correlation with the object's XY-position, and kept the remaining latent dimensions fixed. The blue object always starts at the center of the frame in the beginning of each episode. The white lines indicate the target object's position throughout the trajectory. We see that the disentangled latent goal values of WSC directly align with the direction in which the WSC policy moves the blue object.

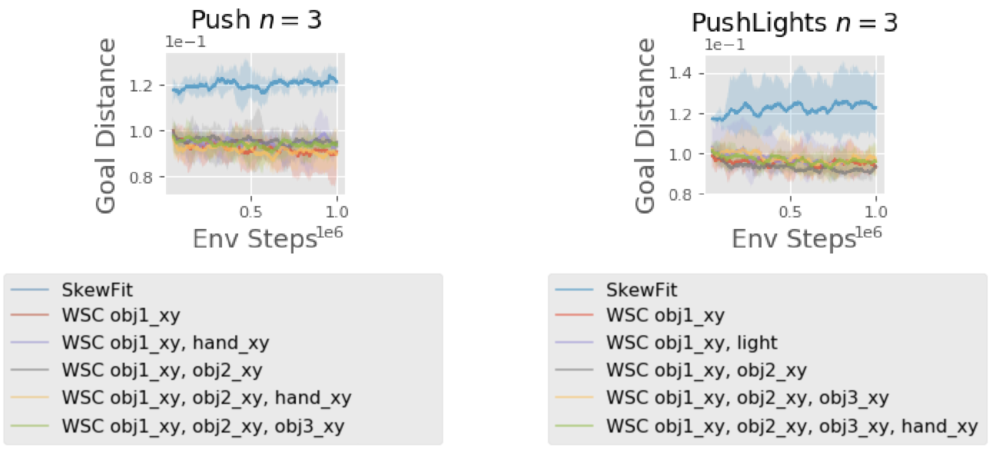

Figure 3.8: **How many factors of variation need to be labelled?** WSC outperforms SkewFit even without being provided weak labels for task-irrelevant factors, such as hand position and lighting.

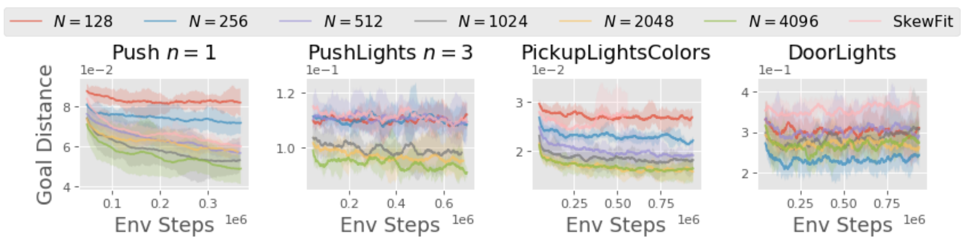

Figure 3.9: **How many weak labels are needed to help visual goal-conditioned RL?** We evaluate the performance of our method (WSC) on visual goal-conditioned tasks as we vary the number of weak pairwise labels $N \in \{128, 256, \dots, 4096\}$. We find that 1024 pairwise labels is generally sufficient for good performance on all domains.

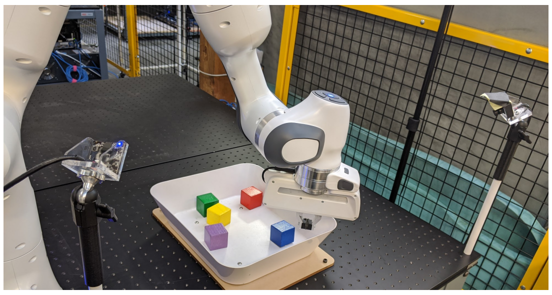

(a) Franka robot with 5 blocks

Block color	Pearson correlation x	Pearson correlation y
Red	0.747 ± 0.046	0.715 ± 0.016
Blue	0.649 ± 0.034	0.673 ± 0.042
Green	0.718 ± 0.057	0.625 ± 0.066
Yellow	0.663 ± 0.052	0.673 ± 0.057
Purple	0.505 ± 0.041	0.518 ± 0.055

(b) Disentangled representation performance

Figure 3.10: **Real-world dataset**: *(a)*: We collected 1,285 RGB camera images (1,029 train, 256 test) on a real Franka robot with 5 block objects, and then had a human provide weak labels for the block positions. We collected the images under various lighting conditions, and used two camera viewpoints to overcome object occlusion. *(b)*: Our method attains a sufficiently high Pearson correlation between the true XY-position of the block (relative to the image frame) vs. the latent dimension of the encoded image, suggesting that weakly-supervised disentangled representation learning may be useful for training robots in the real-world. Results are taken over 6 seeds.

Chapter 4

Multimodal Learning of Vision, Language and Control

Deep reinforcement learning has been shown to be capable of achieving super-human performance in playing games such as Atari 2600 [Mnih et al., 2013] and Go [Silver et al., 2016]. Following the success of deep reinforcement learning in 3D Games such as Doom [Lample and Chaplot, 2017, Dosovitskiy and Koltun, 2016] and Deepmind Lab [Mnih et al., 2016], there has been increased interest in using deep reinforcement learning for training *embodied* AI agents, which interact with a 3D environment by receiving first-person views of the environment and taking navigational actions. The simplest navigational agents learn a particular behavior such as collecting or avoiding particular objects [Kempka et al., 2016, Jaderberg et al., 2016, Mirowski et al., 2016] or playing deathmatches [Lample and Chaplot, 2017, Dosovitskiy and Koltun, 2016]. Subsequently, there have been efforts on training navigational agents whose behavior is conditioned on a target specified using images [Zhu et al., 2017] or coordinates [Gupta et al., 2017a, Savva et al., 2017]. More recently, there has been much interest in training agents with goals specified (either explicitly or implicitly) via language since that offers several advantages over using images or coordinates.

First, the compositional structure of language allows generalization to new tasks without additional learning. Prior work [Oh et al., 2017, Hermann et al., 2017, Chaplot et al., 2017] has trained navigational agents to follow instructions and shown zero-shot generalization to new instructions which contain unseen composition of words seen in the training instructions. Second, language is also a natural means for humans to communicate with autonomous agents. Language not only allows instruction but also interaction. Gordon et al. [2018] and Das et al. [2017] train agents to answer questions by navigating in the environment to gather the required information.

Figure 4.1a shows examples of these multimodal tasks. The agent interacts with the environment by receiving pixel-level visual input and an instruction or a question specifying the task. These multimodal tasks involve several challenges including perception from raw pixels, grounding of words in the instruction or question to visual objects and attributes, reasoning to perform relational tasks, fine-grained navigation in 3D environments with continuous state space, and learning to answer questions. Training a model for each task typically requires tens or hundreds of millions of frames. In this paper, we train a multi-task navigation model to follow instructions and answer questions. Training a single model to perform multiple tasks can help improve the sample efficiency as many of the aforementioned challenges are common between different multimodal tasks. Furthermore, training a multi-task model can also facilitate knowledge transfer between the tasks and allow the model to generalize to scenarios which were not possible with single tasks. For example, if an agent learns to follow the instruction 'Go to the red torch' and answer the question 'What color is the pillar?', then *ideally* it should also be able to follow the instruction 'Go to the red pillar' and answer the question 'What color is the torch?' without any additional training.

Consequently, we define *cross-task knowledge transfer* evaluation criterion to test the generalization ability of multimodal multi-task models. This criterion evaluates zero-shot learning on instructions and questions consisting of unseen composition of words in both tasks. In order to achieve cross-task knowledge transfer, words in the input space of both tasks need to be aligned with each other and with the answer space while they are being grounded to visual objects and attributes. In the above example, in order to answer the question 'What color is the pillar?', the knowledge of the word 'pillar' and its grounding in the visual world must be transferred from instructions, as it is never seen in any training question. Also, the agent also needs to learn to relate the word 'red' in the input space with the answer 'red' along with its grounding in the visual world.

There has been work on training single-task models for both instruction following and embodied question answering. We show that several prior single-task models, when trained on both tasks, fail to achieve cross-task knowledge transfer. In the above example, if the model sees the word 'pillar' only in instructions during training, its representation of the word 'pillar' would be associated with the instruction following task. Consequently, it would always take navigational actions whenever it sees the word 'pillar' in a test question and never any answer actions. We propose a novel dual-attention model involving sequential Gated- and Spatial-Attention operations to perform explicit task-invariant alignment between the image representation channels and the words in the input and answer space. We create datasets and simulation scenarios for testing cross-task knowledge transfer in the Doom environment [Kempka et al., 2016] and show an absolute improvement of 43-61% on instructions and 5-26% for questions over baselines in a range of scenarios with varying difficulty. Additionally, we demonstrate that the modularity of our model allows easy addition of new objects and attributes to a trained model.

4.1 Related Work

This paper is motivated by a series of works on learning to follow navigation instructions [Oh et al., 2017, Hermann et al., 2017, Chaplot et al., 2017, Wu et al., 2018, Yu et al., 2018a] and learning to answer questions by navigating around the environment [Das et al., 2017, Gordon et al., 2018]. Among methods learning from instructions in 3D environments, Oh et al. [2017] introduced a hierarchical RL model for learning sequences of instructions by learning skills to solve subtasks. Chaplot et al. [2017] introduced a gated-attention model for multimodal fusion of textual and visual representations using multiplicative interactions, whereas Hermann et al. [2017] introduced auxiliary tasks such as temporal autoencoding and language prediction to improve sample efficiency for this task. Yu et al. [2018a] proposed guided feature transformation

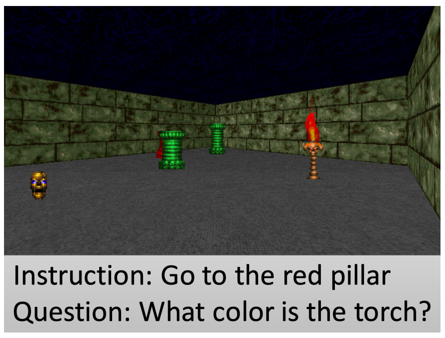
Instruction: Go to the red pillar
Question: What color is the torch?

(a) Embodied multimodal tasks

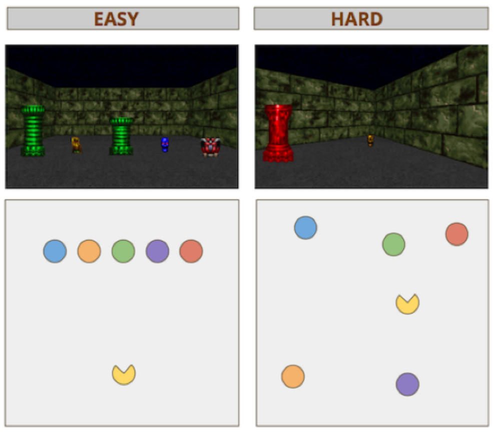

(b) Bird's eye view of the map

Figure 4.1: **(a)** We consider embodied multimodal tasks, where the agent receives visual first-person observations and an instruction or a question specifying the task. **(b)** Example starting states and bird's eye view of the map showing agent and candidate object locations in Easy and Hard settings.

which transforms visual representations using latent sentence embeddings computed from the language input.

Among models for embodied question answering, Das et al. [2017] introduced a hierarchical model consisting of 4 modules, each for processing images, encoding questions, navigation, and question-answering, each of which is pretrained with supervised or imitation learning, followed by fine-tuning of the navigation model using reinforcement learning. Gordon et al. [2018] introduced the task of Interactive Question Answering which involves interacting with objects in the environment with non-navigational actions for answering questions. They proposed Hierarchical Interactive Memory Network (HIMN), which allows temporal abstraction using a factorized set of controllers.

All of the above methods are designed for a single task, following navigational instructions or answering questions, whereas we train a single model for both tasks. Yu et al. [2018b] introduced a model for interactive language acquisition by training on both Visual Question Answering and following instructions in a 2D grid world environment. In contrast, we tackle multimodal multitask learning in challenging 3D environments. Partial observability results in the requirement of learning to navigate for answering the questions, turning visual question answering to embodied question answering. 3D environments also allow us to test interesting and more challenging instructions, such as those based on the relative size of the objects, in addition to object types and colors.

In addition to the above, there is a large body of work on multimodal learning in static settings which do not involve navigation or reinforcement learning. Some relevant works which use attention mechanisms similar to the ones used in our proposed model include Perez et al. [2017], Fukui et al. [2016], Xu and Saenko [2016], Hudson and Manning [2018], Gupta et al. [2017b] for Visual Question Answering and Zhao et al. [2018] for grounding audio to vision.

Table 4.1: Table showing training and test sets for both Semantic Goal Navigation (SGN) and Embodied Question Answering (EQA) tasks. The test set consists of unseen instructions and questions. The dataset evaluates a model for cross-task knowledge transfer between SGN and EQA.

Task	Train Set	Test Set
SGN	Instructions NOT containing 'red' & 'pillar': 'Go to the largest **blue** object' 'Go to the **torch**'	Instructions containing 'red' or 'pillar': 'Go to the red pillar' 'Go to the tall red object'
EQA	Questions NOT containing 'blue' & 'torch': 'Which is the smallest red object?' 'What color is the tall pillar?'	Questions containing 'blue' or 'torch': 'Which object is **blue** in color?' 'What color is the **torch**?'

4.2 Problem Formulation

Consider an autonomous agent interacting with an episodic environment as shown in Figure 4.1. At the beginning of each episode, the agent receives a textual input T specifying the task that it needs to achieve. For example, T could be an instruction asking to navigate to the target object or a question querying some visual detail of objects in the environment. At each time step t, the agent observes a state $s_t = (I_t, T)$ where I_t is the first-person (egocentric) view of the environment, and takes an action a_t, which could be a navigational action or an answer action. The agent's objective is to learn a policy $\pi(a_t|s_t)$ which leads to successful completion of the task specified by the textual input T.

Tasks. We focus on the multi-task learning of two visually-grounded language navigation tasks: In *Embodied Question Answering (EQA)*, the agent is given a question ('What color is the torch?'), and it must navigate around the 3D environment to explore the environment and gather information to answer the question ('red'). In *Semantic Goal Navigation (SGN)*, the agent is given a language instruction ('Go to the red torch') to navigate to a goal location.

Environments. We adapt the ViZDoom [Kempka et al., 2016]-based language grounding environment proposed by Chaplot et al. [2017] for visually-grounded multitask learning. It consists of a single room with 5 objects. The objects are randomized in each episode based on the textual input. We use two difficulty settings for the Doom domain as shown in Figure 4.1b: *Easy*: The agent is spawned at a fixed location. The candidate objects are spawned at five fixed locations along a single horizontal line in the field of view of the agent. *Hard*: The candidate objects and the agent are spawned at random locations and the objects may or may not be in the agent's field of view in the initial configuration. The agent must explore the map to view all objects. The agent can take 4 actions: 3 navigational actions (forward, left, right) and 1 answer action. When the agent takes the answer action, the answer with the maximum probability in the output answer distribution is used.

Datasets. We use the set of 70 instructions from Chaplot et al. [2017] and create a dataset for 29 questions using the same set of objects and attributes. These datasets include instructions and questions about object types, colors, relative sizes (tall/short) and superlative sizes (smallest/largest). We define cross-task knowledge transfer as an evaluation criterion for testing the generalization of multi-task models. We create train-test splits for both instructions and questions datasets to explicitly test a multitask model's ability to transfer the knowledge of

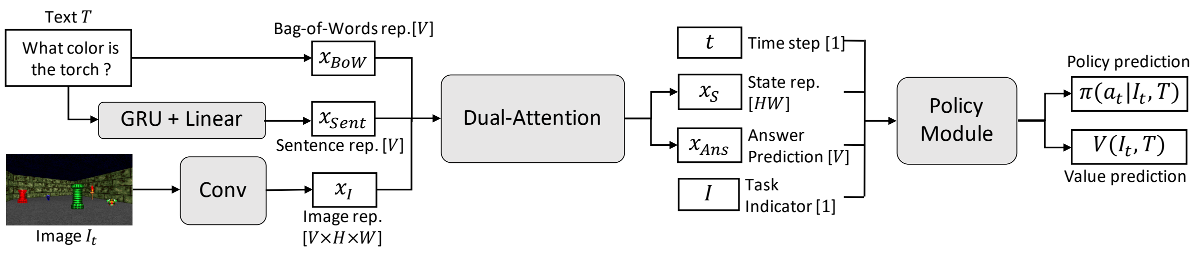

Figure 4.2: Overview of our proposed architecture, described in detail in Section 4.3.

words across different tasks. Each instruction in the test set contains a word that is never seen in any instruction in the training set but is seen in some questions in the training set. Similarly, each question in the test set contains a word never seen in any training set question. Figure 4.1 illustrates the train-test split of instructions and questions used in our experiments in the Doom domain. Note that for the EQA trainset, unseen words can be present in the answer. More details about the datasets and the environments are deferred to Appendix B. We also report results on an additional environment based on House3D [Wu et al., 2018] in Appendix C.

4.3 Proposed Method

In this section, we describe our proposed architecture (illustrated in Figure 4.2). At the start of each episode, the agent receives a textual input T (an instruction or a question) specifying the task that it needs to achieve. At each time step t, the agent observes an egocentric image I_t which is passed through a convolutional neural network [LeCun et al., 1995] with ReLU activations [Glorot et al., 2011] to produce the image representation $x_I = f(I_t; \theta_{\text{conv}}) \in \mathbb{R}^{V\times H\times W}$, where θ_{conv} denotes the parameters of the convolutional network, V is the number of feature maps in the convolutional network output which is by design set equal to the vocabulary size (of the union of the instructions and questions training sets), and H and W are the height and width of each feature map. We use two representations for the textual input T: (1) the bag-of-words representation denoted by $x_{\text{BoW}} \in 0,1^V$ and (2) a sentence representation $x_{\text{sent}} = f(T; \theta_{\text{sent}}) \in \mathbb{R}^V$, which is computed by passing the words in T through a Gated Recurrent Unit (GRU) [Cho et al., 2014] network followed by a linear layer. Here, θ_{sent} denotes the parameters of the GRU network and the linear layer with ReLU activations. Next, the Dual-Attention unit f_{DA} combines the image representation with the text representations to get the complete state representation x_{S} and answer prediction x_{Ans}:

$$x_{\text{S}}, x_{\text{Ans}} = f_{\text{DA}}(x_I, x_{\text{BoW}}, x_{\text{sent}})$$

Finally, x_S and x_{Ans}, along with a time step embedding and a task indicator variable (for whether the task is SGN or EQA), are passed to the policy module to produce an action.

Dual-Attention Unit. The Dual-Attention unit uses two types of attention mechanisms, Gated-Attention f_{GA} and Spatial-Attention f_{SA}, to align representations in different modalities and tasks.

Gated-Attention. The Gated-Attention unit (Figure 4.3a) was proposed in [Chaplot et al., 2017] for multimodal fusion. Intuitively, a GA unit attends to the different channels in the image representation based on the text representation. For example, if the textual input is the

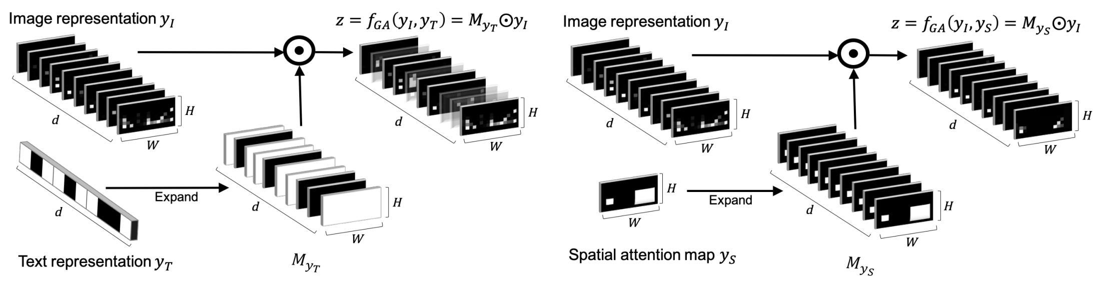
Image representation y_I
$z = f_{GA}(y_I, y_T) = M_{y_T} \odot y_I$
Text representation y_T
Expand
M_{y_T}
Image representation y_I
$z = f_{GA}(y_I, y_S) = M_{y_S} \odot y_I$
Spatial attention map y_S
Expand
M_{y_S}

(a) Gated-Attention unit f_{GA} (b) Spatial-Attention unit f_{SA}

Figure 4.3: The Dual-Attention unit uses two types of attention mechanisms (a, b) to align representations in different modalities and tasks.

instruction 'Go to the red pillar', then the GA unit can learn to attend to channels which detect red things and pillars. Specifically, the GA unit takes as input a 3-dimensional tensor image representation $y_I \in \mathbb{R}^{d\times H\times W}$ and a text representation $y_T \in \mathbb{R}^d$, and outputs a 3-dimensional tensor $z \in \mathbb{R}^{d\times H\times W}$[1]. Note that the dimension of y_T is equal to the number of feature maps and the size of the first dimension of y_I. In the Gated-Attention unit, each element of y_T is expanded to a $H \times W$ matrix, resulting in a 3-dimensional tensor $M_{y_T} \in \mathbb{R}^{d\times H\times W}$, whose $(i,j,k)^{th}$ element is given by $M_{y_T}[i,j,k] = y_T[i]$. This matrix is multiplied element-wise with the image representation: $z = f_{\mathrm{GA}}(y_I, y_T) = M_{y_T} \odot y_I$, where $\odot$ denotes the Hadamard product [Horn, 1990].

Spatial-Attention. We propose a Spatial-Attention unit (Figure 4.3b) which is analogous to the Gated-Attention unit except that it attends to different *pixels* in the image representation rather than the channels. For example, if the textual input is the question 'Which object is blue in color?', then we would like to spatially attend to the parts of the image which contain a blue object in order recognize the type of the blue object. The Spatial-Attention unit takes as input a 3-dimensional tensor image representation $y_I \in \mathbb{R}^{d\times H\times W}$ and a 2-dimensional spatial attention map $y_S \in \mathbb{R}^{H\times W}$, and outputs a tensor $z \in \mathbb{R}^{d\times H\times W}$. Note that the height and width of the spatial attention map is equal to the height and width of the image representation. In the spatial-attention unit, each element of the spatial attention map is expanded to a d dimensional vector. This again results in a 3-dimensional tensor $M_{y_S} \in \mathbb{R}^{d\times H\times W}$, whose $(i,j,k)^{th}$ element is given by: $M_{y_S}[i,j,k] = y_S[j,k]$. Just like in the Gated-Attention unit, this matrix is multiplied element-wise with the image representation: $z = f_{\mathrm{SA}}(y_I, y_S) = M_{y_S} \odot y_I$. Similar spatial attention mechanisms have been used for Visual Question Answering [Fukui et al., 2016, Xu and Saenko, 2016, Hudson and Manning, 2018, Gupta et al., 2017b] and grounding audio in vision [Zhao et al., 2018].

Dual-Attention. We now describe the operations in the Dual-Attention unit shown in Figure 4.4, as well as motivate the intuitions behind each operation. Given x_I, x_{BoW}, and x_{sent}, the Dual-Attention unit first computes a Gated-Attention over x_I using x_{BoW}:

$$x_{\mathrm{GA1}} = f_{\mathrm{GA}}(x_I, x_{\mathrm{BoW}}) \in \mathbb{R}^{V\times H\times W}. \tag{4.1}$$

Intuitively, this first Gated-Attention unit grounds each word in the vocabulary with a feature

[1]We use the variables y and z to describe the Gated-Attention and Spatial-Attention units in a general capacity. We will later instantiate these units multiple times with x variables in our model.

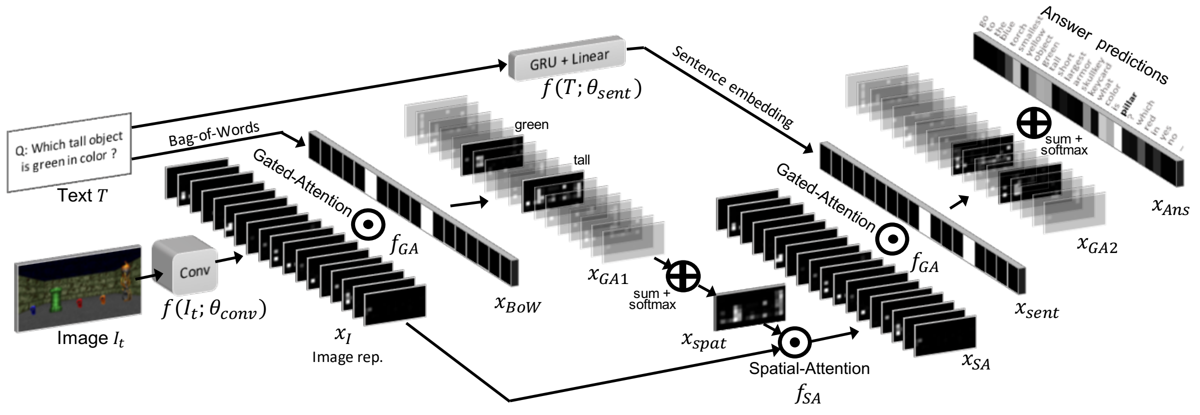

Figure 4.4: Architecture of the **Dual-Attention** unit with example intermediate representations and operations.

map in the image representation. A particular feature map is activated if and only if the corresponding word occurs in the textual input. In other words, the feature maps in the convolutional output learn to detect different objects and attributes, and words in the textual input specify which objects and attributes are relevant to the current task. The Gated-Attention using BoW representation attends to feature maps detecting corresponding objects and attributes, and masks all other feature maps. We use the bag-of-words representation for the first GA unit as it explicitly aligns the words in textual input irrespective of whether it is a question or an instruction. Note that bag-of-words representation has been used previously in models trained for learning to follow instructions [Hermann et al., 2017].

Next, the output of the Gated-Attention unit x_{GA1} is converted to a spatial attention map by summing over all channels followed by a softmax over $H \times W$ elements:

$$x_{\text{spat}} = \sigma\left(\sum_{i}^{V} x_{\text{GA1}}[i,:,:]\right) \in \mathbb{R}^{H\times W} \tag{4.2}$$

where the softmax $\sigma(z)_j = \exp(z_j)/\sum_k \exp(z_k)$ ensures that the attention map is spatially normalized. Summation of x_{GA1} along the depth dimension gives a spatial attention map which has high activations at spatial locations where relevant objects or attributes are detected. ReLU activations in the convolutional feature maps makes all elements positive, ensuring that the summation aggregates the activations of relevant feature maps.

x_{spat} and x_I are then passed through a Spatial-Attention unit:

$$x_{\text{SA}} = f_{\text{SA}}(x_I, x_{\text{spat}}) \in \mathbb{R}^{V\times H\times W} \tag{4.3}$$

The Spatial-Attention unit outputs all attributes present at the locations where relevant objects and attributes are detected. This is especially helpful for question answering, where a single Gated-Attention may not be sufficient. For example, if the textual input is 'Which color is the pillar?', then the model needs to attend not only to feature maps detecting pillars (done by the Gated-Attention), but also to other attributes at the spatial locations where pillars are seen in order to predict their color. Note that a single Gated-Attention is sufficient for instruction following, as shown in [Chaplot et al., 2017]. For example, if the textual input is 'Go to the green pillar', the first Gated-Attention unit can learn to attend to feature maps detecting green objects and pillar, and learn a navigation policy based on the spatial locations of the feature map activations.

x_{SA} is then passed through another Gated-Attention unit with the sentence-level text representation:

$$x_{\text{GA2}} = f_{\text{GA}}(x_{\text{SA}}, x_{\text{sent}}) \in \mathbb{R}^{V \times H \times W} \tag{4.4}$$

This second Gated-Attention unit enables the model to attend to different types of attributes based on the question. For instance, if the question is asking about the color ('Which color is the pillar?'), then the model needs to attend to the feature maps corresponding to colors; or if the question is asking about the object type ('Which object is green in color?'), then the model needs to attend to the feature maps corresponding to object types. The sentence embedding x_{sent} can learn to attend to multiple channels based on the textual input and mask the rest.

Next, the output is transformed to answer prediction by again doing a summation and softmax but this time summing over the height and width instead of the channels:

$$x_{\text{Ans}} = \sigma\left(\sum_{j,k}^{H,W} x_{\text{GA2}}[:, j, k]\right) \in \mathbb{R}^{V} \tag{4.5}$$

Summation of x_{GA2} along each feature map aggregates the activations for relevant attributes spatially. Again, ReLU activations for sentence embedding ensure aggregation of activations for each attribute or word. The answer space is identical to the textual input space $\mathbb{R}^V$.

Finally, the Dual-Attention unit f_{DA} outputs the answer prediction x_{Ans} and the flattened spatial attention map $x_{\text{S}} = \text{vec}(x_{\text{spat}})$, where $\text{vec}(\cdot)$ denotes the flattening operation.

Policy Module. The policy module takes as input the state representation x_{S} from the Dual-Attention unit, a time step embedding t, and a task indicator variable I (for whether the task is SGN or EQA). The inputs are concatenated then passed through a linear layer, then a recurrent GRU layer, then linear layers to estimate the policy function $\pi(a_t \mid I_t, T)$ and the value function $V(I_t, T)$.

All above operations are differentiable, making the entire architecture trainable end-to-end. Note that all attention mechanisms in the Dual-Attention unit only modulate the input image representation, i.e., mask or amplify specific feature maps or pixels. This ensures that there is an explicit alignment between the words in the textual input, the feature maps in the image representation, and the words in answer space. This forces the convolutional network to encode all the information required with respect to a certain word in the corresponding output channel. For the model to predict 'red' as the answer, it must detect red objects in the corresponding feature map. This explicit task-invariant alignment between convolutional feature maps and words in the input and answer space facilitates grounding and allows for cross-task knowledge transfer. As shown in the results later, this also makes our model modular and allows easy addition of objects and attributes to a trained model.

Optimization. The entire model is trained to predict both navigational actions and answers jointly. The policy is trained using Proximal Policy Optimization (PPO) [Schulman et al., 2017]. For training the answer predictions, we use a supervised cross-entropy loss. Both types of losses have common parameters as the answer prediction is essentially an intermediate representation for the policy.

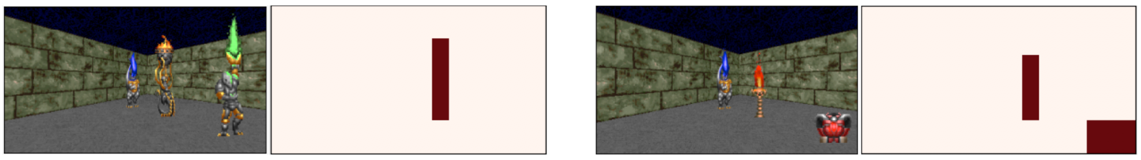

Figure 4.5: Example auxiliary task labels for the red channel.

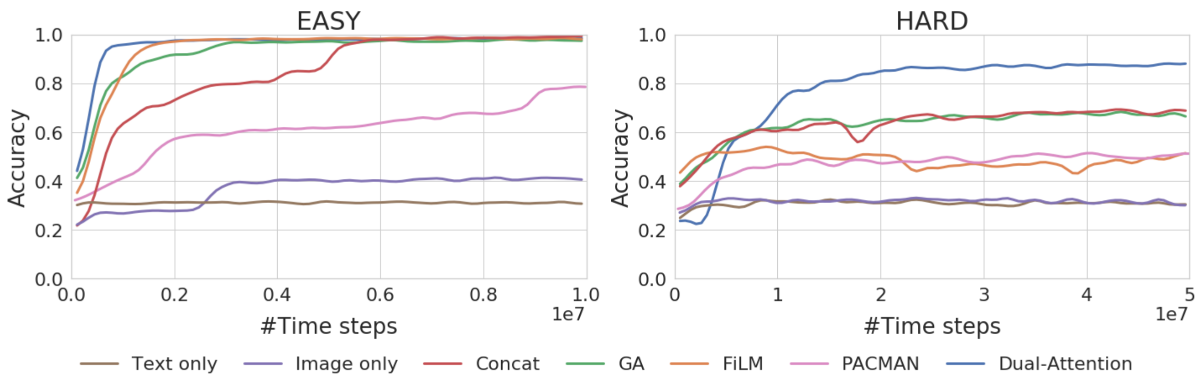

Figure 4.6: Training accuracy of all models trained **with** auxiliary tasks for *Easy* (left) and *Hard* (right).

Auxiliary Task. In order for the feature maps in the convolutional output to be able to detect different objects and attributes, we add a spatial auxiliary task to detect the object or attribute in the convolutional output channels corresponding to the word in the bag-of-words representation. A prior work [Gupta et al., 2017b] also explored the use of attribute and object recognition as an auxiliary task for Visual Question Answering. Rather than doing fine-grained object detection, we keep the size of the auxiliary predictions the same as the convolutional output to avoid increase in the number of parameters, and maintain the explicit alignment on the convolutional feature maps with the words. Consequently, auxiliary labels are $(V \times H \times W)$-dimensional tensors, where each of the V channels corresponds to a word in the vocabulary, and each element in a channel is 1 if the corresponding object or attribute is present in the current frame spatially. Figure 4.5 shows examples of auxiliary task labels for the channel corresponding to the word 'red'. The auxiliary tasks are also trained with cross-entropy loss.

4.4 Experiments & Results

Jointly learning semantic goal navigation and embodied question answering essentially involves a fusion of textual and visual modalities. While prior methods are designed for a single task, we adapt several baselines for our environment and tasks by using their multimodal fusion techniques. We use two naive baselines, **Image only** and **Text only**; two baselines based on prior semantic goal navigation models, **Concat** (used by Hermann et al. [2017], Misra et al. [2017]) and **Gated-Attention** (GA) [Chaplot et al., 2017]; and two baselines based on Question Answering models, **FiLM** [Perez et al., 2017] and **PACMAN** [Das et al., 2017]. For fair comparison, we replace the proposed Dual-Attention unit with multimodal fusion techniques in the baselines and keep everything else identical to the proposed model. We provide more implementation details of all baselines in the Appendix.

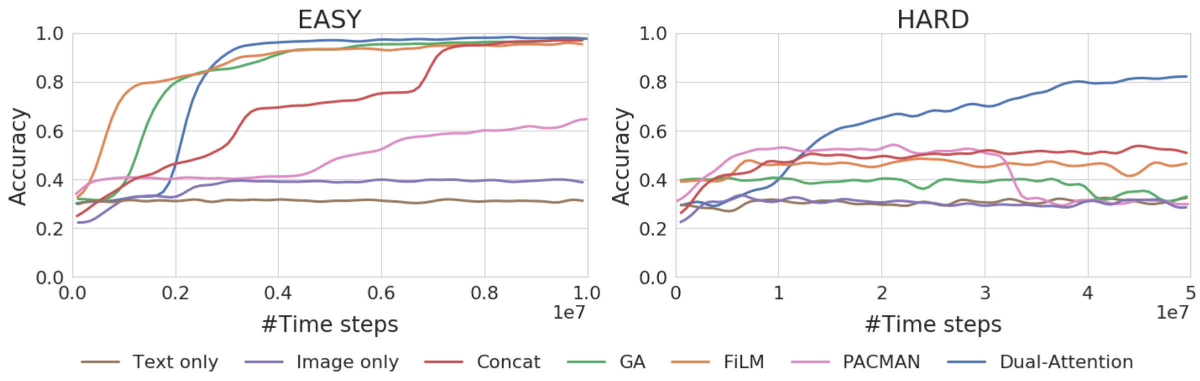

Figure 4.7: Training accuracy of all models trained **without** auxiliary tasks for *Easy* (left) and *Hard* (right).

Results. We train all models for 10 million frames in the *Easy* setting and 50 million frames in the *Hard* setting. We use a +1 reward for reaching the correct object in SGN episodes and predicting the correct answer in EQA episodes. We use a small negative reward of -0.001 per time step to encourage shorter paths to target and answering questions as soon as possible. We also use distance-based reward shaping for SGN episodes, where the agent receives a small reward proportional to the decrease in distance to the target. In the next subsection, we evaluate the performance of the proposed model without the reward shaping. SGN episodes end when the agent reaches any object, and EQA episodes when the agent predicts any answer. All episodes have a maximum length of 210 time steps. We train all models with and without the auxiliary tasks using identical reward functions.

All models are trained jointly for both the tasks and tested on each task separately[2]. We show the training performance curves for all models trained with Auxiliary tasks in Figure 4.6 and trained without auxiliary tasks in Figure 4.7 for both *Easy* and *Hard* settings. In Table 4.2, we report the test performance of all models on both SGN and EQA for both *Easy* and *Hard* settings. We observe that the Dual-Attention model and many baselines achieve nearly 100% accuracy during training in the Easy setting as seen on the left in Figures 4.6 and 4.7, however the test performance of all the baselines is considerably lower than the Dual-Attention model (see Table 4.2 (left)). Even without auxiliary tasks, Dual-Attention model achieves an accuracy of 86% for SGN and 53% for EQA, whereas the best baseline performance is 33% for both SGN and EQA. Performance of all the baselines is worse than 'Text only' model on EQA test set, although the training accuracy is close to 100%. This indicates that baselines tend to overfit on the training set and fail to generalize to questions which contain words never seen in training questions. For the Hard setting, the Dual-Attention model achieves a higher training (87% vs. 70%) as well as test performance (82% vs. 39% for SGN, 59% vs. 33% for EQA with Aux) than the baselines (as seen on the right in Fig 4.6, Fig 4.7 and Table 4.2). These results confirm the hypothesis that prior models, which are designed for a single task, lack the ability to align the words in both the tasks and transfer knowledge across tasks. Lower test accuracy on EQA for most models (Table 4.2) indicates that EQA is more challenging than SGN as it involves

[2] See https://devendrachaplot.github.io/projects/EMML for visualization videos.

Table 4.2: Accuracy of all models on SGN & EQA **test** sets for both *Easy* & *Hard* difficulties.

	Easy				*Hard*			
	No Aux		Aux		No Aux		Aux	
Model	SGN	EQA	SGN	EQA	SGN	EQA	SGN	EQA
Text only	0.2	0.33	0.2	0.33	0.2	0.33	0.2	0.33
Image only	0.20	0.09	0.21	0.08	0.16	0.08	0.15	0.08
Concat	0.33	0.21	0.31	0.19	0.2	0.26	0.39	0.22
GA	0.27	0.18	0.35	0.24	0.18	0.11	0.22	0.24
FiLM	0.24	0.11	0.34	0.12	0.12	0.03	0.25	0.15
PACMAN	0.26	0.12	0.33	0.10	0.29	0.33	0.11	0.27
Dual-Attention	**0.86**	**0.53**	**0.96**	**0.58**	**0.86**	**0.38**	**0.82**	**0.59**

alignment between not only input textual and visual representations but also with the answer space. As expected, using spatial auxiliary tasks lead to better performance for all models (Table 4.2).

Visualizations. Figure 4.9 shows an example indicating that the sentence-level embedding for the question attends to relevant words. It also shows a visualization of spatial-attention maps and answer predictions for each frame in an example EQA episode. The spatial attention map shows that the model attends to relevant objects and attributes based on the question. The answer predictions change as the agent views more objects. These visualizations show that the textual and visual representations are aligned with each other, as well as with the answer space, as expected. In Figure 4.8, we visualize the convolutional network outputs corresponding to 7 words for the same frame for both Aux and No Aux models. As expected, the Aux model predictions are very close to the auxiliary task labels. More interestingly, the convolutional outputs of the No Aux model show that words and objects/properties in the images have been properly aligned even when the model is not trained with any auxiliary task labels.[2]

4.4.1 Ablation tests

We perform a series of ablation tests in order to analyze the contribution of each component in the Dual-Attention unit: without Spatial-Attention (**w/o SA**), without the first Gated-Attention with x_{BoW} (**w/o GA1**), and without the second Gated-Attention with x_{sent} (**w/o GA2**). We also try removing the task indicator variable (**w/o Indicator Variable**), removing reward shaping (**w/o Reward Shaping**), and training the proposed model on a single task, SGN or EQA (**DA Single-Task**).

Figure 4.10 shows the training performance curves for the Dual-Attention model along with all ablation models in the *Easy* Setting. In Table 4.3, we report the test set performance of all ablation models. The results indicate that SA and GA1 contribute the most to the performance of the Dual-Attention model. GA2 is critical for performance on EQA but not SGN (see Table 4.3). This is expected as GA2 is designed to attend to different objects and attributes based on the question and is used mainly for answer prediction. It is not critical for SGN as the spatial attention map consists of locations of relevant objects, which is sufficient for navigating to the correct object. Reward shaping and indicator variable help with learning speed (see Figure 4.10), but have little effect on the final performance (see Table 4.3). Dual-Attention models trained

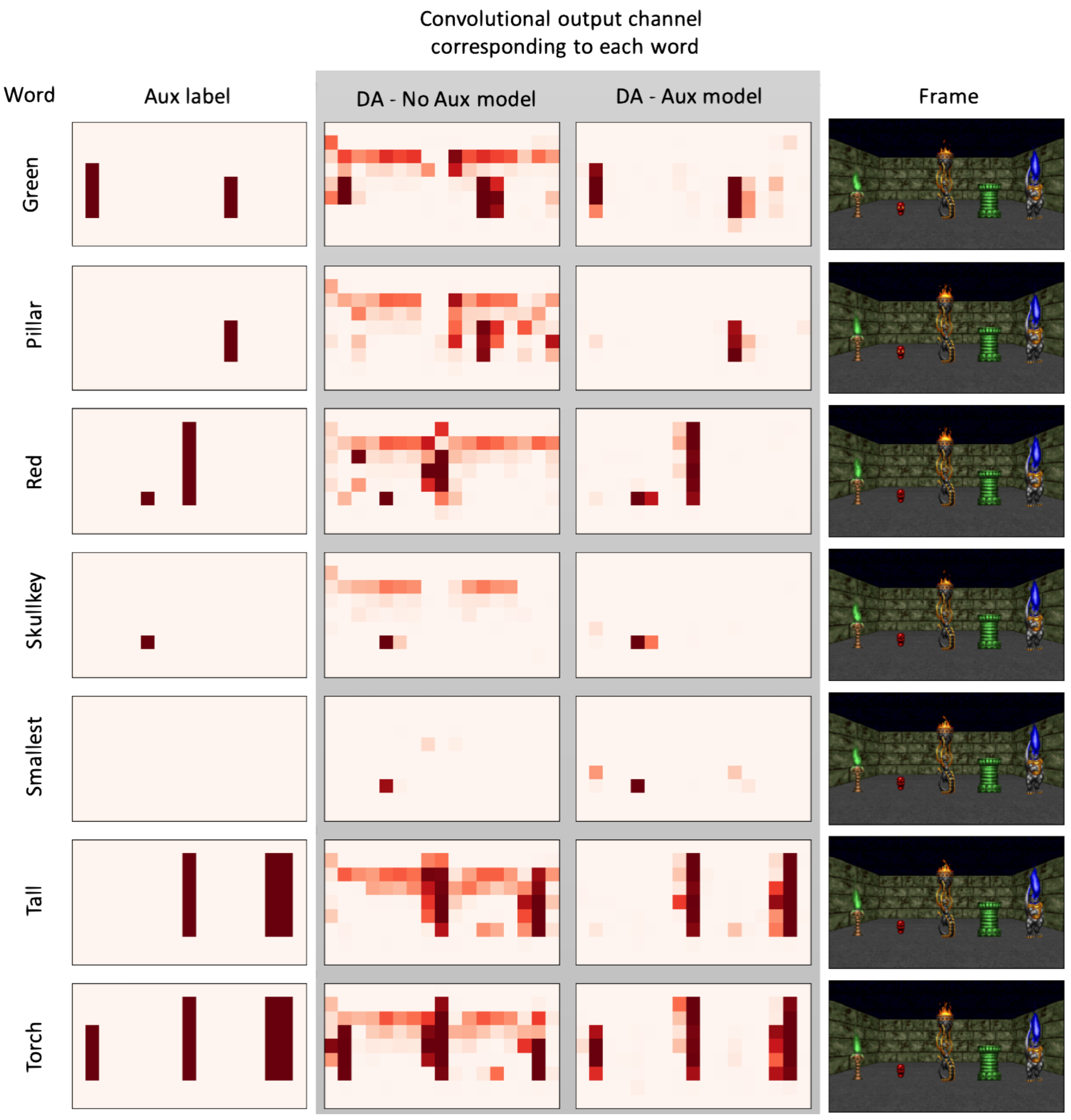

Figure 4.8: **Visualizations of convolutional output channels.** We visualize the convolutional channels corresponding to 7 words (one in each row) for the same frame (shown in the rightmost column). The first column shows the auxiliary task labels for reference. The second column and third column show the output of the corresponding channel for the proposed Dual-Attention model trained without and with auxiliary tasks, respectively. As expected, the Aux model outputs are very close to the auxiliary task labels. The convolutional outputs of the No Aux model show that words and objects/properties in the images have been properly aligned even when the model is not trained with any auxiliary task labels. We do not provide any auxiliary label for words 'smallest' and 'largest' as they are not properties of an object and require relative comparison of objects. The visualizations in row 5 (corresponding to 'smallest') indicate that both models are able to compare the sizes of objects and detect the smallest object in the corresponding output channel even without any aux labels for the smallest object.

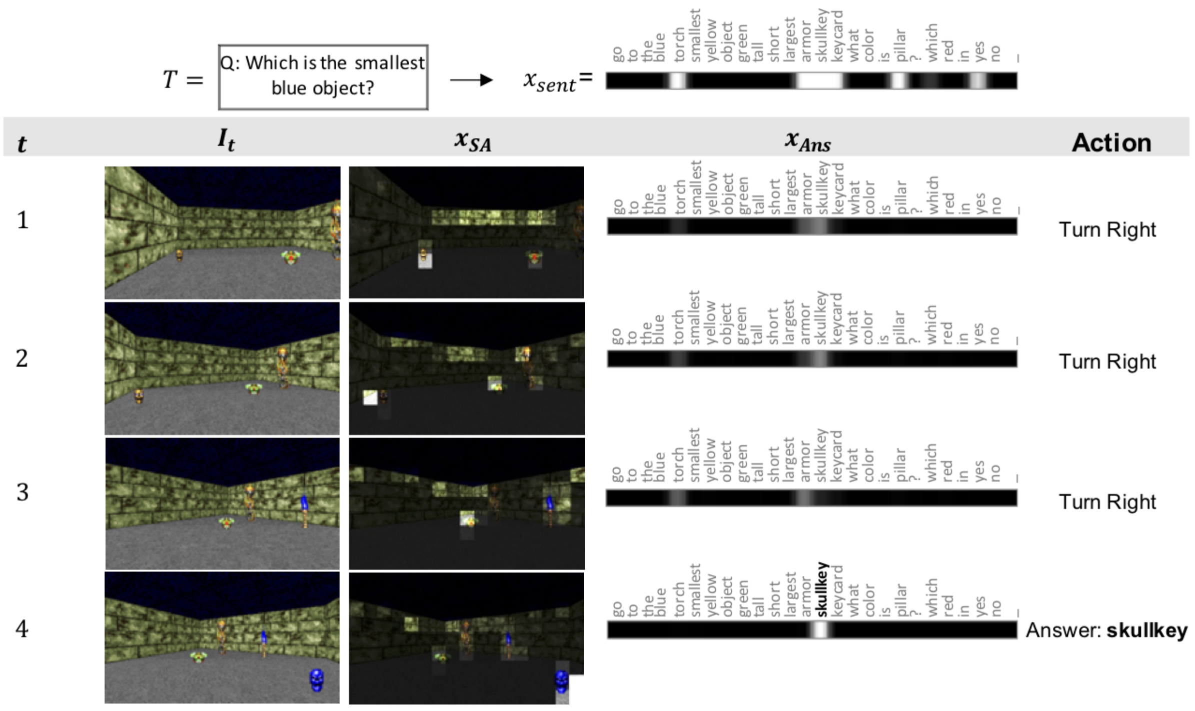

$T =$
Q: Which is the smallest blue object?
$x_{sent}=$
go to the blue torch smallest yellow object green tall short largest armor skullkey keycard what color is pillar ? which red in yes no _
t
I_t
x_{SA}
x_{Ans}
Action
1
Turn Right
2
Turn Right
3
Turn Right
4
Answer: **skullkey**

Figure 4.9: **Spatial Attention and Answer Prediction Visualizations.** An example EQA episode with the question "Which is the smallest blue object?". The sentence embedding of the question is shown on the top (x_{sent}). As expected, the embedding attends to object type words ('torch', 'pillar', 'skullkey', etc.) as the question is asking about an object type ('Which object'). The rows show increasing time steps and columns show the input frame, the input frame overlaid with the spatial attention map, the predicted answer distribution, and the action at each time step. As the agent is turning, the spatial attention attends to small and blue objects. **Time steps 1, 2**: The model is attending to the yellow skullkey but the probability of the answer is not sufficiently high, likely because the skullkey is not blue. **Time step 3**: The model cannot see the skullkey anymore so it attends to the armor which is next smallest object. Consequently, the answer prediction also predicts armor, but the policy decides not to answer due to low probability. **Time step 4**: As the agent turns more, it observes and attends to the blue skullkey. The answer prediction for 'skullkey' has high probability because it is small and blue, so the policy decides to answer the question.

only on single tasks work well on SGN, especially with auxiliary tasks. This is because the auxiliary task for single task models includes object detection labels corresponding to the words in the test set. This highlights a key advantage of the proposed model. Due to its modular and interpretable design, the model can be used for transferring the policy to new objects and attributes without fine-tuning as discussed in the following subsection.

4.4.2 Extension: Transfer to new words

Consider a scenario of SGN where the agent is trained to follow instructions of certain objects and attributes. Suppose that the user wants the agent to follow instructions about a new object such as 'pillar' or a new attribute such the color 'red' which are never seen in any training instruction. Prior SGN models are shown to perform well to unseen combination of object-attribute pairs [Chaplot et al., 2017], but they do not generalize well to instructions containing a new word. The model retrained only on new instructions will lead to catastrophic forgetting of previous

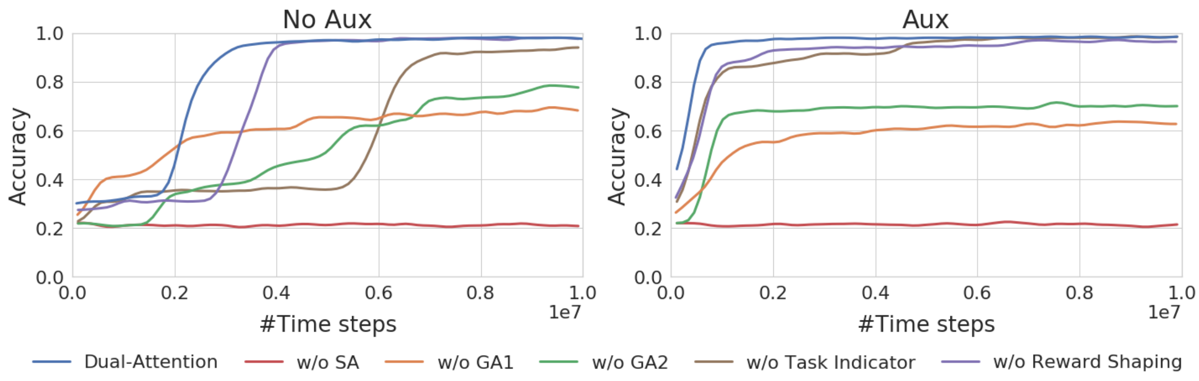

Figure 4.10: Training accuracy of proposed Dual-Attention model with all ablation models trained without (left) and with (right) auxiliary tasks for the *Easy* environment.

Table 4.3: Accuracy of all the ablation models trained with and without Auxiliary tasks on SGN and EQA test sets for the Doom Easy environment.

	No Aux		Aux	
Model	SGN	EQA	SGN	EQA
w/o SA	0.20	0.16	0.20	0.15
w/o GA1	0.14	0.25	0.16	0.38
w/o GA2	0.80	0.33	0.97	0.15
w/o Task Indicator	0.79	0.47	0.96	0.56
w/o Reward Shaping	0.82	0.49	0.93	0.51
DA Single-Task	0.63	0.31	0.91	0.34
DA Multi-Task	0.86	0.53	0.96	0.58

Table 4.4: The performance of a trained policy appended with object detectors on instructions containing unseen words ('red' and 'pillar').

Instruction	Easy	Hard
Go to the **pillar**	1.00	0.71
Go to the **red** object	0.99	0.89
Go to the tall/short **pillar**	0.99	0.68
Go to the <known_color>**pillar**.	1.00	0.79
Go to the **red** <known_object>	1.00	0.93
Go to the largest/smallest **red** object	0.95	0.69
Go to the tall/short **red pillar**	0.99	0.88
Go to the **red pillar**	0.99	0.82

instructions.

In contrast, our model can be used for transfer to new words by training an object detector for each new word and appending it to the image representation x_I. In order to test this, we train a single-task SGN model using the proposed architecture on the training set for instructions. We use auxiliary tasks but only for words in the vocabulary of the instructions training set. After training the policy, we would like the agent to follow instructions containing test words 'red' and 'pillar', which the agent has never seen or received any supervision about how this attribute or object looks visually. For transferring the policy, we assume access to two object detectors which would give object detections for 'red' and 'pillar' separately. We resize the object detections to the size of a feature map in the image representation $(H \times W)$ and append them as channels to the image representation. We also append the words 'red' and 'pillar' to the bag-of-words representations in the same order such that they are aligned with the appended feature maps. We randomly initialize the embeddings of the new words for computing the sentence embedding. The results in Table 4.4 show that this policy generalizes well to different types of instructions with unseen words. This suggests that a trained policy can be scaled to more objects provided the complexity of navigation remains consistent.

4.5 Summary

We proposed a Dual-Attention model for visually-grounded multitask learning which uses Gated- and Spatial-Attention to disentangle attributes in feature representations and align them with the answer space. We show that the proposed model is able to transfer the knowledge of words across tasks and outperforms the baselines on both Semantic Goal Navigation and Embodied Question Answering by a considerable margin. We showed that disentangled and interpretable representations make our model modular and allow for easy addition of new objects or attributes to a trained model. For future work, the model can potentially be extended to transferring knowledge across different domains by using modular interpretable representations of objects which are domain-invariant.

Chapter 5

Conclusion

The recent success of RL algorithms in challenging application domains, including robotic continuous control and video game AI, often relies on the availability of high-quality human supervision. Common forms of supervision include dense rewards and expert demonstrations, but these are often challenging to obtain due to the high cost of human labor and domain expertise, which in turn limits the applicability of RL to many real-world problems. On the other hand, self-supervised RL methods often struggle to scale to complex domains due to sample inefficiency and underfitting. In this thesis, we looked at ways to strike a balance between *self-supervised* and *human-supervised* RL, benefitting from the best of both worlds: the low data requirements and generalizability of self-supervised methods, and the learning efficiency of supervised methods.

Deviating from traditional methods to train RL, we considered alternative modalities of supervision that can be more scalable and easier to acquire. These included a state marginal distribution that informs the agent how it should do exploration for solving a distribution of tasks (Chapter 2); weak semantic labels of images that can be used to learn a structured latent representation for controllable exploration and learning (Chapter 3); and language instructions and questions that specify the agent's task (Chapter 4).

In Chapter 2, we recast exploration as a problem of State Marginal Matching (SMM) between the policy and a target distribution. In particular, the SMM objective provided a framework to understand previous exploration algorithms based on predictive-error and mutual-information as approximately doing distribution matching, potentially explaining their success on hard exploration tasks. Furthermore, we showed how we can amortize the cost of learning to explore by learning a single task-agnostic exploration policy, which can be re-used for solving many downstream tasks.

The latter two chapters of the thesis focused on learning disentangled representations for language, vision and control. In Chapter 3, we introduced structure into the goal-generation process using weak supervision, and demonstrated significant improvement in performance and learning speed over prior visual goal-conditioned RL methods. In Chapter 4, we learned to solve language-specified tasks with an attention architecture that learns to disentangle words with visual entities, and properly align them together. We showed that the explicit disentanglement of representations makes our model modular, interpretable, and enables zero-shot transfer to instructions containing new words by leveraging object detectors.

The takeaway message of this thesis is that combining self-supervised RL with scalable forms of human supervision can make the RL task much easier to learn. By leveraging types of supervision that can be collected at scale, we can greatly improve the learning speed and generalization performance of RL over unsupervised methods. Learning a *structured* latent representation or policy, as we do in Chapter 3, can also enable better safety and controllability of the exploration during training.

5.1 Future Work

While this thesis has proposed different ways to scalably supervise RL agents, there are many unanswered questions regarding how a learning agent can generalize from limited feedback. Below, we outline several directions for future work in the space of *interactive reinforcement learning*—enabling effective and efficient human-agent interaction for training embodied agents.

An effective interactive RL system is critical for broadening the scope of RL applications. A major challenge of training robotic agents in the real-world is the problem of reward specification, which requires knowing the true environment state in order to evaluate the reward function; but state estimation is often difficult in partially observable environments, unless there is a hand-engineered perception system or an extensive instrumentation built around the environment.

How can humans effectively interact with an agent to quickly teach it new tasks and skills? As a motivating example, we consider how a human trainer interacts with a dog for training new tricks. Trainers often provide sparse rewards to the dog using treats or a clicker for positive reinforcement. Dogs are also equipped with motor skills that enable efficient exploration, allowing the human to provide feedback on a diverse set of behaviors. Likewise, we want to create a system that enables easy and accessible human-agent interaction, with the capability of data-efficient learning from human feedback.

What are effective modalities of supervision?

Aside from reward functions, many other sources of supervision signals have been considered within the RL literature. Demonstrations for imitation learning are often obtained from motion capture systems [Kober et al., 2010, Peng et al., 2018, Merel et al., 2018], teleoperation [Zhang et al., 2018b, Mandlekar et al., 2020, DelPreto et al., 2020], and kinesthetic teaching [Guenter et al., 2007, Lee and Ott, 2011, Mülling et al., 2013]. Others have proposed using forms of easy-to-provide supervision that can be scalably collected, such as pairwise preferences between trajectories [Christiano et al., 2017, Lee et al., 2021] and weak semantic labels of images [Lee et al., 2020].

A more intuitive and convenient way for humans to communicate with agents is through *language*. Language is a rich and structured interface that can allow humans to provide instructions, both about the tasks that they want the robot to perform, as well as feedback about how the robot could perform the task better. Prior work that utilized language instructions for visually-grounded RL include behavior cloning approaches using language-action sequence pairs [Anderson et al., 2018, Mei et al., 2016], language-conditioned reward functions [MacGlashan et al., 2015, Bahdanau et al., 2018, Tung et al., 2018, Fu et al., 2019], and methods that convert an instruction into executable actions within the environment [Forbes et al., 2015, Misra et al., 2016, Tellex et al., 2011]. Related to instruction following, Das et al. [2018] propose an embodied question-answering task, where the agent has to explore the surrounding 3D environment in order to find relevant information for answering the given question. Language has also been used for hierarchical abstractions to solve temporally-extended tasks [Jiang et al., 2019]. Language provides a fluid interface between humans and robots that can enable a more seamless collection of supervision for robot learning.

This list is not exhaustive, and there remain many underexplored modes of information that can provide useful supervision signals for the agent. For example, these include visual cues, such as laser pointers, and tactile robotic sensors [Speeter, 1990, Howe, 1993, Dahiya et al., 2009, Chen et al., 2018b]. Moreover, in addition to online supervision, there are also many large offline datasets that can provide rich structured priors about the natural world. For example, there is a large amount of videos and captions, knowledge bases and text, and even offline trajectory data of agents interacting with the environment and performing various tasks. Leveraging these diverse and complex datasets to learn rich representations about the world can enable RL agents to achieve better generalization in real-world tasks. Utilizing offline data can also help RL with its notorious sample inefficiency, reducing the number of environment interactions needed.

Lastly, the user interface for human-agent interaction should support *multimodality*, allowing the agent to learn by processing and relating information from different types of data. Baltrušaitis et al. [2018] provides a survey of recent advances in multimodal machine learning, and summarizes some of the current challenges: (1) How do we *represent* multimodal data?, (2) How do we *translate* and *align* data between modalities?, and (3) How do we *fuse* and *transfer* knowledge between modalities? Within the RL literature, in addition to the prior work on visually-grounded RL (*i.e.*, combining visual and textual information), there has been recent work on sensor fusion for robotics [Liu et al., 2017, Song et al., 2021], as well as using audio-visual association for exploration [Dean et al., 2020].

Interdependence between Exploration & Human-Agent Interaction

In the interactive RL setting, efficient exploration is critical for a number of reasons. Firstly, an exploratory policy that produces diverse behavior can allow the human to provide more meaningful feedback. Recent work has shown that efficient exploration can substantially improve the learning efficiency of interactive RL, reducing the total number of feedback samples needed [Li et al., 2019, Lee et al., 2021]. Secondly, human supervision can be often imperfect in the real world, in which case the agent has to try to extrapolate and learn a more optimal behavior. For example, Brown et al. [2019] addresses the limiting inability of imitation learning to learn a policy that outperforms the given demonstrations, and proposes using a set of ranked demonstrations in order to extrapolate beyond a set of suboptimal demonstrations. Lastly, given that human feedback is often noisy, inconsistent, and delayed in practice [Knox and Stone, 2009, Faulkner et al., 2020], we can use the notion of uncertainty about the true underlying reward to drive exploration and learning. The delicate interdependence between exploration and human-agent interaction, especially in complex, high-dimensional domains, is a relatively understudied but important topic.

To conclude, we listed some of the next big frontiers towards effective, efficient, and accessible training of embodied AI agents. For example: How do we extrapolate beyond suboptimal demonstrations, underspecified rewards, or noisy human feedback? Aside from rewards and demonstrations, what are alternative modalities of supervision for RL that are scalable to collect, and can provide useful and dense learning signals for the agent? How can RL agents scale in complexity beyond the specified training tasks, generalize learned skills to new tasks, and continually adapt to new situations after deployment? To address these challenges, we encourage research to push beyond traditional frameworks for RL, *e.g.*, by redefining how agents are supervised, or considering optimization objectives different from reward maximization for training a policy.

Appendix **A**

Appendix

A.1 Task-Agnostic Exploration via State Marginal Matching

A.1.1 Environment Parameters

We summarize the environment parameters for *Navigation*, *Fetch*, and *D'Claw* in Table A.1.

A.1.2 Algorithm Hyperparameters

We summarize hyperparameter settings in Table A.2. All algorithms were trained for 1e6 steps on *Fetch*, 1e6 steps on *D'Claw* Sim2Real, 1e5 steps on *D'Claw* hardware, and 1e5 steps on *Navigation*.

Loss Hyperparameters. For each exploration method, we tuned the weights of the different loss components. *SAC reward scale* controls the weight of the action entropy reward relative to the extrinsic reward. *Count coeff* controls the intrinsic count-based exploration reward w.r.t. the extrinsic reward and SAC action entropy reward. Similarly, *Pseudocount coeff* controls the intrinsic pseudocount exploration reward. *SMM coeff for* $\mathcal{H}[s \mid z]$ *and* $\mathcal{H}[z \mid s]$ control the weight of the different loss components (state entropy and latent conditional entropy) of the SMM objective in Eq. 2.3.

Historical Averaging. In the *Fetch* experiments, we tried the following sampling strategies for historical averaging: (1) *Uniform*: Sample policies uniformly across training iterations. (2) *Exponential*: Sample policies, with recent policies sampled exponentially more than earlier ones. (3) *Last*: Sample the N latest policies uniformly at random. We found that *Uniform* worked less well, possibly due to the policies at early iterations not being trained enough. We found negligible difference in the state entropy metric between *Exponential* vs. *Last*, and between sampling 5 vs. 10 historical policies, and we also note that it is unnecessary to keep checkpoints from every iteration.

GAIL Hyperparameters: The replay buffer is filled with 1e4 random actions before training, for training stability. We perform one discriminator update per SAC update. For both *Fetch* and *D'Claw*, we used 1e4 states sampled from $p^*(s)$. Other hyperparameter settings, such as batch size for both discriminator and policy updates, are summarized in Table A.2. We observed that GAIL training is more unstable compared to the exploration baselines. Thus,

Table A.1: **Environment parameters** specifying the observation space dimension $|\mathcal{S}|$; action space dimension $|\mathcal{A}|$; max episode length T; the environment reward, related to the target distribution by $\exp\{r_{\text{env}}(s)\} \propto p^*(s)$, and other environment parameters.

Environment	$\|\mathcal{S}\|$	$\|\mathcal{A}\|$	T	Env Reward ($\log p^*(s)$)	Other Parameters	Figures
Navigation	2	2	100	Uniform over all m halls	# Halls: 3, 5, 7 Hall length: 10	2.9a, 2.9b
				Uniform over all m halls	# Halls: 3 Hall length: 50	2.9c
Fetch	25	4	50	Uniform block pos. over table surface		2.6a, 2.5, 2.8, 2.10, 2.12
				More block pos. density on left-half of table		2.11
D'Claw	12	9	50	Uniform object angle over $[-180°, 180°]$		2.6b, 2.7

for GAIL, we did not take the final iterate (e.g., policy at convergence) but instead used early termination (e.g., take the best iterate according to the state entropy metric).

A.2 Weakly-Supervised RL for Controllable Behavior

We provide implementation details for the experimental setup and algorithms.

A.2.1 Algorithm implementation details

Disentangled representation. We describe the disentangled model network architecture in Table A.4, which was slightly modified from Shu et al. [2019] to be trained on 48×48 image observations from the Sawyer manipulation environments. The encoder is not trained jointly with the generator, and is only trained on generated data from $G(z)$ (see Eq. 3.1). All models were trained using Adam optimizer with $\beta_1 = 0.5$, $\beta_2 = 0.999$, learning rate 1e-3, and batch size 64 for 1e5 iterations. The learned disentangled representation is fixed during RL training (Phase 2 in Figure 3.3).

Goal-conditioned RL. The policy and Q-functions each are feedforward networks with (400, 300) hidden sizes and ReLU activation. All policies were trained using Soft Actor-Critic [Haarnoja et al., 2018] with batch size 1024, discount factor 0.99, reward scale 1, and replay buffer size 1e5. The episodic horizon length was set to 50 for *Push* and *Pickup* environments, and 100 for *Door* environments. We used the default hyperparameters for SkewFit from Pong et al. [2019], which uses 10 latent samples for estimating density. For WSC, we relabelled between 0.2 and 0.5 goals with $z_g \sim p(\mathcal{Z}_\mathcal{I})$ (see Table A.3). All RL methods (WSC, SkewFit, RIG, HER) relabel 20% of goals with a future state in the trajectory. SkewFit and RIG additionally relabel 50% of goals with $z_g \sim p^{\text{skew}}(s)$ and $z_g \sim \mathcal{N}(0, I)$, respectively.

VAE. The VAE was pre-trained on the images from the weakly-labelled dataset for 1000 epochs, then trained on environment observations during RL training. We trained the VAE and the policy separately as was done in Pong et al. [2019], and found that jointly training them end-to-end did not perform well. We used learning rate 1e-3, KL regularization coefficient $\beta \in \{20, 30\}$, and batch size 128. The VAE network architecture and hyperparameters are summarized in Table A.5.

SkewFit+pred (Section 3.4.1): We added a dense layer on top of the VAE encoder to predict the factor values, and added a MSE prediction loss to the β-VAE loss. We also tried using the last hidden layer of the VAE encoder instead of the encoder output, but found that it did not perform well.

SkewFit+DR (Figure 3.6): We tried with and without adding the VAE distance reward to the disentangled reward $R_{z_g}(s)$ in Eq. 3.3, and report the best α^{VAE} in Table A.3:

$$R^{\text{DR}}(s) = R_{z_g}(s) - \alpha^{\text{VAE}} \| e^{\text{VAE}}(s) - z_g^{\text{VAE}} \| \tag{A.1}$$

Table A.2: **Hyperparameter settings**. Hyperparameters were chosen according to the following eval metrics: *Fetch-Uniform*: State entropy of the discretized gripper and block positions (bin size 0.05), after rolling out the trained policy for 50K env steps. *Fetch-Half*: $D_{\text{KL}}(p^*(s) \parallel \rho_\pi(s))$ and $\text{TV}(p^*(s), \rho_\pi(s))$ of the discretized gripper and block positions (bin size 0.01), after rolling out the trained policy for 50K env steps. *2D Navigation*: State entropy of the discretized XY-positions of the trained policy. *D'Claw*: State entropy of the object angle.

Environment	**Algorithm**	**Hyperparameters Used**	**Hyperparameters Considered**
All	SMM, SAC, ICM, Count, Pseudocount	Batch size: 128 1e6 env training steps RL discount: 0.99 Network size: 300 Policy lr: 3e-4 Q-function lr: 3e-4 Value function lr: 3e-4	N/A (Default SAC hyperparameters)
	GAIL	1e6 env training steps Policy lr: 1e-5 Critic lr: 1e-3 # Random actions before training: 1e4 Network size: 256	N/A (Default GAIL hyperparameters)
Navigation	SMM, SAC	SAC reward scale: 25	SAC reward scale: 1e-2, 0.1, 1, 10, 25, 100
	SMM	SMM $\mathcal{H}[s \mid z]$ coeff: 1 SMM $\mathcal{H}[z \mid s]$ coeff: 1	SMM $\mathcal{H}[s \mid z]$ coeff: 1e-3, 1e-2, 1e-1, 1, 10 SMM $\mathcal{H}[z \mid s]$ coeff: 1e-3, 1e-2, 1e-1, 1, 10
Fetch-Uniform	SMM	Num skills: 4 VAE lr: 1e-2 SMM $\mathcal{H}[s \mid z]$ coeff: 1 SMM $\mathcal{H}[z \mid s]$ coeff: 1 HA sampling: Exponential # HA policies: 10 SMM Latent Prior Coeff: 1	Num skills: 1, 2, 4, 8, 16 VAE lr: 1e-4, 1e-3, 1e-2 HA sampling: Exponential, Uniform, Last # HA policies: 5, 10 SMM Latent Prior Coeff: 1, 4
	SAC	SAC reward scale: 0.1	SAC reward scale: 0.1, 1, 10, 100
	Count	Count coeff: 10 Histogram bin width: 0.05	Count coeff: 0.1, 1, 10
	Pseudocount	Pseudocount coeff: 1 VAE lr: 1e-2	Pseudocount coeff: 0.1, 1, 10 (Use same VAE lr as SMM)
	ICM	Learning rate: 1e-3	Learning rate: 1e-4, 1e-3, 1e-2
	GAIL	Batch size: 512 # SAC updates per step: 1 Discriminator input: s Training iterate: 1e6 # State Samples: 1e4	Batch size: 128, 512, 1024 # SAC updates per step: 1, 4 Discriminator input: s, s_{object}, $\{s_{\text{object}}, s_{\text{robot}}\}$ Training iterate: 1e5, 2e5, 3e5, …, 9e5, 1e6 # State Samples: 1e4
Fetch-Half	SMM, SAC, ICM, Count	SAC reward scale: 0.1	(Best reward scale for *Fetch-Uniform*)
	SMM	Num skills: 4 SMM $\mathcal{H}[s \mid z]$ coeff: 1 SMM $\mathcal{H}[z \mid s]$ coeff: 1	Num skills: 1, 2, 4, 8
	Count	Count coeff: 10 Histogram bin width: 0.05	Count coeff: 0.1, 1, 10
	ICM	Learning rate: 1e-3	Learning rate: 1e-4, 1e-3, 1e-2
D'Claw	SMM, SAC	SAC reward scale: 5	SAC reward scale: 1e-2, 0.1, 1, 5, 10, 100
	SMM	SMM $\mathcal{H}[s \mid z]$ coeff: 250	SMM $\mathcal{H}[s \mid z]$ coeff: 1, 10, 100, 250, 500, 1e3
	Count	Count coeff: 1 Histogram bin width: 0.05	Count coeff: 1, 10 Histogram bin width: 0.05, 0.1
	Pseudocount	Pseudocount coeff: 1 VAE lr: 1e-3	Pseudocount coeff: 1, 10 VAE lr: 1e-1, 1e-2, 1e-3
	ICM	Learning rate: 1e-3 VAE lr: 1e-1	Learning rate: 1e-2, 1e-3, 1e-4 VAE lr: 1e-1, 1e-2, 1e-3
	GAIL	Batch size: 512 # SAC updates per step: 4 Discriminator input: s_{object} Training iterate: 1e5 # State Samples: 1e4	Batch size: 128, 512, 1024 # SAC updates per step: 1, 4 Discriminator input: s, s_{object} Training iterate: 1e5, 2e5, 3e5, …, 9e5, 1e6 # State Samples: 1e4

Environment	M	Factors (**User-specified factor indices are bolded**)	WSC p_{goal}	α^{DR}
Push $n = 1$	256	hand_x, hand_y, **obj_x**, **obj_y**	0.2	1
Push $n = 2$	256	hand_x, hand_y, **obj1_x**, **obj1_y**, obj2_x, obj2_y	0.3	1
Push $n = 3$	512	hand_x, hand_y, **obj1_x**, **obj1_y**, obj2_x, obj2_y, obj3_x, obj3_y	0.4	0
PushLights $n = 1$	256	hand_x, hand_y, **obj_x**, **obj_y**, light	0.4	1
PushLights $n = 2$	512	hand_x, hand_y, **obj1_x**, **obj1_y**, obj2_x, obj2_y, light	0.4	1
PushLights $n = 3$	512	hand_x, hand_y, **obj1_x**, **obj1_y**, obj2_x, obj2_y, obj3_x, obj3_y, light	0.5	0
Pickup	512	hand_y, hand_z, **obj_y**, **obj_z**	0.4	–
PickupLights	512	hand_y, hand_z, **obj_y**, **obj_z**, light	0.3	–
PickupColors	512	hand_y, hand_z, **obj_y**, **obj_z**, table_color, obj_color	0.4	–
PickupLightsColors	512	hand_y, hand_z, **obj_y**, **obj_z**, light, table_color, obj_color	0.3	–
Door	512	**door_angle**	0.3	–
DoorLights	512	**door_angle**, light	0.5	–

Table A.3: **Environment-specific hyperparameters**: M is the number of training images. "WSC p_{goal}" is the percentage of relabelled goals in WSC (Alg. 3). α^{DR} is the VAE reward coefficient for SkewFit+DR in Eq. A.1.

Encoder $\mathcal{N}(z; \mu(s), \sigma(s))$	Generator $G(z)$	Discriminator Body	Discriminator $D(s_1, s_2, y)$
Input: $48 \times 48 \times 3$ image	Input: $z \in \mathbb{R}^K$	Input: $48 \times 48 \times 3$ image	Input: Weakly-labelled data $(s_1, s_2, y) \in \mathcal{D}$
4×4 Conv, 32 ch, str 2	128 Dense layer	4×4 Conv, 32 ch, str 2	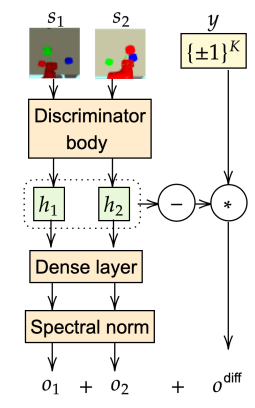 s_1 s_2 y $\{\pm 1\}^K$ Discriminator body h_1 h_2 $-$ $*$ Dense layer Spectral norm o_1 + o_2 + o^{diff}
Spectral norm	Batch norm	Spectral norm	
LeakyReLU	ReLU	LeakyReLU	
4×4 Conv, 32 ch, str 2	$3 \cdot 3 \cdot 64$ Dense layer	4×4 Conv, 32 ch, str 2	
Spectral norm	Batch norm	Spectral norm	
LeakyReLU	ReLU	LeakyReLU	
4×4 Conv, 64 ch, str 2	Reshape $3 \times 3 \times 64$	4×4 Conv, 64 ch, str 2	
Spectral norm	3×3 Conv, 32 ch, str 2	Spectral norm	
LeakyReLU	Batch norm	LeakyReLU	
4×4 Conv, 64 ch, str 2	LeakyReLU	4×4 Conv, 64 ch, str 2	
Spectral norm	3×3 Conv, 16 ch, str 2	Spectral norm	
LeakyReLU	Batch norm	LeakyReLU	
Flatten	LeakyReLU	Flatten	
128 Dense layer	6×6 Conv, 3 ch, str 4	256 Dense layer	
Spectral norm	Batch norm	Spectral norm	
LeakyReLU	Sigmoid	LeakyReLU	
$2 \cdot K$ Dense layer	Output: $48 \times 48 \times 3$ image	256 Dense layer	
Output: $\mu, \sigma \in \mathbb{R}^K$		Spectral norm	
		LeakyReLU	
		Output: Hidden layer h	Output: Prediction $o_1 + o_2 + o^{\text{diff}} \in [0, 1]$

Table A.4: **Disentangled representation model architecture**: We slightly modified the disentangled model architecture from Shu et al. [2019] for 48 × 48 image observations. The discriminator body is applied separately to s_1 and s_2 to compute the unconditional logits o_1 and o_2 respectively, and the conditional logit is computed as $o^{\text{diff}} = y \cdot (h_1 - h_2)$, where h_1, h_2 are the hidden layers and $y \in \{\pm 1\}$.

VAE encoder $\mathcal{N}(z; \mu(s), \sigma(s))$	VAE decoder
Input: $48 \times 48 \times 3$ image	Input: $z \in \mathbb{R}^{L^{\text{VAE}}}$
5×5 Conv, 16 ch, str 2	$3 \cdot 3 \cdot 64$ Dense layer
ReLU	Reshape $3 \times 3 \times 64$
3×3 Conv, 32 ch, str 2	3×3 Conv, 32 ch, str 2
ReLU	ReLU
3×3 Conv, 64 ch, str 2	3×3 Conv, 16 ch, str 2
ReLU	ReLU
Flatten	Output: $48 \times 48 \times 3$ image
$2 \cdot L^{\text{VAE}}$ Dense layer	
Output: $\mu, \sigma \in \mathbb{R}^{L^{\text{VAE}}}$	

Env	β	Best latent dim L^{VAE} WSC	SkewFit, RIG, HER
Push	20	256	4
Pickup	30	256	16
Door	20	256	16

Table A.5: **VAE architecture & hyperparameters**: β is the KL regularization coefficient in the β-VAE loss. We found that a smaller VAE latent dim $L^{\text{VAE}} \in \{4, 16\}$ worked best for SkewFit, RIG, and HER (which use the VAE for both hindsight relabelling and for the actor & critic networks), but a larger dim $L^{\text{VAE}} = 256$ benefitted WSC (which only uses the VAE for the actor & critic networks).

Bibliography

Abbas Abdolmaleki, Jost Tobias Springenberg, Yuval Tassa, Remi Munos, Nicolas Heess, and Martin Riedmiller. Maximum a posteriori policy optimisation. *arXiv preprint arXiv:1806.06920*, 2018.

Joshua Achiam, Harrison Edwards, Dario Amodei, and Pieter Abbeel. Variational option discovery algorithms. *arXiv preprint arXiv:1807.10299*, 2018.

David Barber Felix Agakov. The im algorithm: a variational approach to information maximization. *Advances in Neural Information Processing Systems*, 16:201, 2004.

Pulkit Agrawal, Ashvin V Nair, Pieter Abbeel, Jitendra Malik, and Sergey Levine. Learning to poke by poking: Experiential learning of intuitive physics. In *Advances in neural information processing systems*, pages 5074–5082, 2016.

Michael Ahn, Henry Zhu, Kristian Hartikainen, Hugo Ponte, Abhishek Gupta, Sergey Levine, and Vikash Kumar. Robel: Robotics benchmarks for learning with low-cost robots. *arXiv preprint arXiv:1909.11639*, 2019.

Maruan Al-Shedivat, Lisa Lee, Ruslan Salakhutdinov, and Eric Xing. On the complexity of exploration in goal-driven navigation. *arXiv preprint arXiv:1811.06889*, 2018.

Peter Anderson, Qi Wu, Damien Teney, Jake Bruce, Mark Johnson, Niko Sünderhauf, Ian Reid, Stephen Gould, and Anton van den Hengel. Vision-and-language navigation: Interpreting visually-grounded navigation instructions in real environments. In *Proceedings of the IEEE Conference on Computer Vision and Pattern Recognition*, pages 3674–3683, 2018.

Marcin Andrychowicz, Filip Wolski, Alex Ray, Jonas Schneider, Rachel Fong, Peter Welinder, Bob McGrew, Josh Tobin, OpenAI Pieter Abbeel, and Wojciech Zaremba. Hindsight experience replay. In *Advances in Neural Information Processing Systems*, pages 5048–5058, 2017.

Dzmitry Bahdanau, Felix Hill, Jan Leike, Edward Hughes, Pushmeet Kohli, and Edward Grefenstette. Learning to follow language instructions with adversarial reward induction. *arXiv preprint arXiv:1806.01946*, 2018.

Tadas Baltrušaitis, Chaitanya Ahuja, and Louis-Philippe Morency. Multimodal machine learning: A survey and taxonomy. *IEEE transactions on pattern analysis and machine intelligence*, 41 (2):423–443, 2018.

André Barreto, Will Dabney, Rémi Munos, Jonathan J Hunt, Tom Schaul, Hado P van Hasselt, and David Silver. Successor features for transfer in reinforcement learning. In *Advances in neural information processing systems*, pages 4055–4065, 2017.

Marc Bellemare, Sriram Srinivasan, Georg Ostrovski, Tom Schaul, David Saxton, and Remi Munos. Unifying count-based exploration and intrinsic motivation. In *Advances in Neural Information Processing Systems*, pages 1471–1479, 2016.

Emmanuel Bengio, Valentin Thomas, Joelle Pineau, Doina Precup, and Yoshua Bengio. Independently controllable features. *arXiv preprint arXiv:1703.07718*, 2017.

Christopher Berner, Greg Brockman, Brooke Chan, Vicki Cheung, Przemyslaw Debiak, Christy Dennison, David Farhi, Quirin Fischer, Shariq Hashme, Chris Hesse, et al. Dota 2 with large scale deep reinforcement learning. *arXiv preprint arXiv:1912.06680*, 2019.

Daniel S Brown, Wonjoon Goo, Prabhat Nagarajan, and Scott Niekum. Extrapolating beyond suboptimal demonstrations via inverse reinforcement learning from observations. *arXiv preprint arXiv:1904.06387*, 2019.

G. Brown. Iterative solution of games by fictitious play. *Activity Analysis of Production and Allocation*, 1951.

Yuri Burda, Harrison Edwards, Amos Storkey, and Oleg Klimov. Exploration by random network distillation. *arXiv preprint arXiv:1810.12894*, 2018.

Devendra Singh Chaplot, Kanthashree Mysore Sathyendra, Rama Kumar Pasumarthi, Dheeraj Rajagopal, and Ruslan Salakhutdinov. Gated-attention architectures for task-oriented language grounding. *arXiv preprint arXiv:1706.07230*, 2017.

Devendra Singh Chaplot, Lisa Lee, Ruslan Salakhutdinov, Devi Parikh, and Dhruv Batra. Embodied multimodal multitask learning. *International Joint Conference on Artificial Intelligence (IJCAI)*, 2020.

Junxiang Chen and Kayhan Batmanghelich. Weakly supervised disentanglement by pairwise similarities. *arXiv preprint arXiv:1906.01044*, 2019.

Tian Qi Chen, Xuechen Li, Roger B Grosse, and David K Duvenaud. Isolating sources of disentanglement in variational autoencoders. In *Advances in Neural Information Processing Systems*, pages 2610–2620, 2018a.

Wei Chen, Heba Khamis, Ingvars Birznieks, Nathan F Lepora, and Stephen J Redmond. Tactile sensors for friction estimation and incipient slip detection—toward dexterous robotic manipulation: A review. *IEEE Sensors Journal*, 18(22):9049–9064, 2018b.

Xi Chen, Yan Duan, Rein Houthooft, John Schulman, Ilya Sutskever, and Pieter Abbeel. Infogan: Interpretable representation learning by information maximizing generative adversarial nets. In *Advances in neural information processing systems*, pages 2172–2180, 2016.

Nuttapong Chentanez, Andrew G Barto, and Satinder P Singh. Intrinsically motivated reinforcement learning. In *Advances in neural information processing systems*, pages 1281–1288, 2005.

Kyunghyun Cho, Bart Van Merriënboer, Dzmitry Bahdanau, and Yoshua Bengio. On the properties of neural machine translation: Encoder-decoder approaches. *arXiv preprint arXiv:1409.1259*, 2014.

Paul F Christiano, Jan Leike, Tom Brown, Miljan Martic, Shane Legg, and Dario Amodei. Deep reinforcement learning from human preferences. In *Advances in Neural Information Processing Systems*, pages 4299–4307, 2017.

John D Co-Reyes, YuXuan Liu, Abhishek Gupta, Benjamin Eysenbach, Pieter Abbeel, and Sergey Levine. Self-consistent trajectory autoencoder: Hierarchical reinforcement learning with trajectory embeddings. *arXiv preprint arXiv:1806.02813*, 2018.

Cédric Colas, Olivier Sigaud, and Pierre-Yves Oudeyer. Curious: Intrinsically motivated multi-task, multi-goal reinforcement learning. *arXiv preprint arXiv:1810.06284*, 2018.

Ravinder S Dahiya, Giorgio Metta, Maurizio Valle, and Giulio Sandini. Tactile sensing—from humans to humanoids. *IEEE transactions on robotics*, 26(1):1–20, 2009.

Abhishek Das, Samyak Datta, Georgia Gkioxari, Stefan Lee, Devi Parikh, and Dhruv Batra. Embodied question answering. *arXiv preprint arXiv:1711.11543*, 2017.

Abhishek Das, Samyak Datta, Georgia Gkioxari, Stefan Lee, Devi Parikh, and Dhruv Batra. Embodied question answering. In *Proceedings of the IEEE Conference on Computer Vision and Pattern Recognition*, pages 1–10, 2018.

Sudeep Dasari, Frederik Ebert, Stephen Tian, Suraj Nair, Bernadette Bucher, Karl Schmeckpeper, Siddharth Singh, Sergey Levine, and Chelsea Finn. Robonet: Large-scale multi-robot learning. *arXiv preprint arXiv:1910.11215*, 2019.

Constantinos Daskalakis and Qinxuan Pan. A counter-example to karlin's strong conjecture for fictitious play. In *2014 IEEE 55th Annual Symposium on Foundations of Computer Science*, pages 11–20. IEEE, 2014.

Victoria Dean, Shubham Tulsiani, and Abhinav Gupta. See, hear, explore: Curiosity via audio-visual association. *arXiv preprint arXiv:2007.03669*, 2020.

Joseph DelPreto, Jeffrey I Lipton, Lindsay Sanneman, Aidan J Fay, Christopher Fourie, Changhyun Choi, and Daniela Rus. Helping robots learn: a human-robot master-apprentice model using demonstrations via virtual reality teleoperation. In *2020 IEEE International Conference on Robotics and Automation (ICRA)*, pages 10226–10233. IEEE, 2020.

Nat Dilokthanakul, Christos Kaplanis, Nick Pawlowski, and Murray Shanahan. Feature control as intrinsic motivation for hierarchical reinforcement learning. *IEEE transactions on neural networks and learning systems*, 30(11):3409–3418, 2019.

Alexey Dosovitskiy and Vladlen Koltun. Learning to act by predicting the future. *arXiv preprint arXiv:1611.01779*, 2016.

Yan Duan, John Schulman, Xi Chen, Peter L Bartlett, Ilya Sutskever, and Pieter Abbeel. Rl$\hat{2}$: Fast reinforcement learning via slow reinforcement learning. *arXiv preprint arXiv:1611.02779*, 2016.

Yan Duan, Marcin Andrychowicz, Bradly Stadie, OpenAI Jonathan Ho, Jonas Schneider, Ilya Sutskever, Pieter Abbeel, and Wojciech Zaremba. One-shot imitation learning. In *Advances in neural information processing systems*, pages 1087–1098, 2017.

Babak Esmaeili, Hao Wu, Sarthak Jain, Alican Bozkurt, Narayanaswamy Siddharth, Brooks Paige, Dana H Brooks, Jennifer Dy, and Jan-Willem van de Meent. Structured disentangled representations. *arXiv preprint arXiv:1804.02086*, 2018.

Benjamin Eysenbach, Abhishek Gupta, Julian Ibarz, and Sergey Levine. Diversity is all you need: Learning skills without a reward function. *arXiv preprint arXiv:1802.06070*, 2018.

Taylor A Kessler Faulkner, Elaine Schaertl Short, and Andrea L Thomaz. Interactive reinforcement learning with inaccurate feedback. In *2020 IEEE International Conference on Robotics and Automation (ICRA)*, pages 7498–7504. IEEE, 2020.

Chelsea Finn and Sergey Levine. Deep visual foresight for planning robot motion. In *2017 IEEE International Conference on Robotics and Automation (ICRA)*, pages 2786–2793. IEEE, 2017.

Chelsea Finn, Sergey Levine, and Pieter Abbeel. Guided cost learning: Deep inverse optimal control via policy optimization. In *International Conference on Machine Learning*, pages 49–58, 2016a.

Chelsea Finn, Xin Yu Tan, Yan Duan, Trevor Darrell, Sergey Levine, and Pieter Abbeel. Deep spatial autoencoders for visuomotor learning. In *2016 IEEE International Conference on Robotics and Automation (ICRA)*, pages 512–519. IEEE, 2016b.

Chelsea Finn, Pieter Abbeel, and Sergey Levine. Model-agnostic meta-learning for fast adaptation of deep networks. In *Proceedings of the 34th International Conference on Machine Learning-Volume 70*, pages 1126–1135. JMLR. org, 2017.

Maxwell Forbes, Rajesh PN Rao, Luke Zettlemoyer, and Maya Cakmak. Robot programming by demonstration with situated spatial language understanding. In *2015 IEEE International Conference on Robotics and Automation (ICRA)*, pages 2014–2020. IEEE, 2015.

Meire Fortunato, Mohammad Gheshlaghi Azar, Bilal Piot, Jacob Menick, Ian Osband, Alex Graves, Vlad Mnih, Remi Munos, Demis Hassabis, Olivier Pietquin, et al. Noisy networks for exploration. *arXiv preprint arXiv:1706.10295*, 2017.

Justin Fu, Katie Luo, and Sergey Levine. Learning robust rewards with adversarial inverse reinforcement learning. *arXiv preprint arXiv:1710.11248*, 2017.

Justin Fu, Katie Luo, and Sergey Levine. Learning robust rewards with adverserial inverse reinforcement learning. In *International Conference on Learning Representations*, 2018a. URL https://openreview.net/forum?id=rkHywl-A-.

Justin Fu, Avi Singh, Dibya Ghosh, Larry Yang, and Sergey Levine. Variational inverse control with events: A general framework for data-driven reward definition. In *Advances in Neural Information Processing Systems*, pages 8538–8547, 2018b.

Justin Fu, Anoop Korattikara, Sergey Levine, and Sergio Guadarrama. From language to goals: Inverse reinforcement learning for vision-based instruction following. *arXiv preprint arXiv:1902.07742*, 2019.

Akira Fukui, Dong Huk Park, Daylen Yang, Anna Rohrbach, Trevor Darrell, and Marcus Rohrbach. Multimodal compact bilinear pooling for visual question answering and visual grounding. *arXiv preprint arXiv:1606.01847*, 2016.

Aviv Gabbay and Yedid Hoshen. Latent optimization for non-adversarial representation disentanglement. *arXiv preprint arXiv:1906.11796*, 2019.

Carles Gelada, Saurabh Kumar, Jacob Buckman, Ofir Nachum, and Marc G Bellemare. Deepmdp: Learning continuous latent space models for representation learning. *arXiv preprint arXiv:1906.02736*, 2019.

Seyed Kamyar Seyed Ghasemipour, Richard Zemel, and Shixiang Gu. A divergence minimization perspective on imitation learning methods. *Conference on Robot Learning (CoRL)*, 2019.

Leilani H Gilpin, David Bau, Ben Z Yuan, Ayesha Bajwa, Michael Specter, and Lalana Kagal. Explaining explanations: An overview of interpretability of machine learning. In *2018 IEEE 5th International Conference on data science and advanced analytics (DSAA)*, pages 80–89. IEEE, 2018.

Xavier Glorot, Antoine Bordes, and Yoshua Bengio. Deep sparse rectifier neural networks. In *Proceedings of the fourteenth international conference on artificial intelligence and statistics*, pages 315–323, 2011.

Daniel Gordon, Aniruddha Kembhavi, Mohammad Rastegari, Joseph Redmon, Dieter Fox, and Ali Farhadi. Iqa: Visual question answering in interactive environments. In *Proceedings of the IEEE Conference on Computer Vision and Pattern Recognition*, pages 4089–4098, 2018.

Anirudh Goyal, Riashat Islam, Daniel Strouse, Zafarali Ahmed, Matthew Botvinick, Hugo Larochelle, Sergey Levine, and Yoshua Bengio. Infobot: Transfer and exploration via the information bottleneck. *arXiv preprint arXiv:1901.10902*, 2019.

Shixiang Gu, Ethan Holly, Timothy Lillicrap, and Sergey Levine. Deep reinforcement learning for robotic manipulation with asynchronous off-policy updates. In *2017 IEEE international conference on robotics and automation (ICRA)*, pages 3389–3396. IEEE, 2017.

Florent Guenter, Micha Hersch, Sylvain Calinon, and Aude Billard. Reinforcement learning for imitating constrained reaching movements. *Advanced Robotics*, 21(13):1521–1544, 2007.

Abhishek Gupta, Russell Mendonca, YuXuan Liu, Pieter Abbeel, and Sergey Levine. Meta-reinforcement learning of structured exploration strategies. In *Advances in Neural Information Processing Systems*, pages 5302–5311, 2018.

Saurabh Gupta, James Davidson, Sergey Levine, Rahul Sukthankar, and Jitendra Malik. Cognitive mapping and planning for visual navigation. *arXiv preprint arXiv:1702.03920*, 3, 2017a.

Tanmay Gupta, Kevin J Shih, Saurabh Singh, Derek Hoiem, Kevin J Shih, Arun Mallya, Wei Di, Vignesh Jagadeesh, Robinson Piramuthu, K Shih, et al. Aligned image-word representations improve inductive transfer across vision-language tasks. In *ICCV*, pages 4223–4232, 2017b.

Tuomas Haarnoja, Aurick Zhou, Pieter Abbeel, and Sergey Levine. Soft actor-critic: Off-policy maximum entropy deep reinforcement learning with a stochastic actor. *arXiv preprint arXiv:1801.01290*, 2018.

Dylan Hadfield-Menell, Smitha Milli, Pieter Abbeel, Stuart J Russell, and Anca Dragan. Inverse reward design. In *Advances in neural information processing systems*, pages 6765–6774, 2017.

Danijar Hafner, Timothy Lillicrap, Ian Fischer, Ruben Villegas, David Ha, Honglak Lee, and James Davidson. Learning latent dynamics for planning from pixels. *arXiv preprint arXiv:1811.04551*, 2018.

Karol Hausman, Jost Tobias Springenberg, Ziyu Wang, Nicolas Heess, and Martin Riedmiller. Learning an embedding space for transferable robot skills. 2018.

Elad Hazan, Sham M Kakade, Karan Singh, and Abby Van Soest. Provably efficient maximum entropy exploration. *arXiv preprint arXiv:1812.02690*, 2018.

David Held, Xinyang Geng, Carlos Florensa, and Pieter Abbeel. Automatic goal generation for reinforcement learning agents. *arXiv preprint arXiv:1705.06366*, 2017.

Karl Moritz Hermann, Felix Hill, Simon Green, Fumin Wang, Ryan Faulkner, Hubert Soyer, David Szepesvari, Wojtek Czarnecki, Max Jaderberg, Denis Teplyashin, et al. Grounded language learning in a simulated 3d world. *arXiv preprint arXiv:1706.06551*, 2017.

Irina Higgins, Loic Matthey, Arka Pal, Christopher Burgess, Xavier Glorot, Matthew Botvinick, Shakir Mohamed, and Alexander Lerchner. beta-vae: Learning basic visual concepts with a constrained variational framework. *Iclr*, 2(5):6, 2017.

Irina Higgins, David Amos, David Pfau, Sebastien Racaniere, Loic Matthey, Danilo Rezende, and Alexander Lerchner. Towards a definition of disentangled representations. *arXiv preprint arXiv:1812.02230*, 2018.

Jonathan Ho and Stefano Ermon. Generative adversarial imitation learning. In *Advances in Neural Information Processing Systems*, pages 4565–4573, 2016.

Roger A Horn. The hadamard product. In *Proc. Symp. Appl. Math*, volume 40, pages 87–169, 1990.

Rein Houthooft, Xi Chen, Yan Duan, John Schulman, Filip De Turck, and Pieter Abbeel. Vime: Variational information maximizing exploration. In *Advances in Neural Information Processing Systems*, pages 1109–1117, 2016.

Robert D Howe. Tactile sensing and control of robotic manipulation. *Advanced Robotics*, 8(3): 245–261, 1993.

Drew A Hudson and Christopher D Manning. Compositional attention networks for machine reasoning. *arXiv preprint arXiv:1803.03067*, 2018.

Max Jaderberg, Volodymyr Mnih, Wojciech Marian Czarnecki, Tom Schaul, Joel Z Leibo, David Silver, and Koray Kavukcuoglu. Reinforcement learning with unsupervised auxiliary tasks. *arXiv preprint arXiv:1611.05397*, 2016.

Yiding Jiang, Shixiang Gu, Kevin Murphy, and Chelsea Finn. Language as an abstraction for hierarchical deep reinforcement learning. *arXiv preprint arXiv:1906.07343*, 2019.

Yohan Jo, Lisa Lee, and Shruti Palaskar. Combining lstm and latent topic modeling for mortality prediction. *arXiv preprint arXiv:1709.02842*, 2017.

Leslie Pack Kaelbling. Learning to achieve goals. In *IJCAI*, pages 1094–1099. Citeseer, 1993.

Lukasz Kaiser, Mohammad Babaeizadeh, Piotr Milos, Blazej Osinski, Roy H Campbell, Konrad Czechowski, Dumitru Erhan, Chelsea Finn, Piotr Kozakowski, Sergey Levine, et al. Model-based reinforcement learning for atari. *arXiv preprint arXiv:1903.00374*, 2019.

Hilbert J Kappen, Vicenç Gómez, and Manfred Opper. Optimal control as a graphical model inference problem. *Machine learning*, 87(2):159–182, 2012.

Michał Kempka, Marek Wydmuch, Grzegorz Runc, Jakub Toczek, and Wojciech Jaśkowski. ViZDoom: A Doom-based AI research platform for visual reinforcement learning. In *IEEE Conference on Computational Intelligence and Games*, pages 341–348. IEEE, Sep 2016.

Hyunjik Kim and Andriy Mnih. Disentangling by factorising. *arXiv preprint arXiv:1802.05983*, 2018.

W Bradley Knox and Peter Stone. Interactively shaping agents via human reinforcement: The tamer framework. In *Proceedings of the fifth international conference on Knowledge capture*, pages 9–16, 2009.

Jens Kober, Betty Mohler, and Jan Peters. Imitation and reinforcement learning for motor primitives with perceptual coupling. In *From motor learning to interaction learning in robots*, pages 209–225. Springer, 2010.

J Zico Kolter and Andrew Y Ng. Near-bayesian exploration in polynomial time. In *Proceedings of the 26th annual international conference on machine learning*, pages 513–520, 2009.

Brenden M Lake, Tomer D Ullman, Joshua B Tenenbaum, and Samuel J Gershman. Building machines that learn and think like people. *Behavioral and brain sciences*, 40, 2017.

Guillaume Lample and Devendra Singh Chaplot. Playing FPS games with deep reinforcement learning. In *Thirty-First AAAI Conference on Artificial Intelligence*, 2017.

Michael Laskey, Jonathan Lee, Roy Fox, Anca Dragan, and Ken Goldberg. Dart: Noise injection for robust imitation learning. *arXiv preprint arXiv:1703.09327*, 2017.

Yann LeCun, Yoshua Bengio, et al. Convolutional networks for images, speech, and time series. *The handbook of brain theory and neural networks*, 3361(10):1995, 1995.

Alex X Lee, Anusha Nagabandi, Pieter Abbeel, and Sergey Levine. Stochastic latent actor-critic: Deep reinforcement learning with a latent variable model. *arXiv preprint arXiv:1907.00953*, 2019a.

Dongheui Lee and Christian Ott. Incremental kinesthetic teaching of motion primitives using the motion refinement tube. *Autonomous Robots*, 31(2):115–131, 2011.

Kimin Lee, Laura Smith, and Pieter Abbeel. Pebble: Feedback-efficient interactive reinforcement learning via relabeling experience and unsupervised pre-training. *arXiv preprint arXiv:2106.05091*, 2021.

Lisa Lee, Emilio Parisotto, Devendra Singh Chaplot, Eric Xing, and Ruslan Salakhutdinov. Gated path planning networks. In *International Conference on Machine Learning (ICML)*, pages 2947–2955. PMLR, 2018.

Lisa Lee, Benjamin Eysenbach, Emilio Parisotto, Eric Xing, Sergey Levine, and Ruslan Salakhutdinov. Efficient exploration via state marginal matching. *arXiv preprint arXiv:1906.05274*, 2019b.

Lisa Lee, Benjamin Eysenbach, Ruslan Salakhutdinov, Chelsea Finn, et al. Weakly-supervised reinforcement learning for controllable behavior. *Neural Information Processing Systems (NeurIPS)*, 2020.

Sergey Levine. Reinforcement learning and control as probabilistic inference: Tutorial and review. *arXiv preprint arXiv:1805.00909*, 2018.

Guangliang Li, Randy Gomez, Keisuke Nakamura, Jinying Lin, Qilei Zhang, and Bo He. Improving interactive reinforcement agent planning with human demonstration. *arXiv preprint arXiv:1904.08621*, 2019.

Xiaodan Liang, Lisa Lee, Wei Dai, and Eric P Xing. Dual motion gan for future-flow embedded video prediction. In *Proceedings of the IEEE International Conference on Computer Vision (ICCV)*, pages 1744–1752, 2017a.

Xiaodan Liang, Lisa Lee, and Eric P Xing. Deep variation-structured reinforcement learning for visual relationship and attribute detection. In *Proceedings of the IEEE conference on Computer Vision and Pattern Recognition (CVPR)*, pages 848–857, 2017b.

Timothy P Lillicrap, Jonathan J Hunt, Alexander Pritzel, Nicolas Heess, Tom Erez, Yuval Tassa, David Silver, and Daan Wierstra. Continuous control with deep reinforcement learning. *arXiv preprint arXiv:1509.02971*, 2015.

Guan-Horng Liu, Avinash Siravuru, Sai Prabhakar, Manuela Veloso, and George Kantor. Learning end-to-end multimodal sensor policies for autonomous navigation. In *Conference on Robot Learning*, pages 249–261. PMLR, 2017.

Francesco Locatello, Stefan Bauer, Mario Lucic, Gunnar Rätsch, Sylvain Gelly, Bernhard Schölkopf, and Olivier Bachem. Challenging common assumptions in the unsupervised learning of disentangled representations. *arXiv preprint arXiv:1811.12359*, 2018.

James MacGlashan, Monica Babes-Vroman, Marie desJardins, Michael L Littman, Smaranda Muresan, Shawn Squire, Stefanie Tellex, Dilip Arumugam, and Lei Yang. Grounding english commands to reward functions. In *Robotics: Science and Systems*, 2015.

Marios C Machado, Marc G Bellemare, and Michael Bowling. A laplacian framework for option discovery in reinforcement learning. In *Proceedings of the 34th International Conference on Machine Learning-Volume 70*, pages 2295–2304. JMLR. org, 2017.

Sridhar Mahadevan. Proto-value functions: Developmental reinforcement learning. In *Proceedings of the 22nd international conference on Machine learning*, pages 553–560. ACM, 2005.

Ajay Mandlekar, Yuke Zhu, Animesh Garg, Jonathan Booher, Max Spero, Albert Tung, Julian Gao, John Emmons, Anchit Gupta, Emre Orbay, et al. Roboturk: A crowdsourcing platform for robotic skill learning through imitation. *arXiv preprint arXiv:1811.02790*, 2018.

Ajay Mandlekar, Danfei Xu, Roberto Martín-Martín, Yuke Zhu, Li Fei-Fei, and Silvio Savarese. Human-in-the-loop imitation learning using remote teleoperation. *arXiv preprint arXiv:2012.06733*, 2020.

Loic Matthey, Irina Higgins, Demis Hassabis, and Alexander Lerchner. dsprites: Disentanglement testing sprites dataset. https://github.com/deepmind/dsprites-dataset/, 2017.

Hongyuan Mei, Mohit Bansal, and Matthew R Walter. Listen, attend, and walk: Neural mapping of navigational instructions to action sequences. In *Thirtieth AAAI Conference on Artificial Intelligence*, 2016.

Josh Merel, Leonard Hasenclever, Alexandre Galashov, Arun Ahuja, Vu Pham, Greg Wayne, Yee Whye Teh, and Nicolas Heess. Neural probabilistic motor primitives for humanoid control. *arXiv preprint arXiv:1811.11711*, 2018.

Piotr Mirowski, Razvan Pascanu, Fabio Viola, Hubert Soyer, Andrew J Ballard, Andrea Banino, Misha Denil, Ross Goroshin, Laurent Sifre, Koray Kavukcuoglu, et al. Learning to navigate in complex environments. *arXiv preprint arXiv:1611.03673*, 2016.

Nikhil Mishra, Mostafa Rohaninejad, Xi Chen, and Pieter Abbeel. A simple neural attentive meta-learner. *arXiv preprint arXiv:1707.03141*, 2017.

Dipendra K Misra, Jaeyong Sung, Kevin Lee, and Ashutosh Saxena. Tell me dave: Context-sensitive grounding of natural language to manipulation instructions. *The International Journal of Robotics Research*, 35(1-3):281–300, 2016.

Dipendra K Misra, John Langford, and Yoav Artzi. Mapping instructions and visual observations to actions with reinforcement learning. *arXiv preprint arXiv:1704.08795*, 2017.

Volodymyr Mnih, Koray Kavukcuoglu, David Silver, Alex Graves, Ioannis Antonoglou, Daan Wierstra, and Martin Riedmiller. Playing atari with deep reinforcement learning. *arXiv preprint arXiv:1312.5602*, 2013.

Volodymyr Mnih, Adria Puigdomenech Badia, Mehdi Mirza, Alex Graves, Timothy P Lillicrap, Tim Harley, David Silver, and Koray Kavukcuoglu. Asynchronous methods for deep reinforcement learning. In *ICML*, 2016.

Katharina Mülling, Jens Kober, Oliver Kroemer, and Jan Peters. Learning to select and generalize striking movements in robot table tennis. *The International Journal of Robotics Research*, 32 (3):263–279, 2013.

Ofir Nachum, Shixiang Gu, Honglak Lee, and Sergey Levine. Near-optimal representation learning for hierarchical reinforcement learning. *arXiv preprint arXiv:1810.01257*, 2018.

Ashvin V Nair, Vitchyr Pong, Murtaza Dalal, Shikhar Bahl, Steven Lin, and Sergey Levine. Visual reinforcement learning with imagined goals. In *Advances in Neural Information Processing Systems*, pages 9191–9200, 2018.

John Nash. Non-cooperative games. *Annals of mathematics*, pages 286–295, 1951.

Tianwei Ni, Harshit Sikchi, Yufei Wang, Tejus Gupta, Lisa Lee, and Benjamin Eysenbach. F-irl: Inverse reinforcement learning via state marginal matching. *Conference on Robot Learning (CoRL)*, 2020.

Junhyuk Oh, Satinder Singh, Honglak Lee, and Pushmeet Kohli. Zero-shot task generalization with multi-task deep reinforcement learning. *arXiv preprint arXiv:1706.05064*, 2017.

Pierre-Yves Oudeyer, Frdric Kaplan, and Verena V Hafner. Intrinsic motivation systems for autonomous mental development. *IEEE transactions on evolutionary computation*, 11(2): 265–286, 2007.

Deepak Pathak, Pulkit Agrawal, Alexei A Efros, and Trevor Darrell. Curiosity-driven exploration by self-supervised prediction. In *Proceedings of the IEEE Conference on Computer Vision and Pattern Recognition Workshops*, pages 16–17, 2017.

Deepak Pathak, Parsa Mahmoudieh, Guanghao Luo, Pulkit Agrawal, Dian Chen, Yide Shentu, Evan Shelhamer, Jitendra Malik, Alexei A Efros, and Trevor Darrell. Zero-shot visual imitation. In *Proceedings of the IEEE Conference on Computer Vision and Pattern Recognition Workshops*, pages 2050–2053, 2018.

Xue Bin Peng, Angjoo Kanazawa, Jitendra Malik, Pieter Abbeel, and Sergey Levine. Sfv: Reinforcement learning of physical skills from videos. *ACM Transactions On Graphics (TOG)*, 37(6):1–14, 2018.

Ethan Perez, Florian Strub, Harm De Vries, Vincent Dumoulin, and Aaron Courville. Film: Visual reasoning with a general conditioning layer. *arXiv preprint arXiv:1709.07871*, 2017.

Jan Peters, Katharina Mulling, and Yasemin Altun. Relative entropy policy search. In *Twenty-Fourth AAAI Conference on Artificial Intelligence*, 2010.

Matthias Plappert, Rein Houthooft, Prafulla Dhariwal, Szymon Sidor, Richard Y Chen, Xi Chen, Tamim Asfour, Pieter Abbeel, and Marcin Andrychowicz. Parameter space noise for exploration. *arXiv preprint arXiv:1706.01905*, 2017.

Matthias Plappert, Marcin Andrychowicz, Alex Ray, Bob McGrew, Bowen Baker, Glenn Powell, Jonas Schneider, Josh Tobin, Maciek Chociej, Peter Welinder, et al. Multi-goal reinforcement learning: Challenging robotics environments and request for research. *arXiv preprint arXiv:1802.09464*, 2018.

Vitchyr Pong, Shixiang Gu, Murtaza Dalal, and Sergey Levine. Temporal difference models: Model-free deep rl for model-based control. *arXiv preprint arXiv:1802.09081*, 2018.

Vitchyr H Pong, Murtaza Dalal, Steven Lin, Ashvin Nair, Shikhar Bahl, and Sergey Levine. Skew-fit: State-covering self-supervised reinforcement learning. *arXiv preprint arXiv:1903.03698*, 2019.

Justin K Pugh, Lisa B Soros, and Kenneth O Stanley. Quality diversity: A new frontier for evolutionary computation. *Frontiers in Robotics and AI*, 3:40, 2016.

Martin L Puterman. *Markov Decision Processes.: Discrete Stochastic Dynamic Programming.* John Wiley & Sons, 2014.

Kate Rakelly, Aurick Zhou, Deirdre Quillen, Chelsea Finn, and Sergey Levine. Efficient off-policy meta-reinforcement learning via probabilistic context variables. *arXiv preprint arXiv:1903.08254*, 2019.

Nathan D Ratliff, J Andrew Bagnell, and Martin A Zinkevich. Maximum margin planning. In *Proceedings of the 23rd international conference on Machine learning*, pages 729–736, 2006.

Konrad Rawlik, Marc Toussaint, and Sethu Vijayakumar. On stochastic optimal control and reinforcement learning by approximate inference. In *Twenty-Third International Joint Conference on Artificial Intelligence*, 2013.

Julia Robinson. An iterative method of solving a game. *Annals of mathematics*, pages 296–301, 1951.

Manolis Savva, Angel X. Chang, Alexey Dosovitskiy, Thomas Funkhouser, and Vladlen Koltun. MINOS: Multimodal indoor simulator for navigation in complex environments. *arXiv:1712.03931*, 2017.

Tom Schaul, Daniel Horgan, Karol Gregor, and David Silver. Universal value function approximators. In *International conference on machine learning*, pages 1312–1320, 2015.

Jürgen Schmidhuber. A possibility for implementing curiosity and boredom in model-building neural controllers. In *Proc. of the international conference on simulation of adaptive behavior: From animals to animats*, pages 222–227, 1991.

Jürgen Schmidhuber. Formal theory of creativity, fun, and intrinsic motivation (1990–2010). *IEEE Transactions on Autonomous Mental Development*, 2(3):230–247, 2010.

John Schulman, Sergey Levine, Pieter Abbeel, Michael Jordan, and Philipp Moritz. Trust region policy optimization. In *International conference on machine learning*, pages 1889–1897, 2015.

John Schulman, Filip Wolski, Prafulla Dhariwal, Alec Radford, and Oleg Klimov. Proximal policy optimization algorithms. *arXiv preprint arXiv:1707.06347*, 2017.

Evan Shelhamer, Parsa Mahmoudieh, Max Argus, and Trevor Darrell. Loss is its own reward: Self-supervision for reinforcement learning. *arXiv preprint arXiv:1612.07307*, 2016.

Rui Shu, Yining Chen, Abhishek Kumar, Stefano Ermon, and Ben Poole. Weakly supervised disentanglement with guarantees. *arXiv preprint arXiv:1910.09772*, 2019.

David Silver, Aja Huang, Chris J Maddison, Arthur Guez, Laurent Sifre, George Van Den Driessche, Julian Schrittwieser, Ioannis Antonoglou, Veda Panneershelvam, Marc Lanctot, et al. Mastering the game of go with deep neural networks and tree search. *Nature*, 529(7587): 484–489, 2016.

David Silver, Thomas Hubert, Julian Schrittwieser, Ioannis Antonoglou, Matthew Lai, Arthur Guez, Marc Lanctot, Laurent Sifre, Dharshan Kumaran, Thore Graepel, et al. Mastering chess and shogi by self-play with a general reinforcement learning algorithm. *arXiv preprint arXiv:1712.01815*, 2017.

Avi Singh, Larry Yang, Kristian Hartikainen, Chelsea Finn, and Sergey Levine. End-to-end robotic reinforcement learning without reward engineering. *arXiv preprint arXiv:1904.07854*, 2019.

Hailuo Song, Ao Li, Tong Wang, and Minghui Wang. Multimodal deep reinforcement learning with auxiliary task for obstacle avoidance of indoor mobile robot. *Sensors*, 21(4):1363, 2021.

Thomas H Speeter. A tactile sensing system for robotic manipulation. *The International Journal of Robotics Research*, 9(6):25–36, 1990.

Bradly C Stadie, Sergey Levine, and Pieter Abbeel. Incentivizing exploration in reinforcement learning with deep predictive models. *arXiv preprint arXiv:1507.00814*, 2015.

Kenneth O Stanley and Risto Miikkulainen. Evolving neural networks through augmenting topologies. *Evolutionary computation*, 10(2):99–127, 2002.

Adrien Ali Taïga, William Fedus, Marlos C Machado, Aaron Courville, and Marc G Bellemare. Benchmarking bonus-based exploration methods on the arcade learning environment. *arXiv preprint arXiv:1908.02388*, 2019.

Haoran Tang, Rein Houthooft, Davis Foote, Adam Stooke, OpenAI Xi Chen, Yan Duan, John Schulman, Filip DeTurck, and Pieter Abbeel. # exploration: A study of count-based exploration for deep reinforcement learning. In *Advances in neural information processing systems*, pages 2753–2762, 2017.

Stefanie A Tellex, Thomas Fleming Kollar, Steven R Dickerson, Matthew R Walter, Ashis Banerjee, Seth Teller, and Nicholas Roy. Understanding natural language commands for robotic navigation and mobile manipulation. 2011.

Evangelos A Theodorou and Emanuel Todorov. Relative entropy and free energy dualities: Connections to path integral and kl control. In *2012 IEEE 51st IEEE Conference on Decision and Control (CDC)*, pages 1466–1473. IEEE, 2012.

Valentin Thomas, Jules Pondard, Emmanuel Bengio, Marc Sarfati, Philippe Beaudoin, Marie-Jean Meurs, Joelle Pineau, Doina Precup, and Yoshua Bengio. Independently controllable features. *arXiv preprint arXiv:1708.01289*, 2017.

Marc Toussaint and Amos Storkey. Probabilistic inference for solving discrete and continuous state markov decision processes. In *Proceedings of the 23rd international conference on Machine learning*, pages 945–952. ACM, 2006.

Hsiao-Yu Tung, Adam W Harley, Liang-Kang Huang, and Katerina Fragkiadaki. Reward learning from narrated demonstrations. In *Proceedings of the IEEE Conference on Computer Vision and Pattern Recognition*, pages 7004–7013, 2018.

Sjoerd van Steenkiste, Francesco Locatello, Jürgen Schmidhuber, and Olivier Bachem. Are disentangled representations helpful for abstract visual reasoning? In *Advances in Neural Information Processing Systems*, pages 14222–14235, 2019.

Mel Vecerik, Oleg Sushkov, David Barker, Thomas Rothörl, Todd Hester, and Jon Scholz. A practical approach to insertion with variable socket position using deep reinforcement learning. In *2019 International Conference on Robotics and Automation (ICRA)*, pages 754–760. IEEE, 2019.

Oriol Vinyals, Igor Babuschkin, Wojciech M Czarnecki, Michaël Mathieu, Andrew Dudzik, Junyoung Chung, David H Choi, Richard Powell, Timo Ewalds, Petko Georgiev, et al. Grandmaster level in starcraft ii using multi-agent reinforcement learning. *Nature*, 575(7782):350–354, 2019.

Manuel Watter, Jost Springenberg, Joschka Boedecker, and Martin Riedmiller. Embed to control: A locally linear latent dynamics model for control from raw images. In *Advances in neural information processing systems*, pages 2746–2754, 2015.

Yi Wu, Yuxin Wu, Georgia Gkioxari, and Yuandong Tian. Building generalizable agents with a realistic and rich 3d environment. *arXiv preprint arXiv:1801.02209*, 2018.

Annie Xie, Avi Singh, Sergey Levine, and Chelsea Finn. Few-shot goal inference for visuomotor learning and planning. *arXiv preprint arXiv:1810.00482*, 2018.

Dan Xie, Sinisa Todorovic, and Song-Chun Zhu. Inferring "dark matter" and "dark energy" from videos. In *The IEEE International Conference on Computer Vision (ICCV)*, December 2013.

Huijuan Xu and Kate Saenko. Ask, attend and answer: Exploring question-guided spatial attention for visual question answering. In *European Conference on Computer Vision*, pages 451–466. Springer, 2016.

Tianbing Xu, Qiang Liu, Liang Zhao, and Jian Peng. Learning to explore with meta-policy gradient. *arXiv preprint arXiv:1803.05044*, 2018.

Fusun Yaman, Thomas J Walsh, Michael L Littman, et al. Learning lexicographic preference models. In *Preference learning*, pages 251–272. Springer, 2010.

Denis Yarats, Amy Zhang, Ilya Kostrikov, Brandon Amos, Joelle Pineau, and Rob Fergus. Improving sample efficiency in model-free reinforcement learning from images. *arXiv preprint arXiv:1910.01741*, 2019.

Haonan Yu, Xiaochen Lian, Haichao Zhang, and Wei Xu. Guided feature transformation (gft): A neural language grounding module for embodied agents. *arXiv preprint arXiv:1805.08329*, 2018a.

Haonan Yu, Haichao Zhang, and Wei Xu. Interactive grounded language acquisition and generalization in a 2d world. *arXiv preprint arXiv:1802.01433*, 2018b.

Tianhe Yu, Gleb Shevchuk, Dorsa Sadigh, and Chelsea Finn. Unsupervised visuomotor control through distributional planning networks. *arXiv preprint arXiv:1902.05542*, 2019.

Marvin Zhang, Sharad Vikram, Laura Smith, Pieter Abbeel, Matthew J Johnson, and Sergey Levine. Solar: Deep structured latent representations for model-based reinforcement learning. *arXiv preprint arXiv:1808.09105*, 2018a.

Tianhao Zhang, Zoe McCarthy, Owen Jow, Dennis Lee, Xi Chen, Ken Goldberg, and Pieter Abbeel. Deep imitation learning for complex manipulation tasks from virtual reality teleoperation. In *2018 IEEE International Conference on Robotics and Automation (ICRA)*, pages 5628–5635. IEEE, 2018b.

Hang Zhao, Chuang Gan, Andrew Rouditchenko, Carl Vondrick, Josh McDermott, and Antonio Torralba. The sound of pixels. *arXiv preprint arXiv:1804.03160*, 2018.

Henry Zhu, Abhishek Gupta, Aravind Rajeswaran, Sergey Levine, and Vikash Kumar. Dexterous manipulation with deep reinforcement learning: Efficient, general, and low-cost. In *2019 International Conference on Robotics and Automation (ICRA)*, pages 3651–3657. IEEE, 2019.

Yuke Zhu, Roozbeh Mottaghi, Eric Kolve, Joseph J Lim, Abhinav Gupta, Li Fei-Fei, and Ali Farhadi. Target-driven visual navigation in indoor scenes using deep reinforcement learning. In *Robotics and Automation (ICRA), 2017 IEEE International Conference on*, pages 3357–3364. IEEE, 2017.

Brian D Ziebart. Modeling purposeful adaptive behavior with the principle of maximum causal entropy. 2010.

Brian D Ziebart, Andrew L Maas, J Andrew Bagnell, and Anind K Dey. Maximum entropy inverse reinforcement learning. In *Aaai*, volume 8, pages 1433–1438. Chicago, IL, USA, 2008.

Brian D Ziebart, Nathan Ratliff, Garratt Gallagher, Christoph Mertz, Kevin Peterson, J Andrew Bagnell, Martial Hebert, Anind K Dey, and Siddhartha Srinivasa. Planning-based prediction for pedestrians. In *2009 IEEE/RSJ International Conference on Intelligent Robots and Systems*, pages 3931–3936. IEEE, 2009.